



**AFRL-AFOSR-VA-TR-2017-0021**

---

3D Printed Composites for Topology-Transforming  
Multifunctional Devices

**Kurt Maute**  
**REGENTS OF THE UNIVERSITY OF COLORADO THE**  
**3100 MARINE ST 572 UCB**  
**BOULDER, CO 80309-0001**

---

**01/26/2017**  
**Final Report**

<p><b>DISTRIBUTION A: Distribution approved for public release.</b></p>
---

Air Force Research Laboratory  
AF Office Of Scientific Research (AFOSR)/RTB2

REPORT DOCUMENTATION PAGE					Form Approved OMB No. 0704-0188	
<p>The public reporting burden for this collection of information is estimated to average 1 hour per response, including the time for reviewing instructions, searching existing data sources, gathering and maintaining the data needed, and completing and reviewing the collection of information. Send comments regarding this burden estimate or any other aspect of this collection of information, including suggestions for reducing the burden, to the Department of Defense, Executive Service Directorate (0704-0188). Respondents should be aware that notwithstanding any other provision of law, no person shall be subject to any penalty for failing to comply with a collection of information if it does not display a currently valid OMB control number.</p> <p><b>PLEASE DO NOT RETURN YOUR FORM TO THE ABOVE ORGANIZATION.</b></p>						
1. REPORT DATE (DD-MM-YYYY) 15-11-2016		2. REPORT TYPE Final Report			3. DATES COVERED (From - To) July 15, 2013 - July 14, 2016	
4. TITLE AND SUBTITLE 3D Printed Composites for Topology-Transforming Multifunctional Devices				5a. CONTRACT NUMBER FA9550-13-1-0088		
				5b. GRANT NUMBER		
				5c. PROGRAM ELEMENT NUMBER		
6. AUTHOR(S) Kurt Maute, Jerry H. Qi, and Martin L. Dunn				5d. PROJECT NUMBER		
				5e. TASK NUMBER		
				5f. WORK UNIT NUMBER		
7. PERFORMING ORGANIZATION NAME(S) AND ADDRESS(ES) University of Colorado Boulder, Boulder, CO 80309, U.S.A. Georgia Institute of Technology, North Ave NW, Atlanta, GA 30332, U.S.A.					8. PERFORMING ORGANIZATION REPORT NUMBER	
9. SPONSORING/MONITORING AGENCY NAME(S) AND ADDRESS(ES) U. S. Air Force Office of Scientific Research Mechanics of Multifunctional Materials & Microsystems Program 875 North Randolph Street, Arlington, VA 22203, U.S.A.					10. SPONSOR/MONITOR'S ACRONYM(S)	
					11. SPONSOR/MONITOR'S REPORT NUMBER(S)	
12. DISTRIBUTION/AVAILABILITY STATEMENT Distribution A - Approved for Public Release						
13. SUPPLEMENTARY NOTES						
14. ABSTRACT <p>The goal of the research was to develop a new methodology for the fabrication and the design of new multifunctional composites and devices using 3D printing. The main accomplishments of this project can be summarized as follows: 1) Proposing and demonstrating the 4D printing concept and novel printed active composites (PACs); 2) developing multiple PAC continuum mechanics PAC models of various levels of accuracy and complexity; 3) developing the 4D printing concept to design PACs undergoing multiple shape changes; 4) developing a PAC-based concept that enables reversible shape changes; 5) application of PACs for printed origami design; 6) developing a finite element framework for the optimum design of PACs by topology optimization; 7) optimizing and experimentally characterizing PACs that undergo desired shape changes.</p>						
15. SUBJECT TERMS 3D Printing, Active Composites, Shape Memory Polymers, Topology Optimization						
16. SECURITY CLASSIFICATION OF:			17. LIMITATION OF ABSTRACT	18. NUMBER OF PAGES 74	19a. NAME OF RESPONSIBLE PERSON Kurt Maute	
a. REPORT UU	b. ABSTRACT UU	c. THIS PAGE UU			19b. TELEPHONE NUMBER (Include area code) 303-735-2103	

## INSTRUCTIONS FOR COMPLETING SF 298

**1. REPORT DATE.** Full publication date, including day, month, if available. Must cite at least the year and be Year 2000 compliant, e.g. 30-06-1998; xx-06-1998; xx-xx-1998.

**2. REPORT TYPE.** State the type of report, such as final, technical, interim, memorandum, master's thesis, progress, quarterly, research, special, group study, etc.

**3. DATES COVERED.** Indicate the time during which the work was performed and the report was written, e.g., Jun 1997 - Jun 1998; 1-10 Jun 1996; May - Nov 1998; Nov 1998.

**4. TITLE.** Enter title and subtitle with volume number and part number, if applicable. On classified documents, enter the title classification in parentheses.

**5a. CONTRACT NUMBER.** Enter all contract numbers as they appear in the report, e.g. F33615-86-C-5169.

**5b. GRANT NUMBER.** Enter all grant numbers as they appear in the report, e.g. AFOSR-82-1234.

**5c. PROGRAM ELEMENT NUMBER.** Enter all program element numbers as they appear in the report, e.g. 61101A.

**5d. PROJECT NUMBER.** Enter all project numbers as they appear in the report, e.g. 1F665702D1257; ILIR.

**5e. TASK NUMBER.** Enter all task numbers as they appear in the report, e.g. 05; RF0330201; T4112.

**5f. WORK UNIT NUMBER.** Enter all work unit numbers as they appear in the report, e.g. 001; AFAPL30480105.

**6. AUTHOR(S).** Enter name(s) of person(s) responsible for writing the report, performing the research, or credited with the content of the report. The form of entry is the last name, first name, middle initial, and additional qualifiers separated by commas, e.g. Smith, Richard, J, Jr.

**7. PERFORMING ORGANIZATION NAME(S) AND ADDRESS(ES).** Self-explanatory.

**8. PERFORMING ORGANIZATION REPORT NUMBER.** Enter all unique alphanumeric report numbers assigned by the performing organization, e.g. BRL-1234; AFWL-TR-85-4017-Vol-21-PT-2.

**9. SPONSORING/MONITORING AGENCY NAME(S) AND ADDRESS(ES).** Enter the name and address of the organization(s) financially responsible for and monitoring the work.

**10. SPONSOR/MONITOR'S ACRONYM(S).** Enter, if available, e.g. BRL, ARDEC, NADC.

**11. SPONSOR/MONITOR'S REPORT NUMBER(S).** Enter report number as assigned by the sponsoring/monitoring agency, if available, e.g. BRL-TR-829; -215.

**12. DISTRIBUTION/AVAILABILITY STATEMENT.** Use agency-mandated availability statements to indicate the public availability or distribution limitations of the report. If additional limitations/ restrictions or special markings are indicated, follow agency authorization procedures, e.g. RD/FRD, PROPIN, ITAR, etc. Include copyright information.

**13. SUPPLEMENTARY NOTES.** Enter information not included elsewhere such as: prepared in cooperation with; translation of; report supersedes; old edition number, etc.

**14. ABSTRACT.** A brief (approximately 200 words) factual summary of the most significant information.

**15. SUBJECT TERMS.** Key words or phrases identifying major concepts in the report.

**16. SECURITY CLASSIFICATION.** Enter security classification in accordance with security classification regulations, e.g. U, C, S, etc. If this form contains classified information, stamp classification level on the top and bottom of this page.

**17. LIMITATION OF ABSTRACT.** This block must be completed to assign a distribution limitation to the abstract. Enter UU (Unclassified Unlimited) or SAR (Same as Report). An entry in this block is necessary if the abstract is to be limited.

Final Report for FA9550-13-1-0088

Project

## 3D Printed Composites for Topology-Transforming Multifunctional Devices

PIs: J Qi<sup>1</sup>, K. Maute<sup>2</sup>, M. Dunn<sup>3</sup>

<sup>1</sup> Georgia Institute of Technology

<sup>2</sup> University of Colorado Boulder

<sup>3</sup> Singapore University of Technology and Design

Program Manager: Dr. Byung-Lip Lee, AFOSR/RSA



## Executive Summary

The goal of the research was to develop a new methodology for the fabrication and the design of new multifunctional composites and devices using 3D printing. The main accomplishments of this project can be summarized as follows: 1) Proposing and demonstrating the 4D printing concept and novel printed active composites (PACs); 2) developing multiple PAC continuum mechanics PAC models of various levels of accuracy and complexity; 3) developing the 4D printing concept to design PACs undergoing multiple shape changes; 4) developing a PAC-based concept that enables reversible shape changes; 5) application of PACs for printed origami design; 6) developing a finite element framework for the optimum design of PACs by topology optimization; 7) optimizing and experimentally characterizing PACs that undergo desired shape changes.

The outcomes of this research project were published in 14 peer-reviewed journal papers. Our paper on topology optimization for PACs was selected featured article in the ASME Journal of Mechanical Design. Our work on 4D printing and PAM was reported by a variety of media, including NPR and ABC, Denver Post, and others.

## 1. Summary of Major Research Activities

### 1.1 Printed Active Composites and 4D Printing

Recent advances in 3D printing allow the precise placement of multiple materials at micrometer resolution with essentially no restrictions on the geometric complexity of the spatial arrangement. Complex 3D solids can be created with highly non-regular material distributions in an optimal fashion. In this project, we exploit these advances and introduce the paradigm of *printed active composites* (PACs). We directly print a composite from a CAD file that specifies the inhomogeneous material layout at the lamina and laminate level. This process has considerable design freedom to enable creation of composites with complex and controllable anisotropic thermomechanical behavior *via* prescribing the material layout of active and inactive phases. Our PACs are *soft* composites consisting of glassy polymer inclusions, such as fibers, reinforcing an elastomeric matrix. The glassy polymer phase exhibits a shape memory effect [1, 2] and we use this to create *active* soft composites where the glassy polymer phase serves as a switch to affect the shape memory behavior of the composite. In this manner we imbue the active composites with intelligence *via* the lamina and laminate architecture and the thermomechanical training process. The active motion of the PAC is essential to the 4D printing concept, which is in the spirit of the recent developments of Tibbits [3], although our work differs significantly in terms of the physical phenomena at play and the emphasis on understanding them. Upon the initial development of 4D printing and PAC, we further pushed the design space of 4D printing by developing three new types of designs: 1) sequential folding of components using digital shape memory polymers; 2) multiple shape change printed active composites where multiple types of shape memory fibers are used to achieve activation of the composites at different time and different conditions; 3) reversible shape changing composites where we use both shape memory polymers and hydrogels to achieve autonomous shape change without the assistance of external forces.

Our major efforts on modeling and experimental verification included: 1) In order to gain in-depth understanding of interplay between different design parameters of PAM, we developed a suite of

theoretical models that vary in phenomena captured, accuracy, and complexity. These models were compared against experiments. 2) We investigated the effects of oxygen on the interface properties of the 3D printed materials; 3) Guided by the theoretical analysis, we applied the 4D printing concept to create PAC that deform into complicated geometries, such as 4D printed origami. 4) We explored how to use the frontal polymerization method to create folding structures. 5) We studied methods of integrating conductive ink with 3D/4D printing techniques to enhance the multi-functionality of PACs.

## 1.2 Design and Optimization Methodology

One of the primary goals of this project was the development and application of a design optimization methodology for determining the precise and optimal layout of functional composites realized by 3D/4D printing. State-of-the-art multi-material printers allow fabricating highly non-regular (but carefully prescribed) spatial arrangements of multiple polymers. To take advantage of this capability, we developed two novel 3D topology optimization approaches that determine the precise geometry of each material phase within the composite. The optimization method accounts for the complex physical phenomena of PACs via proper mechanical models and high-fidelity finite element predictions.

We studied two optimization approaches; one describes the geometry of the material arrangement via the spatial distribution of material parameters at the macro scale. The second approach resolves the material architecture via level set functions that describe the microstructural layout. The first approach, often called *density* approach, has been used successfully in the past for a broad range of structural and material design problems [4] but not yet for the design of 3D PACs. We have studied the density approach for the design of PACs approximating the shape memory behavior of the active phase by a simple eigenstrain model. The optimized material layouts were then printed on an Object 260 printer (Stratasys, Edina, MN, USA). This study served mainly as proof-of-concept and revealed several issues of the density method.

Albeit robust and easy to implement for simple kinematic and constitutive models, the main disadvantages of the density approach are that (i) it cannot resolve reliably complex nonlinear mechanical phenomena and (ii) it requires post-processing to extract the final material layout which then can be printed. To avoid these issues, we developed and integrated a Level Set Method (LSM) used to describe the microstructural geometry and a generalized version of the eXtended Finite Element Method (XFEM) for discretizing the mechanical models and predicting the PAC response.

We developed a simple, computationally efficient, but still sufficiently accurate model to predict the PAC response at the training stage and after activation. We compared this new model against an even simpler model that relies on crude approximations of the training strains and verified our new model against experimental data. We integrated the simplified PAC models into our LSM-XFEM optimization framework and applied it to optimizing PACs that assume a target shape upon activation. The optimized designs were printed and their behavior studied experimentally. The optimization study showed that the proposed analysis and optimization methods are well suited to design PACs that exhibit a desired response.

We extended our PAC model to account for finite strains at the training stage and after activation. This work required extensive research on the stability of the XFEM formulation of finite strains models and we developed novel stabilization approach. We integrated the finite strain PAC model into our LSM-

XFEM optimization framework and performed exploratory studies on optimizing PACs that assume a target shape upon activation. Furthermore, we studied the influence of imperfect bonding between material phases on the optimum design by incorporating a cohesive zone model into the mechanical model.

### 1.3 Publications

The outcomes and findings of this project were published in the following peer-reviewed journal papers.

- [1] \*Ge, Q., Qi, H.J., Dunn, M.L., 2013, Active Materials by 4D Printing. *Applied Physics Letter*, 103, 131901.
- [2] Ge, Q., Dunn, C., Qi, H.J., Dunn, M.L., 2014. Active Origami by 4D Printing. *Smart Materials and Structures*, 23, 094007-15.
- [3] Yu, K., Ge, Q., Qi, H.J., 2014, Reduced Time as a Unified Parameter Determining Fixity and Free Recovery of Shape Memory Polymers. *Nature Communication*, 5:3066.
- [4] Yu, K., Ritchie, A., Mao, Y., Dunn, M.L., Qi, H.J., 2015. Controlled Sequential Shape Changing Components by 3D Printing of Shape Memory Polymer Multimaterials. *Procedia IUTAM*, 12, 193-203.
- [5] \*\*K. Maute, A. Tkachuk, J. Wu, H. J. Qi, Z. Ding, and M.L. Dunn. 2015. Level Set Topology Optimization of Printed Active Composites. *ASME Journal of Mechanical Design*, 137: 111704-1, 2015.
- [6] Mao, Y., Yu, K., Isakov, M., Wu, J., Dunn, M.L., and Qi, H.J., 2015. Sequential Self-Folding Structures by 3D Printed Digital Shape Memory Polymers, *Scientific Reports*, 5:13616.
- [7] Wu, J., Yuan, C., Ding, Z., Isakov, M., Mao, Y., Wang, T., Dunn, M.L., Qi, H.J. 2016. Multi-shape active composites by 3D printing of digital shape memory polymers. *Scientific Reports* 6:24224.
- [8] Mao, Y., Ding, Z., Yuan, C., Ai, S., Isakov, M., Wu, J., Wang, T., Dunn, M.L., and Qi, H.J., 2016. 3D Printed Reversible Shape Changing Component with Stimuli Responsive Materials. *Scientific Reports* 6:24761.
- [9] Zhao, Z, Mu, X., Wu, J., Qi, H.J., Fang, D., 2016. Effects of oxygen on interfacial strength of incremental forming of materials by photopolymerization. *Extreme Mechanics Letters* 9(1):108–118.
- [10] Zhao, Z, Wu, J., Mu, X., Qi, H.J., Fang, D., 2016. Origami Folding by Frontal Photopolymerization, submitted.
- [11] Mu, Q, Dunn, C.K. Wang, L., Dunn, M.L., Qi, H.J., Wang, T., 2016. Thermal cure effects on electromechanical properties of conductive wires by direct ink write for 4D printing and soft machines, submitted.
- [12] Sharma, A., Villanueva, H., Maute, 2016. On Shape Sensitivities with Heaviside-Enriched XFEM, submitted to Structural and Multidisciplinary Optimization.
- [13] Behrou, R., Lawry, M., Maute, K., 2016. Level set topology optimization of structural problems with interface cohesion, submitted to Int. J. Num. Meth. Engrg.
- [14] Lawry, M., Maute, K., 2016. Level set shape and topology optimization of finite strain bilateral contact problems, submitted to Int. J. Num. Meth. Engrg.

\* This work was widely reported by the media, including NPR-online, ABC, Denver Post, Engineering and Technology Magazine, NASA Tech Briefs-Online, etc. At the end of November 2013, it was estimated that 4.5M people was reached through these reports.

\*\* Featured paper in special issue of *ASME Journal of Mechanical design* on additive manufacturing in December 2015.

## 2. Research Efforts and Accomplishments

### 2.1 Fundamental Models and Experimental Studies

#### 2.1.1 Printed Active Composites (PACs) by 4D Printing

We realize the PAC concept *via* the processing approach shown in Figure 2.1.1-1a. Briefly, we design the complete 3D architecture of the fibers and matrix in a CAD file to yield specific active behavior based on understanding developed from theory and simulation, and use a 3D multimaterial polymer printer (Objet Connex 260, Stratasys, Edina, MN, USA) to print the composite. We design the matrix to be an elastomer and the fibers to be a glassy polymer with tailored thermomechanical, including shape-memory, behavior. This design is printed directly and results in a film that contains matrix and fiber material at an in-plane resolution of 32–64  $\mu\text{m}$ , depending on the printing resolution (Figure 2.1.1-1b). The complete composite architecture is then realized by printing multiple film layers to create an individual lamina and ultimately multiple layers to create the 3D laminate. We measured the storage modulus  $E_s$  of the of the matrix, fiber, and the composites in  $x$ -direction with a dynamic mechanical analyzer (DMA) in uniaxial loading at 0.1 Hz as a function of temperature from 60  $^{\circ}\text{C}$  to 15  $^{\circ}\text{C}$  (Figure 2.1.1-1c). The matrix modulus decreases linearly with temperature, consistent with rubber entropic elasticity; the slight increase at 15  $^{\circ}\text{C}$  is because this is close to the glass transition region and continued decreases in temperature result in large increases in  $E_s$ .

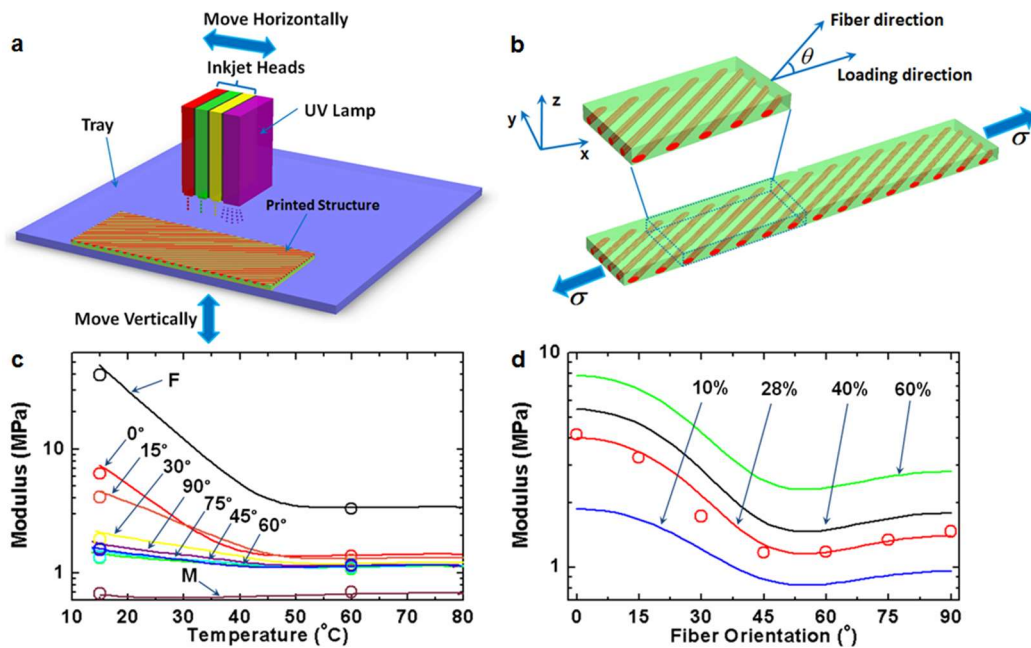


Figure 2.1.1-1. (a) Schematic illustrating the PAC printing process. The inkjet heads move horizontally above the tray depositing multimaterial droplets of polymer ink at prescribed positions, wiping them into a smooth film, and then UV photopolymerizing the film. After one film layer is completed, the tray moves down to print the next layer. (b) Schematic of a PAC lamina; fibers are oriented at an angle  $\theta$  from  $x$ -direction (the loading direction). (c) The storage modulus  $E_s$  in  $x$ -direction of the matrix (M), fiber (F), and the composites from 60  $^{\circ}\text{C}$  to 15  $^{\circ}\text{C}$ , along with the modulus obtained from quasi-static uniaxial tensile tests at 60 $^{\circ}\text{C}$  and 15 $^{\circ}\text{C}$  (circles). (d) Theoretical estimates of the relaxed modulus  $E_r$  versus fiber orientation, including experiments at  $\nu_f = 0.28$  (circles) at 15  $^{\circ}\text{C}$ .

The composites show an increasing modulus as temperature decreases, with a large variation centered at about 40 °C, which is associated with the glass transition of the fibers. Considerable anisotropy exists, especially as the fibers transition to the glassy state and stiffen. Also shown as circles in Figure 2.1.1-1c are results for the modulus obtained from quasi-static uniaxial tensile tests at 60 °C and 15 °C; they are in good agreement with the DMA results. Since the relaxation contributes importantly to the shape memory behavior of the composites, we plot the relaxed modulus (after 30 minutes) for each as a function of fiber orientation in Figure 2.1.1-1d. Also shown are theoretical estimates (solid lines) based on a recent theory of fiber-reinforced elastomers (Guo et al. [5, 6], Lopez-Pamies et al.[7], deBotton et al.[8]). The theory describes the experiments well and both show significant anisotropy in the response.

We design PACs that exhibit the shape memory effect over the range from  $T_L = 15$  °C to  $T_H = 60$  °C. To exercise the shape memory effect (Figure 2.1.1-2a) we deform samples at  $T_H = 60$  °C which is above  $T_g$  of the fibers (~35 °C), and then maintain the applied stress on the sample while cooling it to  $T_L = 15$  °C at a rate of 2 °C/min. At  $T_L$  the matrix is still in the rubbery state but the fibers have transformed to the glassy state. During cooling, the strain decreases slightly, due to thermal strain of the constituents. After holding the sample at  $T_L$  for a time sufficient to equilibrate the strain (~5 min), we released the stress and observed elastic unloading, the magnitude of which depends on the fiber orientation. At this stage the composite is in its fixed configuration and we characterized the degree of fixity by  $R_f = (\varepsilon_u - \varepsilon_T) / (\varepsilon_m - \varepsilon_T)$ , where  $\varepsilon_m$  and  $\varepsilon_u$  are the axial strains before and after the unloading step, and  $\varepsilon_T$  is the thermal strain at  $T_L$ . Finally, we recover the strain by heating the unconstrained sample at 2 °C/min to 60 °C. Figure 2.1.1-2b shows the applied temperature and stress cycle and Figure 2.1.1-2c shows the strain response for the composites as well as for the fiber and matrix, indicating a significant anisotropy in the shape memory behavior of the composites as a function of fiber orientation; this is illustrated specifically for the fixity in Figure 2.1.1-2d. The fixity as a function of  $\theta$  follows the behavior of the relaxed modulus  $E_r$ , exhibiting a slight minimum at  $\theta \sim 45$ -60°. Predictions of a theoretical model, based on combining models of hyperelastic composites with those describing the shape memory behavior of glassy polymers are in good agreement with measurements for the shape memory cycle and fixity (Figure 2.1.1-2d). We note that the polymer fibers themselves exhibit shape memory ( $R_f \sim 80\%$ ), while the matrix does not ( $R_f = 0\%$ ). Simulations show that fixity increases with increasing fiber volume fraction as this provides increasing stiffness to hold the composite in its prescribed deformation state after cooling. For all volume fractions, the fibers are most effective in terms of providing fixity when aligned with the load, but this is at the expense of reduced strain for a fixed stress.

We further exploit the anisotropic shape memory behavior of the active lamina to create PAC laminates in Figure 2.1.1-3. We design laminates with varying fiber orientations and volume fractions, and we even allow these design parameters to vary within a lamina, an aspect that can be readily achieved via printing. Figure 2.1.1-3a shows the notional concept: a two-layer laminate with a prescribed fiber architecture is printed, then heated, stretched, cooled, and released. Upon release of the stress it assumes a complex temporary shape, depending on the fiber architecture. Upon reheating it recovers its original shape, a flat rectangular strip. Figure 2.1.1-3b shows an actual strip in its original shape and then Figure 2.1.1-3c-h shows the results of this process with strips that are nominally identical macroscopically,

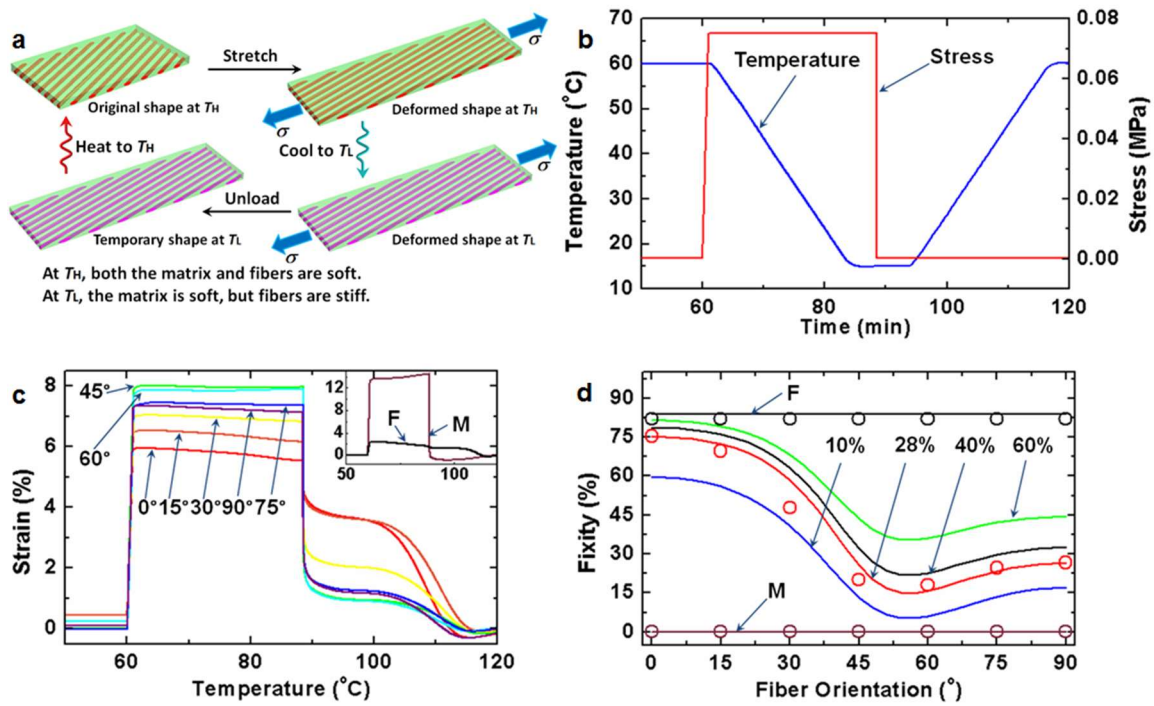


Figure 2.1.1-2. Shape memory behavior of active composite lamina. (a) Schematic of a shape memory cycle. (b) Thermomechanical loading program for the shape memory behavior of the active composite lamina. (c) Strain-time response of the  $v_f = 0.28$  composites (the inset denotes the matrix (M) and fibers (F)). (d) Predictions of fixity versus fiber orientation are compared to experiments (circles).

but have differing fiber architectures. The laminates in Figure 2.1.1-3c-e each have two layers of equal thickness (0.5 mm), one of them has a fiber volume fraction of  $v_f = 0.25$  and the other is pure matrix ( $v_f = 0$ ), and  $\theta = 0^{\circ}$ ,  $90^{\circ}$ , and  $30^{\circ}$  in Figures 2.1.1-3c, d, and e, respectively. Both the  $\theta = 0^{\circ}$  and  $90^{\circ}$  strips roll into coils, with the  $\theta = 0^{\circ}$  having a much larger curvature due to the increased fixity of a  $\theta = 0^{\circ}$  lamina versus a  $\theta = 90^{\circ}$  lamina. In general, the magnitude of the curvature depends on the composite geometries and properties, the applied mechanical load, and the thermal history; all of these are design variables. The strip with  $\theta = 30^{\circ}$  coils into a helix due to the shear-tension coupling of the laminate. The laminates of Figure 2.1.1-3f, g, h have alternating regions of segments with two layers, one with fibers ( $v_f = 0.25$ ) and the other without fibers ( $v_f = 0$ ).

The ordering of the segments is such that the fibers alternate from being in the top layer and bottom layer along the strip. In Figure 2.1.1-3f, the fibers are at  $\theta = 0^{\circ}$  and so the strip assumes the shape of alternating bent segments, while in Figure 2.1.1-3g, the fibers are at  $\theta = 0^{\circ}$  in the top layer and at  $\theta = 30^{\circ}$  in the bottom layer leading to a combination of bending and twisting of the strip in alternating fashion. In Figure 2.1.1-3h, the fibers are all at  $\theta = 0^{\circ}$  but are patterned in segments along the strip of different lengths that lead to a variation of curvature in each segment.



Figure 2.1.1-4 shows an extension of this concept to realize a shape with complex, nonuniform curvature, essentially a sculpted surface. Here a two-layer laminate (80 mm × 80 mm) is fabricated but

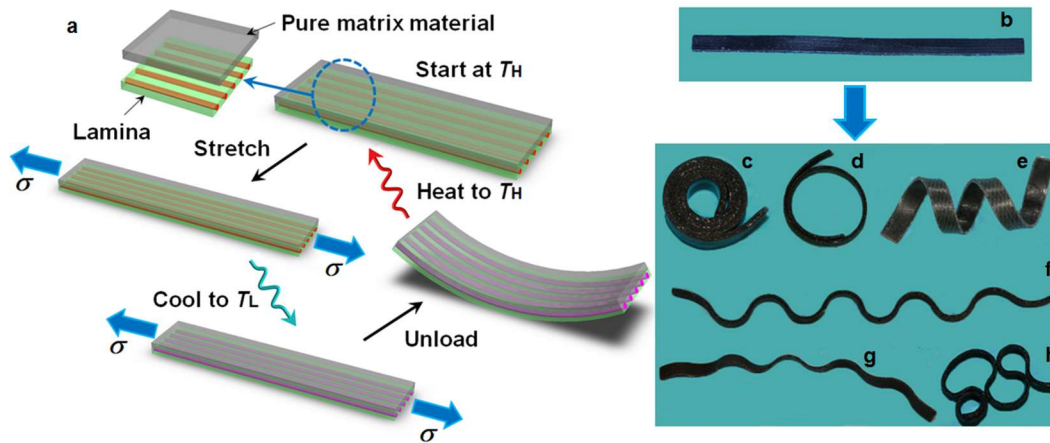


Figure 2.1.1-3. Complex low-temperature shapes of active composite laminates obtained by design of the laminate architecture. (a) A two-layer laminate designed with one layer being a lamina with fibers at a prescribed orientation and one layer being pure matrix material is printed, then heated, stretched, cooled, and released. Upon release of the stress it assumes a complex shape, depending on the laminate architecture. When reheating it then assumes its original shape, a flat rectangular strip. (b) shows an actual strip in its original shape and (c) - (h) show results of this process with differing fiber architectures.

the architecture of the fibers includes a spatial variation in both its orientation and volume fraction, to yield the desired curvature. Over each end of the laminate  $\theta = 0^\circ$  fibers exist at a volume fraction that varies with position ranging from  $v_f = 0.25$  at the end of the laminate to  $v_f = 0.14$  toward the center of the laminate (the precise layout is shown in Supplementary Material). The laminate is antisymmetric, with respect to the planar dimensions. The surface of the laminate has a randomly printed patchwork, intended to be reminiscent of the interesting artistic and architectural forms created by 3D printing by Oxman [9]. Unlike that complex surface that was directly printed in 3D, ours was created as a flat plate and then following our thermomechanical protocol, it assumed the curved shape as a result of the fibrous architecture. While the patchwork pattern here is only for aesthetic purposes, applications can be envisioned where the pattern has functional purposes.

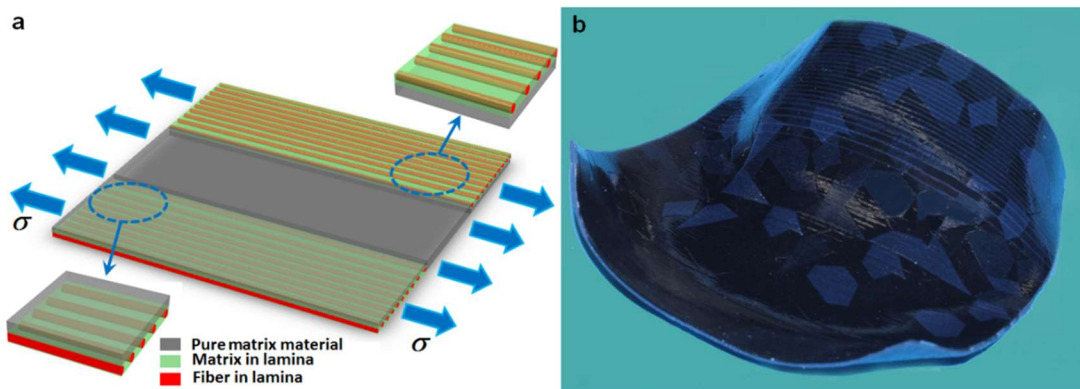


Figure 2.1.1-4. A sculpted surface with a complex, nonuniform curvature obtained by design of the laminate architecture. (a) Schematic of a flat laminate that is stretched at  $T_H$ . (b) After cooling to  $T_L$  and unloading, a desired complex, nonuniform curvature is achieved.

## 2.1.2 Continuum Mechanics PAC Model

Recently, Guo et al. [5, 6] developed a hyperelastic constitutive model for anisotropic fiber-reinforced composites, which treats both the matrix and fibers as neo-Hookean materials, and decomposes deformation into uniaxial deformation along the fiber and a subsequent shear deformation to estimate the strain energy. In the model, the strain energy stored in the composite system is:

$$W = \frac{1}{2} \mu_a (I_1 - 3) + \frac{1}{2} \mu_b (I_4 + I_4^{-1/2} - 3), \quad (2.1.2-1)$$

and the corresponding Cauchy stress is

$$\boldsymbol{\sigma} = -p\mathbf{I} + \underbrace{\mu_a \mathbf{B}}_{iso} + \underbrace{\mu_b (1 - I_4^{-3/2}) \mathbf{F} \mathbf{a}_0 \otimes \mathbf{F} \mathbf{a}_0}_{aniso}. \quad (2.1.2-2)$$

with  $\mu_a = \frac{(1-v_f)\mu_m + (1+v_f)\mu_f}{(1+v_f)\mu_m + (1-v_f)\mu_f} \mu_m$  and  $\mu_b = \frac{(\mu_f - \mu_m)^2 v_m v_f}{(1+v_f)\mu_m + (1-v_f)\mu_f}$ , where  $\mu_m$  and  $\mu_f$  are shear

moduli of the matrix and the fibers, respectively;  $v_m$  and  $v_f$  are volume fractions of the matrix and the fibers and  $v_m + v_f = 1$ . Here,  $\mathbf{F}$  is the deformation gradient  $\mathbf{F} = \partial \mathbf{x} / \partial \mathbf{X}$  where we use  $\mathbf{X}$  to represent the position of a material particle in the original (undeformed) configuration, while  $\mathbf{x}$  is the position of the corresponding particle in the current (deformed) configuration.  $\mathbf{B}$  is the left Cauchy-Green deformation gradient and  $\mathbf{B} = \mathbf{F} \mathbf{F}^T$ .  $\mathbf{C}$  is the right green Cauchy-Green deformation tensor and  $\mathbf{C} = \mathbf{F}^T \mathbf{F}$ .  $I_1$  and  $I_4$  are the principal invariants of  $\mathbf{C}$ :  $I_1 = \text{tr} \mathbf{C}$  and  $I_4 = \mathbf{a}_0 \cdot \mathbf{C} \cdot \mathbf{a}_0 = \lambda_F^2$ , where  $\mathbf{a}_0$  is a unit vector that represents the fiber orientation of the reinforced fiber in the original (undeformed) configuration and  $\lambda_F$  is the fiber stretch. In Eq. (2),  $p$  is an arbitrary hydrostatic pressure, the second term is associated with the isotropic part of the Cauchy stress and the third term is associated with the anisotropic part of the Cauchy stress. Figure 1c & d show the comparison between model simulations and experiments.

Based on Guo's model, we develop a thermomechanical constitutive model to describe the shape memory behavior of composites consisting of an elastomer matrix and glassy polymer fibers that pass through the glass transition during the temperature cycles. During a shape memory cycle, the model decomposes the total deformation  $\mathbf{F}$  into the thermal deformation  $\mathbf{F}_T$  and the mechanical deformation  $\mathbf{F}_M$ , that is,  $\mathbf{F} = \mathbf{F}_T \mathbf{F}_M$ . The thermal deformation,  $\mathbf{F}_T$ , is directly described by a simple model based on the observation of experiments. The mechanical deformation,  $\mathbf{F}_M$ , gives rise to the stress acting on the composite system. At high temperatures, fibers are in a rubbery state, and  $\mu_f$  is  $\mu_r$  (this value is measured by experiments). Therefore, at time  $t = t_0$  with a high temperature  $T = T_0$ , the Cauchy stress is

$$\boldsymbol{\sigma}_0 = -p\mathbf{I} + \mu_a|_{\mu_f(t=t_0)} \mathbf{F}_M^0 (\mathbf{F}_M^0)^T + \mu_b|_{\mu_f(t=t_0)} (1 - I_4^{-3/2}) \mathbf{F}_M^0 \mathbf{a}_0 \otimes \mathbf{F}_M^0 \mathbf{a}_0. \quad (2.1.2-3)$$

During glass transition, for the sake of model simplicity we make several assumptions and:



- i) We phenomenologically assume that the fibers can be described as an aggregate of rubbery and glassy phases, and the phase transition between these two phases is realized through the change of volume fraction of each phase [10].
- ii) The volume fraction of each phase ( $f_r$  for the rubbery phase and  $f_g$  for the glassy phase) as a function of temperature is defined as:

$$f_r = \frac{1}{1 + \exp[-(T - T_r)/A]}, \text{ and } f_g = 1 - f_r, \quad (2.1.2-4)$$

with a parameter  $A$  characterizing the width of the phase transition zone, and a reference temperature  $T_r$ .

- iii) During glass transition,  $\mu_f$  is simply described as  $\mu_f = f_r \mu_r + f_g \mu_g$  ( $\mu_g$  is also measured by experiments). As a result  $\mu_f$  varies from  $\mu_r$  to  $\mu_g$ , which leads to the change of  $\mu_a$  and  $\mu_b$  in Eq. (2), from  $\mu_a|_{\mu_f=\mu_r}$  ( $\mu_b|_{\mu_f=\mu_r}$ ) to  $\mu_a|_{\mu_f=\mu_g}$  ( $\mu_b|_{\mu_f=\mu_g}$ ).
- iv) We assume that the newly formed glassy phase is in a stress-free configuration and take this as its reference configuration for any subsequent deformation <sup>7</sup>.

Based on the assumption that the newly formed glassy phase is in a stress-free configuration, when we calculate the total Cauchy stress applied to the composite during glass transition, the increasing amounts of  $\mu_a$  and  $\mu_b$  is only associated with the deformation after the formation of the glassy phase resulting in the corresponding increase of  $\mu_a$  and  $\mu_b$ . Therefore, we obtain a general expression for the total Cauchy stress acting on the composite during glass transition, at time  $t = t_0 + n\Delta t$ , and  $T = T_0 + n\Delta T$ ,

$$\begin{aligned} \boldsymbol{\sigma}_n = & -p\mathbf{I} + \mu_{a,0} \mathbf{F}_M^n (\mathbf{F}_M^n)^T + \mu_{b,0} \left[ 1 - I_4(\mathbf{F}_M^n, \mathbf{a}_0)^{-3/2} \right] \mathbf{F}_M^n \mathbf{a}_0 \otimes \mathbf{F}_M^n \mathbf{a}_0 \\ & + \sum_{i=1}^n \left\{ \Delta\mu_{a,i} \mathbf{F}_M^{i \rightarrow n} (\mathbf{F}_M^{i \rightarrow n})^T + \Delta\mu_{b,i} \left[ 1 - I_4(\mathbf{F}_M^{i \rightarrow n}, \mathbf{a}_i)^{-3/2} \right] \mathbf{F}_M^{i \rightarrow n} \mathbf{a}_i \otimes \mathbf{F}_M^{i \rightarrow n} \mathbf{a}_i \right\}. \end{aligned} \quad (2.1.2-5)$$

In Eq. (2.1.2-5),  $\mu_{a(b)} = \mu_{a(b)}|_{\mu_f(t=t_0)}$ ,  $\Delta\mu_{a(b),i} = \mu_{a(b)}|_{\mu_f(t=t_0+i\Delta t)} - \mu_{a(b)}|_{\mu_f(t=t_0+(i-1)\Delta t)}$ ,  $\mathbf{F}_M^n = \left( \prod_{i=1}^n \Delta\mathbf{F}_M^i \right) \mathbf{F}_M^0$ ,  $\mathbf{F}_M^{i \rightarrow n}$

$= \left( \prod_{j=i}^n \Delta\mathbf{F}_M^j \right)$ ,  $\mathbf{a}_i = \frac{\mathbf{F}_M^{i-1} \mathbf{a}_0}{|\mathbf{F}_M^{i-1} \mathbf{a}_0|}$ , and,  $I_4(\mathbf{F}, \mathbf{a}) = \mathbf{F} \mathbf{a} \cdot \mathbf{F} \mathbf{a}$ .  $\mathbf{F}_M^0$  is the mechanical deformation before glass

transition, and  $\Delta\mathbf{F}_M^i$  is the incremental deformation at time  $t = t_0 + i\Delta t$ . Comparing model predictions and experiments showed good agreement; see Figure 2.1.1-2.

### 2.1.3 Origami by 4D Printing

We further extend the PAM concept to demonstrate how we can print flat-plate structures consisting of PAC hinges directly connected to rigid plastic components of arbitrary shape and then program the hinges to assemble the as-printed structure into a desired 3-D configuration. First we designed a box consisting of six sides connected by PAC hinges that is printed in a flat (unfolded) form as shown in Figure 2.1.3-1a. Specifically, we created hinges from PACs by following a theoretical study similar to the one in Section 2.1.2, and stretched the box biaxially by 20%. Figure 2.1.3-1a shows the as-printed box (the flat plate) where the rigid sides are white and the hinges are black. The assembled box was created after biaxially

stretching the as-printed structure by 20% at  $T_H$ , cooling to  $T_L$ , and releasing the load. It clearly assembles into the desired box shape (Figure 2.1.3-1b), with only small deviations from the desired 90°

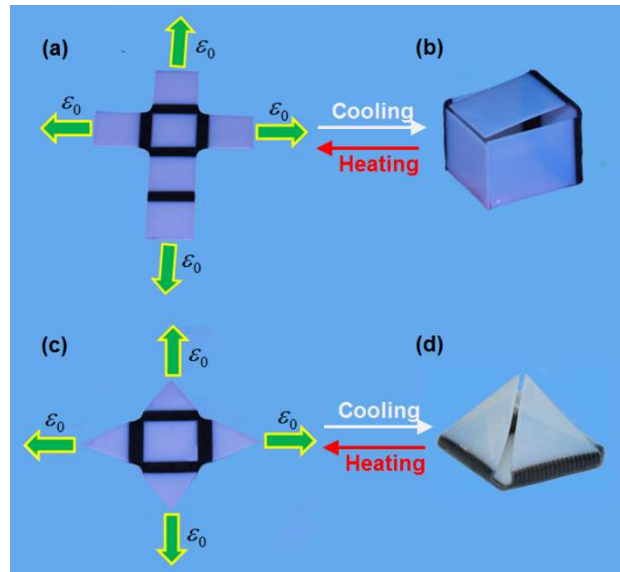


Figure 2.1.3-1. Active origami box and pyramid. The printed flat cross shape in (a) assembles itself into a desired box shape in (b) after the programming steps. The printed flat Ninja star shape plate in (c) assembles itself into a desired pyramid shape in (d) after the programming steps.

angles, and these are likely due to inaccuracies in the straining process. Figures 2.1.3-1c and d show a similar structure, a five-sided 3D pyramid. Here the printed flat Ninja star shape plate consists of a square base with four triangular sides (Figure 2.1.3-1c) that are folded to a 3D pyramids with 60° angles (Figure 2.1.3-1d).

We can also create complex 3D shapes with different hinge angles by printing hinges with different geometries. Figure 2.1.3-2a shows an example that a flat triangle sheet that folds itself into an origami airplane with a 0° angle in the middle hinge that bends upward and 90° angles in the two side hinges that bend downward. The hinges are created by printing the bilayer composites with the fibers on the top layer for the 0° hinges and on the bottom for the 90° hinges. To simplify the loading process (allowing simply a 20% stretch) we print the 90° hinges in Figure 2.1.3-2a at an inclined angle relative to the base of the plane, but we maintain the fiber orientations parallel to the base (and the applied stretch, Figure 2.1.3-2a inset). We create an even more sophisticated origami airplane by printing not only hinges with different lengths but also ones with different cross-section profiles (Figure 2.1.3-2c and d).

The use 3D printing of active materials to create components that controllably change their shape over time is not limited to the use of PAC hinges. In fact, we can directly print 3D devices by strategically placing shape memory polymers at pivotal locations or throughout an entire structure. We can then program a temporary shape of arbitrary form that can be achieved by applying a prescribed mechanical loading at  $T_H$  followed by releasing the constraints at  $T_L$ . The components can then be returned to their complex original 3D shapes after heating back to  $T_H$ . Figure 2.1.3-3 shows such an example. We directly printed a

3D box with a pattern of SUTD-CU logos on the five panels. In Figure 2.1.3-3a, the complete 3D box was printed with a three-layer laminate consisting of a Verowhite middle layer embedded in a Tangoblack

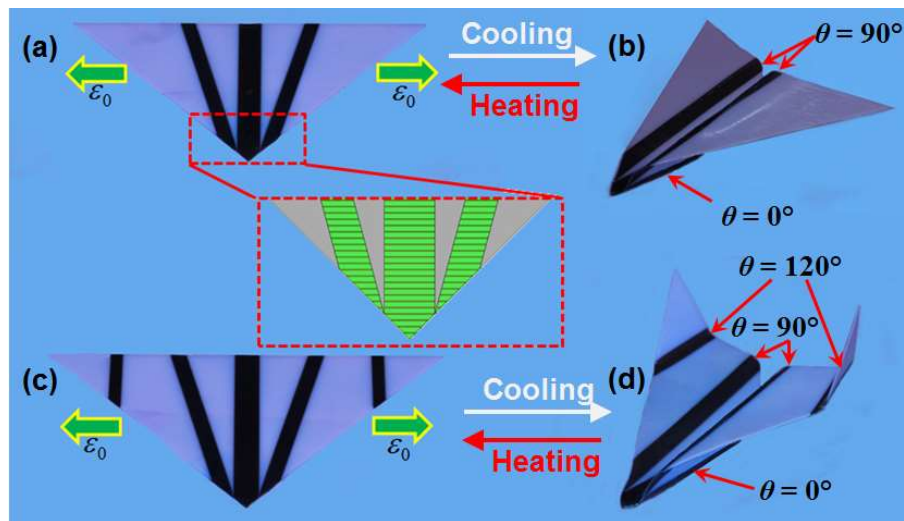


Figure 2.1.3-2. Active origami airplanes. A flat triangle sheet with three hinges in (a) assembles itself into an origami airplane with a  $0^\circ$  angle in the middle hinge that bends upward and  $90^\circ$  angles in the two side hinges that bend downward in (b). A flat triangle sheet with five hinges in (c) assembles itself into an origami airplane with two winglets in (d).

matrix. The box is then deformed to a flat form (Figure 2.1.3-3b) by applying mechanical loads at  $T_H$ , and cooled to  $T_L$  where the constraints were removed, leaving it in a flat form. Upon heating back to  $T_H$ , the structure retakes the original 3D box shape (Figure 2.1.3-3a).

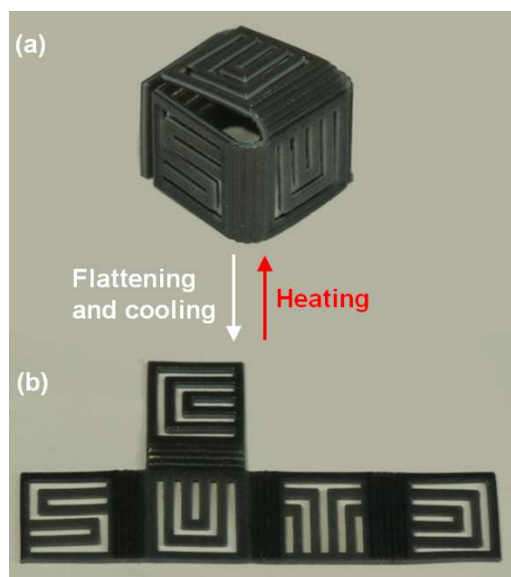


Figure 2.1.3-3. A directly-printed origami SUTD-CU box. An as-printed 3D SUTD-CU box in (a) was deformed into a flat form at  $T_L$  in (b). After heating back to  $T_H$ , the structure recovers the 3D box shape.

### 2.2.1 Sequential folding structures using digital shape memory polymers

In this work, we used digital SMPs with different thermomechanical properties to achieve different recovery speeds of the SMPs at the same recovery temperature; we then further exploited this feature to design complicated folding structures. This work was published in “Mao, Y., Yu, K., Isakov, M.S., Wu, J., Dunn, M.L., Qi, H.J., 2015. *Sequential Self-Folding Structures by 3D Printed Digital Shape Memory Polymers*, *Scientific Reports*, 5: 13616. doi:10.1038/srep13616.”

**Hinge Folding:** Hinges designed with digital SMPs with specified thermomechanical behaviors, especially recovery, are the key element of sequentially self-folding structures (shown in the inset of Figure 1a). We designed, fabricated, and tested hinges using seven different digital SMPs. We use H-i ( $i=1,2,3...7$ ) to represent the  $i$ -th hinge. The glass transition temperatures ( $T_g$ s) of these hinge materials are shown in Figure 1a. The shape memory behavior of the hinges, including shape fixity and shape recovery, is controlled by the applied mechanical and thermal-temporal programming and recovery conditions. To understand the basic hinge behavior we consider a hinge printed with an initial angle of  $\theta = 90^\circ$  and then programmed (by bending at  $T_H = 90^\circ\text{C}$ ) to assume a temporary flat state ( $\theta = 180^\circ$ ), which corresponds to a shape fixity of 100%. Then we recover the hinges to their original shape ( $\theta = 90^\circ$ ) by heating them in a constant temperature bath, during which we monitor the recovery of the hinges as a function of time. We quantify the shape recovery with the angular recovery ratio ( $R_r$ ):

$$R_r(t) = \frac{180^\circ - \theta(t)}{90^\circ}, \quad (2.2.1-1)$$

where  $\theta(t)$  is the time dependent angle (Figure 2.2.1-1a).

The time-dependent angular recovery of the bending hinges can be examined by using a simple scaling approach with respect to the uniaxial shape memory behavior, which is modeled by a multi-branch constitutive model<sup>43-45</sup> with 16 branches. Figure 1b shows the folding time at three different folding temperatures for the seven hinges by 1D model. Here, the folding time is defined as the time needed for a hinge to fold to  $\theta = 91.8^\circ$ , which corresponds to a recovery ratio of 98%. It can be seen that at the same folding temperature, hinges fabricated by lower  $T_g$  materials (the higher hinge numbers) need longer time to fold. The difference in the folding time provides the opportunity to design the sequencing of folding.

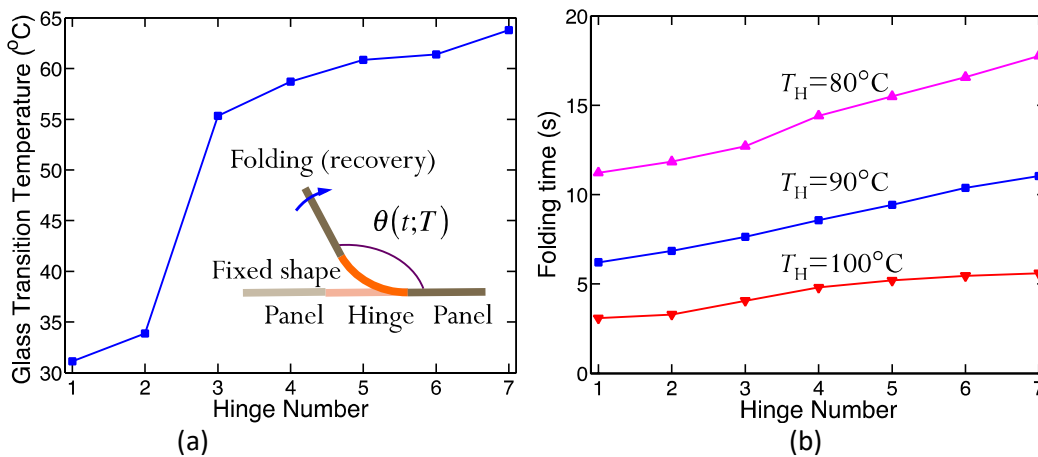


Figure 2.2.1-1. (a) Glass transition temperatures of the seven digital SMPs used for hinge materials; the inset shows a schematic view of the folding of an SMP hinge; (b) folding time of hinges to obtain 98% recovery ratio at various recovery temperatures.

**Sequential self-folding.** As the first example, we demonstrate a seemingly-simple helical structure where rigid (non-active) panels are connected by active hinges on each corner with a radius of 5mm (Figure 2.2.1-2a). The thickness of the panels and hinges is 0.8mm, the depth is 6mm and the clearance between neighboring panels is 5mm. We design two structures that have identical geometry, but each has a different set of materials used for the hinges. In Sample 1 each of the 9 hinges uses the same SMP material (H-3), and in Sample 2 the hinges are made from seven different materials (H1-H7; Table 2.2.1-1). After printing the structure, we deform it into a flat configuration in hot water at  $T_H=90\text{ }^{\circ}\text{C}$ , which is above the  $T_g$  of all of the SMP sections. Then the sample is cooled to  $T_L=10\text{ }^{\circ}\text{C}$ , at which all the SMP hinges are in their glassy states. After releasing the external load, the structure is fixed at the temporary straight shape. To activate the shape recovery of the structure, we immerse it in hot water with  $T_r=90\text{ }^{\circ}\text{C}$  so that all hinges experience the same thermal conditions. The shape recovery process is monitored by a video camera.

Figure 2.2.1-2b shows the recovery sequence of Sample 1. Since all the hinges possess the same thermomechanical behavior ( $H_3$  with  $T_g \approx 55\text{ }^{\circ}\text{C}$ ), they start to recover their shape simultaneously. The uncoordinated and simultaneous motions of all hinges lead to two undesirable results. First, at  $\sim 7.5\text{ s}$  parts of the structure collide with each other because of folding pathway interference. The contact between different parts of the structure provides frictional resistance and leads to a significant reduction of folding speed. Second, at  $12.5\text{ s}$ , the frictional force becomes so large that folding stops and the structure fails to reach its final target shape.

Table 2.2.1-1 Hinge assignment of each fold

Fold Number		1	2	3	4	5	6	7	8	9
Material	Sample 1	H-3	H-3	H-3	H-3	H-3	H-3	H-3	H-3	H-3
	Sample 2	H-1	H-1	H-2	H-3	H-4	H-5	H-6	H-7	H-7

For the structure shown in Figure 2.2.1-2a, in order to recover its final target shape, the inner hinges require faster folding speeds than those of the outer hinges, which can be accomplished by assigning SMPs with lower  $T_g$ s. To this end we designed hinges unique to each corner as (see Case 2 in Table 2.2.1-1). After experiencing the same programming procedure as described in the previous section, the structure is immersed in hot water at  $T_H=90\text{ }^{\circ}\text{C}$  and the free recovery process is monitored. Figure 2.2.1-2c shows the snapshots at different recovery times, which visually demonstrates the sequential recovery of hinges to yield unconstrained and rapid ( $\sim 7.0\text{ s}$ ) folding to the target configuration as shown in Figure 2.2.1-2c.

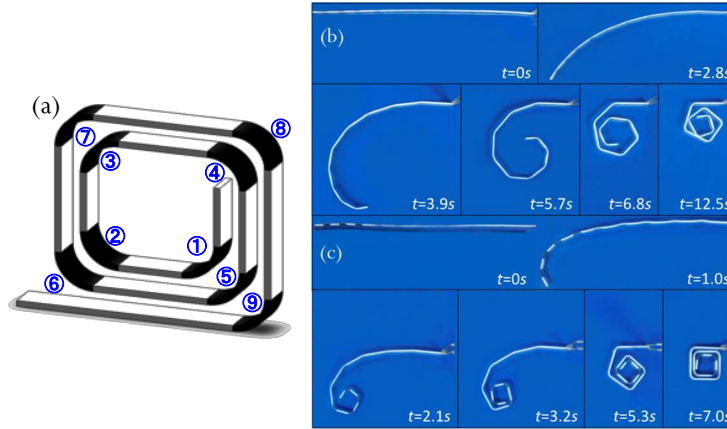


Figure 2.2.1-2. Schematic of the helical SMP component (a). Series of photographs showing the shape recovery process of the helical SMP component with uniform hinge section (b), and with graded hinge sections(c).

The different folding speeds of the hinge sections due to their respective  $T_g$ s enable the avoidance of self-collisions. Since the folding speeds of the three inner hinges are faster than the outside ones, they first exhibit shape recovery (they start the shape recovery within  $\sim 1$ s and finish in  $\sim 3$ s). Then shape change is successively triggered along the helical line and the last two hinges start to recover after 3s and finish at  $\sim 7.0$ s. The hierarchical shape recovery profiles of the hinge sections enable the successful sequential shape recovery in the SMP component without interruption by collisions.

The above two cases demonstrate the importance of design and the ability to control the assembly sequence and dynamics by the spatial arrangement of SMPs with varying thermomechanical behavior. A “bad” design without careful coordination of different folding panels can lead to slower and even failed folding of the entire structure.

**Folding simulations: finite element analysis and reduced-order model.** To describe both unfolding and folding behaviors and use this understanding in current design, we take a two-stage approach for analysis. First, we simulate the folding dynamics using finite element analysis (FEA). FEA provides high-fidelity simulation of the spatial and temporal variation of the programming (unfolding) and deployment (folding) processes. However, it is also time-consuming as it involves complicated contact (used for unfolding) as well as nonlinear geometrical mechanics. Second, we develop a reduced-order model (ROM) to simulate rigid body motions of the panels (driven by the recovery of angular shape recovery of hinges) to investigate the folding pathways. During folding and unfolding the deformation is mainly localized in the hinges so in the ROM we idealize the structure as rigid panels connected by hinges with rotational behavior given by our constitutive model.

For ROM, we use the scaling rule demonstrated above to predict the shape recovery ratio of hinge by the recovery behavior of a sample under linear stretch. Here, we assume that the folding structure can be represented by rigid panels connected by hinges, which occupy infinitesimal space but control the angles between two panels. Figure 2.2.1-3 shows panels are connected by hinges, which are represented by  $P_i$  with its coordinates of  $(x_i, y_i)$  for the  $i$ -th hinge. In the ROM, we assume that the angular rotation of the hinge is equal to the linear recovery ratio of a SMP. This assumption is validated in the above sections. Following Eq. 2.2.1-1, we have

$$\theta_i(t) = 180^\circ - 90^\circ R_r^i(t), \quad (2.2.1-2)$$

where  $\theta_i(t)$  is the angle between the  $i$ -th panel and  $(i+1)$ -th panel,  $R_r^i(t)$  is the recovery ratio of the  $i$ -th

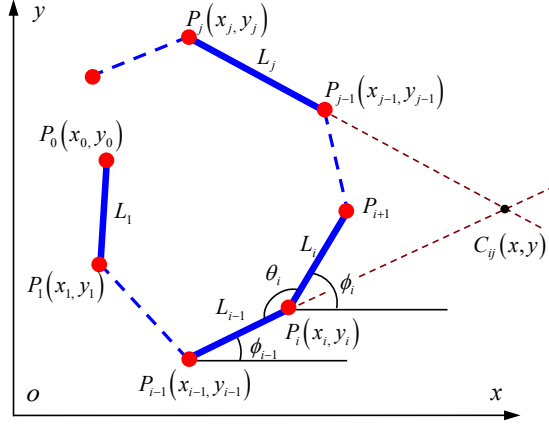


Figure 2.2.1-3. Schematic of two arbitrary strips having a factitious intersection point

hinge, which is between the  $i$ -th and  $(i+1)$ -th panels. In order to calculate the location of the hinges, the orientation of the  $i$ -th panel is calculated as

$$\phi_i(t) = \phi_{i-1}(t) + \theta_i(t), \quad (2.2.1-3)$$

where  $\phi_i(t)$  is the orientation of  $i$ -th panel. Finally, the coordinates of the  $i$ -th hinges are

$$x_i(t) = x_0 + \sum_{i=1}^i l_i \cos[\phi_i(t)], \quad y_i(t) = y_0 + \sum_{i=1}^i l_i \sin[\phi_i(t)], \quad (2.2.1-4)$$

where  $l_i$  is the length of the  $i$ -th panel.

In ROM simulations, at each time increment, the coordinates of individual hinge points are first calculated; the intersections points and the intersection indices are calculated. If  $0 < S_{ij} < 1$ , the above three conditions will be checked; if any one of them is satisfied, there is no intersection; otherwise, an intersection exists and folding cannot be completed.

Figure 2.2.1-4a shows finite element simulations of the folding and unfolding processes. In the unfolding process, the structure is opened by rigid surfaces to successively unfold one panel after the other at a high temperature. After lowering the temperature and unloading, the structure is fixed into the flat configuration. Recovery is achieved by heating the structure uniformly and it folds into the original configuration. The simulated recovery ratios for representative hinges (H-1, H-4, and H-7) are presented in Figure 2.2.1-4b along with measurements and results from the ROM. Both FEA and ROM predictions are in good agreement with experimental measurement. Figures 2.2.1-4c and 2.2.1-4d show ROM simulations of the two samples in Table 2.2.1-1. They describe both the unsuccessful (Fig. 2.2.1-4c) and successful (Fig. 2.2.1-4d) folding sequences well. Importantly the ROM captures the self-collisions that occur during the failed folding; based on this capability, we use it to design more complex folding scenarios in the next section.

**Collision determination.** Utilizing the ROM simulation, we develop a simple *collision index*, which can be used to determine if two panels will collide during the folding process. We consider two arbitrary panels in the structure (as shown in Figure 2.2.1-3), denoted as  $L_i, L_j$ , with coordinates of points as  $P_j^{(1)}(x_j^{(2)}, y_j^{(2)}), P_j^{(2)}(x_j^{(2)}, y_j^{(2)})$ , respectively. The parametric equation for the  $i$ -th panel (denoted as a solid line) is given as



$$\frac{y - y_i^{(1)}}{y_i^{(2)} - y_i^{(1)}} = \frac{x - x_i^{(1)}}{x_i^{(2)} - x_i^{(1)}} = S, \quad (2.2.1-5)$$

where  $S$  is a parameter that is the distance from point  $i$  to point  $(x,y)$  normalized by the length of the panel. Therefore, for the point  $(x,y)$  on the panel,  $0 \leq S < 1$ . By using the parametric equations of the  $i$ -th panel and the  $j$ -th panel, the coordinates of the intersection between these two panels can be calculated as  $C_{ij}(x_{ij}, y_{ij})$ . Substituting the coordinate of intersection point  $(C_{ij}(x_{ij}, y_{ij}))$  into the  $i$ -th line equation (Eq. (2.2.1-2)) yields a parametric index  $S_i$ . When  $0 \leq S_i \leq 1$ , the intersection point is on the  $i$ -th panel, while when  $S_i > 1$  or  $S_i < 0$  the intersection point sits on the extension line of the  $i$ -th panel. The same is true for parametric index,  $S_j$ , for the  $j$ -th panel. It is thus easy to conclude that when the two panels intersect, we have  $0 \leq S_i \leq 1$  and  $0 \leq S_j \leq 1$ ; otherwise there is no intersection.

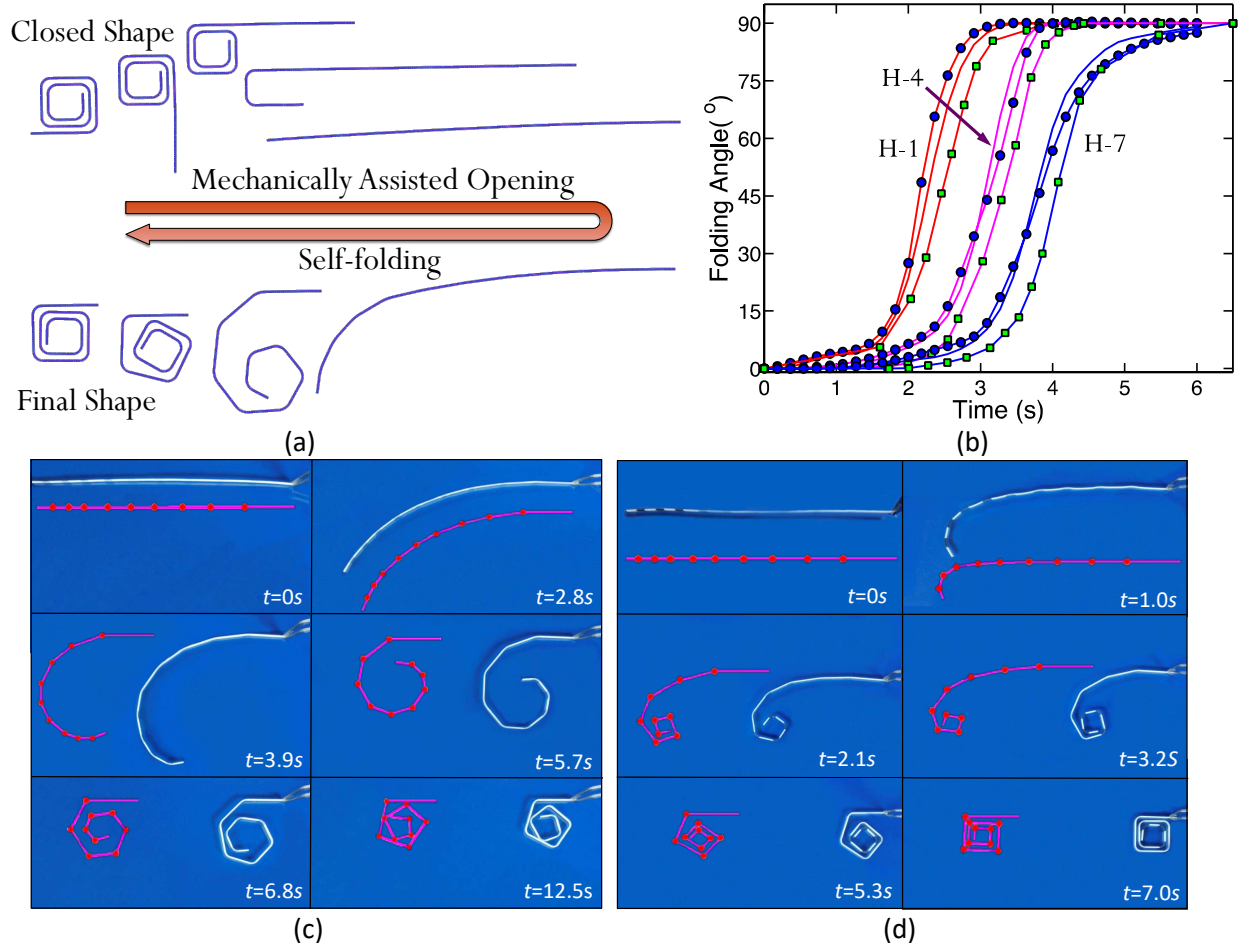


Figure 2.2.1-4. (a) Finite element simulation of shape memory recovery activated sequential self-folding when the strip is firstly programmed at high temperature. (b) Simulation of folding angles of three representative hinges by ROM and compared with that by FEA and experiments. Solid-line only: FEA; round dot: ROM; square: experiments. Red color: H-1; magenta color: H-4; Blue color: H-7. Comparison between ROM simulations and experiments for Sample 1(c) and 2 (d), where red lines indicate the simulation results.



We further define an interaction index for intersection of line  $i$  and line  $j$  as

$$S_{ij} = S_i \times S_j . \quad (2.2.1-6)$$

In general, when  $0 < S_{ij} < 1$ , intersection occurs. However, three cases that can give  $0 < S_{ij} < 1$  but no intersection: (1)  $0 < S_i < 1$  and  $S_j > 1$  (for example,  $S_j$  is slightly larger than 1); (2)  $0 < S_j < 1$  and  $S_i > 1$  (for example,  $S_i$  is slightly larger than 1); (3)  $S_i < 0$  and  $S_j < 0$ . As described in the Methods section, the collision index,  $S_{ij}$ , is calculated based on the motion of any pair of panels (the  $i$ -th panel and the  $j$ -th panel) during each time increment of the simulation. In general, when  $0 < S_{ij} < 1$ , a collision will occur. Figures 2.2.1-5a and 2.2.1-5b show the collision indices of the two designs discussed above; there are 10 panels in each design which gives rise to 40 unique panel pairs. In Figure 2.2.1-5a, the structure can fold without collisions, therefore, no collision index falls between the band between 0 and 1 during the simulation. In Figure 2.2.1-2c two collisions occurred between panels and the structure cannot fold to its target shape; Figure 2.2.1-5b reflects this as two collision indices fall in span(0,1). In the figure, the red dot between (0,1) corresponds to first collision; the blue dot corresponds to the second collision. More collision will happen; but since our interest is the first collision, no further calculation was conducted.

**A self-locking system.** Here we use our ROM to design and then 3D print a self-folding and self-locking structure, as shown in Figure 6a. Here, two holes with different dimensions are designed on one of the end panels. The objective is to sequentially guide the other end of the structure through the first hole and then through the second hole to lock the structure in place. Five hinges (with a radius of 5mm in uniform) are used. In order to ensure that the end of the strip passes through the two holes in sequence, we design each hinge to control the folding rate of each segment of the structure. This results in two requirements: First, the folding of hinges 1 and 2 should be faster than the others so that the two end sides reach each other in the correct position and angle. Second, folding of hinges 4 and 5 should be slower to guarantee them to pass through the two holes successively and then lock the structure. Using our ROM simulations with the collision index, we determined feasible folding rates for each hinge, and then realized them with hinges. Specifically, we assigned hinges H-2, H-2, H-3, H-6 and H-6 for hinges 1 to 5 in Fig. 6a. The self-folding and self-locking structure is demonstrated experimentally in Fig. 5. The structure shown in Figure 2.2.1-6a is first printed. At the temperature of 90 °C, it is opened into a flat strip, or namely the unlocked configuration. It is then cooled to 10 °C where the flat shape is maintained. After this programming step, the unlocked structure is immersed in hot water (90 °C) and the free recovery process is shown in the snapshots of Figure 2.2.1-6d. The insets show the ROM simulated folding and locking procedure. As predicted by ROM, the active locking side is able to pass through the two holes successively, and finally recovers to the initial configuration as shown in Figure 2.2.1-6c. The ROM simulation and the experiment show good agreement.

**A 3D folding structure.** Folding boxes are notable folding structures in daily life and widely used in packaging. They normally require a folding sequence in order to form a stable and fully packed structure. Taking a USPS mailbox (Figure 2.2.1-7a) as an example, one can take a sheet of hard board paper cut into a specific shape. One folds the box in a sequential manner; the red lines represent the first group of folds, where some lips are folded to form supports; the blue lines represent the second group of folds to partially close the box; the final folds (black lines) insert the two small lids (on the left top and bottom) into the

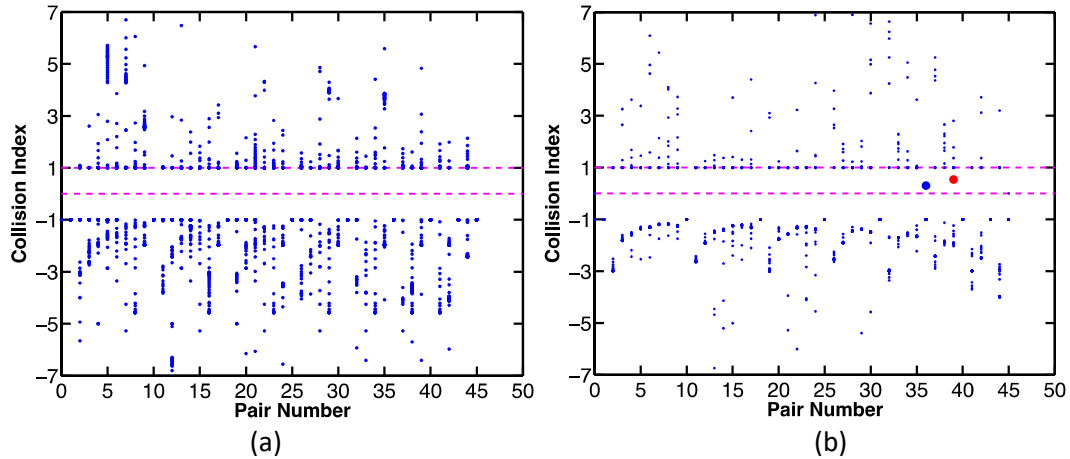


Figure 2.2.1-5. The self sequential self-folding (a) without collisions; (b) with collisions. When there is no collision, all collision indices are out of span (0,1)(shown in (a)), and when there is a collision, the index falls in span (0, 1) (as shown in (b), two points (a red and a blue point) are in span (0,1)). The red dot between (0,1) corresponds to first collision; the blue dot corresponds to the second collision.

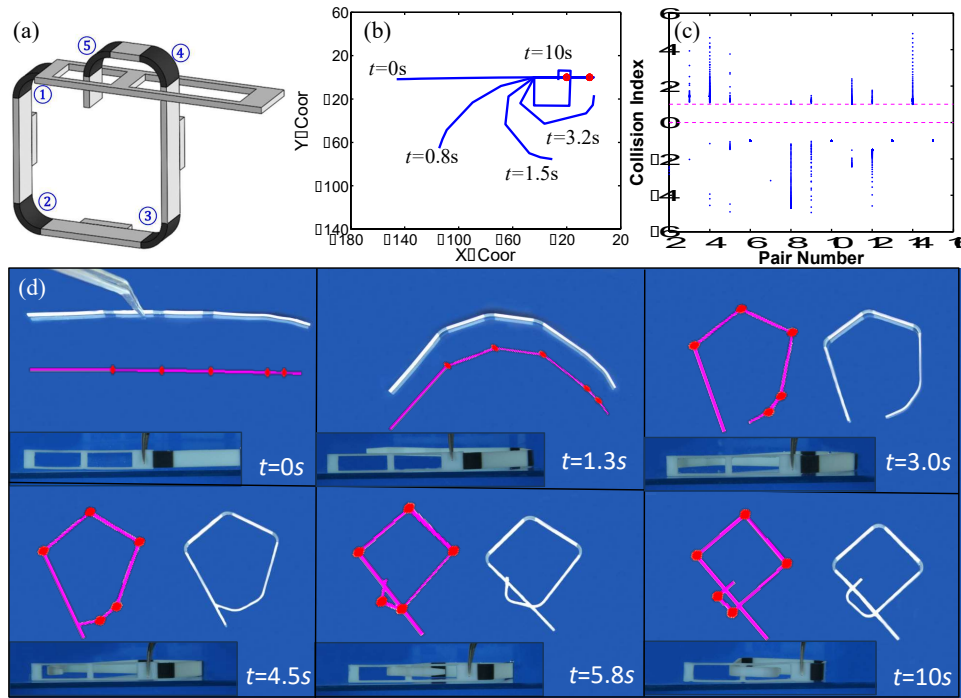


Figure 2.2.1-6. Schematic of the interlocking SMP component (a). ROM simulation of the sequential folding resulting in interlocking (b), the collision indices of the chosen design (c), and a comparison of experiments (plan and side views) and the ROM simulations (red lines) (d).

holes formed by the long blue line folds to increase the stability of the box. Inspired by this, we designed a 3D folding box with an internal locking mechanism, as shown in Figure 2.2.1-7b. Three types of hinges were used. Hinge H-3 is used on the smaller lips to enable fast folding of these lips (red lines). Hinge H-5 is used in the location indicated by the green line, to enable intermediate folding speeds such that some self-support and self-locking mechanism can be formed. Hinge H-6 (black lines) has the slowest folding speed and is used to form the final structure. The original shape of the box is shown in Figure 2.2.1-7c.

Since curved portions of the hinges are not in the printing plane, these hinges are suspect to damage during unfolding. To improve the damage tolerance, hinges are specially designed (Figure 2.2.1-7d-f). A periodic step profile was employed along the surface contour of the hinge (Figure 2.2.1-7d). Thinner stepwise sections require lower bending stress and have higher thermal conductivity, making it both easier and faster to unfold complex assemblies. To secure the interface between hinges and structural faces, the hinges were embedded within the structural faces and reinforced with a triangular interface to maximize axial strength (Figure 2.2.1-7e). Longer hinges were equipped with slots cut along the length of the jagged contours to isolate fracture points should a fracture occur (Figure 2.2.1-7f). Figures 2.2.1-7g-j shows the folding sequence. The whole structure folds back in about 11 seconds.

### 2.3.1 Multiple shape change printed active composites

In this work, we demonstrate the design and manufacture of active composites that can take multiple shapes, depending on the environmental temperature. This is achieved by 3D printing layered composite structures with multiple families of shape memory polymer (SMP) fibers – digital SMPs - with different glass transition temperatures ( $T_g$ ) to control the transformation of the structure. After a simple single-step thermomechanical programming process, the fiber families can be sequentially activated to bend when the temperature is increased. By tuning the volume fraction of the fibers, bending deformation can

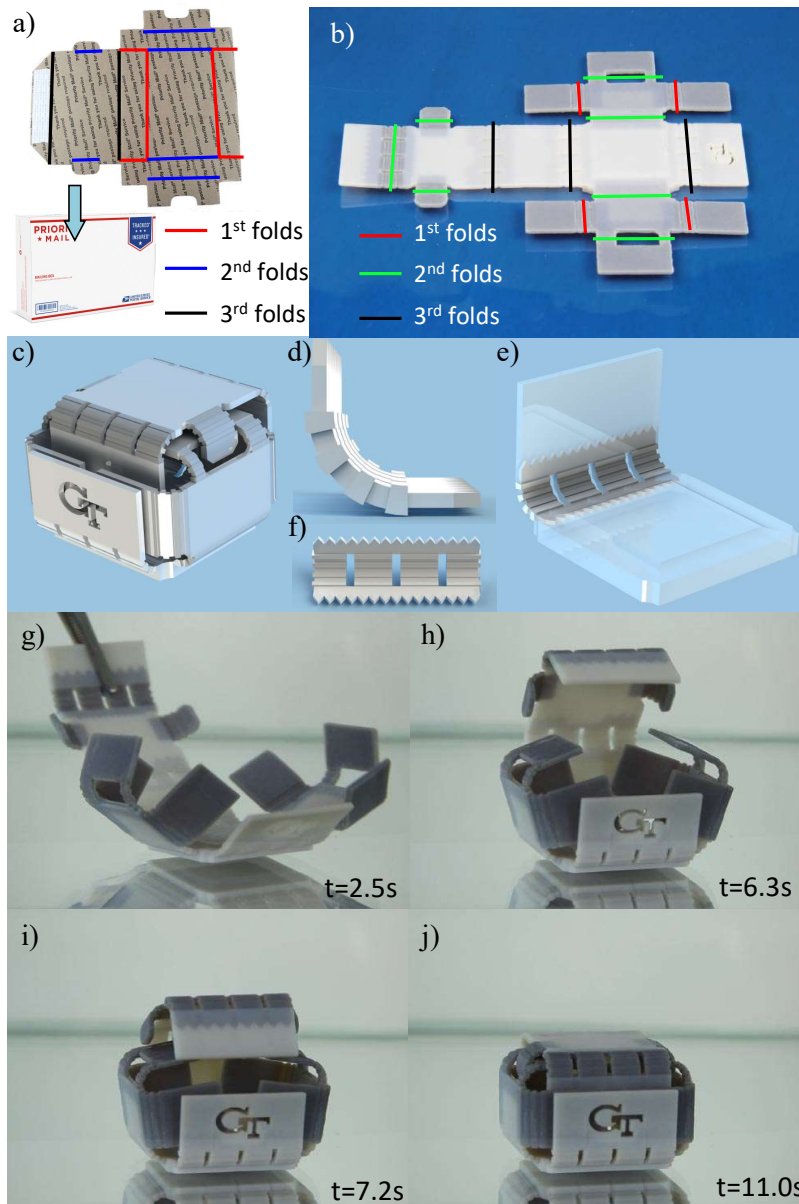


Figure 2.2.1-7. 3D folding structures mimicking the USPS mailbox. (a) A USPS mailbox is folded into a box by following a sequence of folding; b) a programmed 3D printed sheet with different materials assigned at different hinges; c-f) design of the folding box with some details at the hinges. g-j) upon heating, the sheet folds into a box with self-locking mechanism.

be controlled. We also develop a theoretical model to predict the deformation behavior for better understanding the phenomena and aiding the design. This work is in the manuscript “Wu, J., Yuan, C., Ding, Z., Isakov, M., Mao, Y., Wang, T., Dunn, M.L., Qi, H.J. 2016. Multi-shape active composites by 3D printing of digital shape memory polymers *Scientific Reports* 6, Article number: 24224”. More details can also be found in this manuscript.

**Design concepts.** The composites in this study consist of three materials with different glass transition temperatures ( $T_g$ s) and are part of the material library of our multi-material 3D printer (Objet260 Connex, Stratasys Inc, Edina, MN, USA). Figure 2.3.1-1a shows the design of a two-layer composite. The matrix is

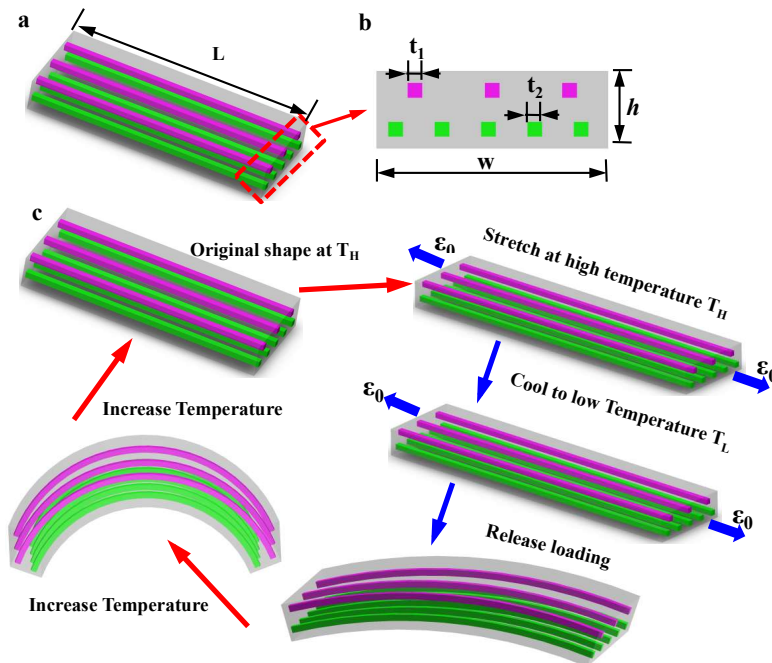


Figure 2.3.1-1. Schematics of the printed SMP composite design. (a) The design of the two layer SMP composite strips and the characterization of the design. The purple color represents the fiber with higher  $T_g$  and the green color represents the fiber with lower  $T_g$ . (b) The typical programming steps for SMPs and desired response.

TangoBlack+, which has the lowest  $T_g$  ( $\sim 2^\circ\text{C}$ ) of the three materials. Two families of digital SMP fibers with different  $T_g$ s are embedded in the two layers, respectively, with prescribed volume fractions. The fibers (fiber 1: DM8530,  $T_g \sim 58^\circ\text{C}$ ; fiber 2: DM9895,  $T_g \sim 40^\circ\text{C}$ ), have shape memory effects in the temperature range between  $\sim 20^\circ\text{C}$  and  $\sim 70^\circ\text{C}$ . The thermomechanical programming steps are shown in Figure 2.3.1-1c. We first stretch the composite strip at an elevated programming temperature  $T_H$ , which is higher than  $T_g$ s of both fibers, to a prescribed strain ( $\epsilon_0$ ), and then cool it to the low temperature  $0^\circ\text{C}$  ( $T_L$ , which is lower than  $T_g$ s of both fiber materials) while maintaining the strain  $\epsilon_0$ . The applied strain is then released, which fixes the composite in the first temporary shape. Upon heating, the strip gains the ability to deform due to the temperature dependent viscoelastic properties of the matrix and fibers; the amount of deformation depends on the thermomechanical properties of the fibers and the matrix, the programming strain and the ambient temperature. If we heat the sample to a temperature that is higher than the  $T_g$  of the matrix but lower than that of the fibers, the sample is able to change to a second temporary shape. Due to the long stress relaxation time of the fibers at low temperatures, we are able to obtain a series of temporary shapes with different bending curvatures if we increase the temperature in a staggered manner. If we heat the sample to the temperature higher than the  $T_g$ s of both fibers, it will recover the flat permanent shape.

**The shape memory behavior of the SMP composite strip.** To demonstrate the multi-shape memory effects of the 3D printed SMP composites, we print the active composite strip by following the design concept illustrated above. Here, the strip is 70mm long, 6mm wide, and 2mm thick, with the fiber dimensions of  $a=b=0.38\text{mm}$  (Figure 2.3.1-2a). The fibers are placed at the center of each layer, i.e., the center of fiber 1 is 0.5mm from the top surface and the center of fiber 2 is 0.5mm from the bottom surface. The fibers are uniformly spaced at 0.5mm (fiber center to fiber center) to give volume fractions of 14% for either fiber 1 or fiber 2. In order to facilitate the stretching of the sample, two handles are directly

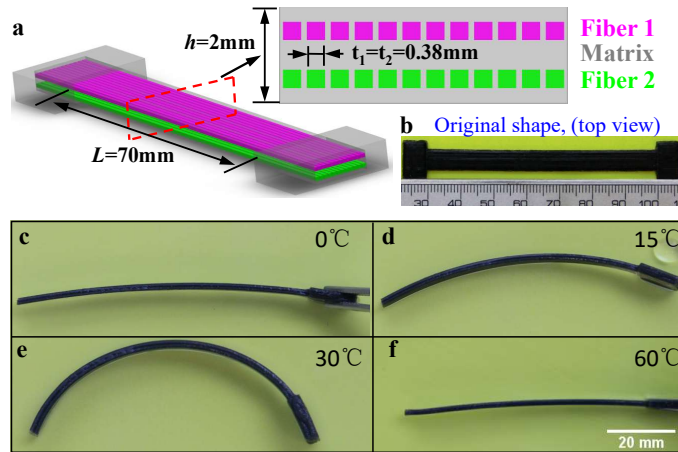


Figure 2.3.1-2. Multi-shape memory effects of a printed active composite strip. (a) The design and dimensions of the sample. The enlarged drawing is the cross section of the structure. (b) The original printed sample. The length scale in the bottom is in mm. (c) - (f) Shape change of the sample at different temperature.

printed at the ends of the sample, and one handle is cut off before reheating. The printed sample is first stretched at high temperature  $T_H=70^\circ\text{C}$  with strain of 10%, then cooled in cold water of  $\sim 2^\circ\text{C}$ , while the loading strain is kept. After the sample is fully cooled down, the strain loading is released. Then the sample is stepwise heated in water with three different temperatures ( $15^\circ\text{C}$ ,  $30^\circ\text{C}$ ,  $60^\circ\text{C}$ ) to demonstrate the shape recovery process. Figure 2.3.1-2b shows the top view of the original printed sample. Figures 2.3.1-2c-f show the shape memory effects of the sample. Figure 2.3.1-2c is the temporary shape of the sample at 2s after programming. After programming the sample bends slightly towards the side that contains fibers with lower  $T_g$ . When we cool for one minute at the temperature of  $15^\circ\text{C}$ , which is lower than the  $T_g$  of fiber 2, the sample bends more to form a new temporary shape (Figure 2.3.1-2d). After that, we heat the sample in  $30^\circ\text{C}$  water for 1 min.

Figure 2.3.1-2e shows the new temporary shape of the sample. Comparing the bending angles of the sample in Figure 2.3.1-2d and Figure 2.3.1-2e, we can see the shape of the sample changes slightly although the temperature is higher than the  $T_g$  of fiber 2. Finally, we heat the strip to  $60^\circ\text{C}$  and the sample recovers its original flat shape (Figure 2.3.1-2f). The sequence of transformations of the 3D printed SMP composites indicates that we can achieve multiple shapes using convenient 3D printing technology with a programming process that consists of a single simple step. In addition, Figure 2.3.1-2 shows a distinct feature of the new design: unlike conventional SME in polymers where the shape change is simply from one to another; here, a simple stretch can create multiple shape changes, i.e. it folds (bends) first, then unfolds (unbends) to become straight.

To further investigate the shape recovery process and speed of the printed active composite (PAC) strip, we directly heat the sample under hot water to prescribed temperature of  $T_H=70^\circ\text{C}$ . The bending behavior of the sample can be described by the variation of the bending curvature. Figures 2.3.1-3a-f show the deformation behavior of the sample at different times. The curvature of the sample as a function of the time in hot water is plotted in Figure 2.3.1-3g. It is clear that the curvature first increases when the strip begins to form the new temporary shape and then decreases when the sample begins to recover to its permanent shape after the temperature rises higher than the  $T_g$ s of both fibers. Note that the whole recovery time is only 12 seconds, indicating the fast response speed of shape change.



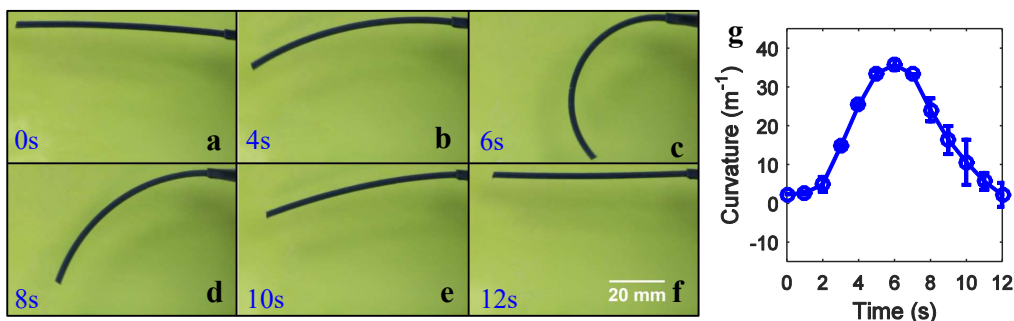


Figure 2.3.1-3. Bending actuation of the printed active composite strip during the recovery process. (a-f) Snapshots of the sample bending at different times. All six images are the side view of the sample. (g) Variation of the bending curvature during the recovery process.

**Theoretical prediction of multi-shape memory behavior.** In order to better understand the deformation behavior of the SMP composites, a theoretical model is developed that can be used to design SMP composites. In this model, the bending behavior of the composite strip is described using classical laminate theory, and a multi-branch model is used to describe the viscoelastic mechanical behavior of the matrix and fibers. Since the recovery speed is relatively fast, the heat transfer problem is considered to capture the non-uniform temperature distribution in the sample during the heating process. Using the theoretical model, we can predict the deformation behavior of the SMP composites. The curvature variation of the SMP composites strip is calculated as a function of the heating time. Figure 2.3.1-4a shows the comparison of the experimental and theoretical results of the curvature variation of the PAC sample during the heating process. Overall, the model captures the variation of the sample's curvature during the recovery and confirms the qualitative explanation of the operant phenomena of the preceding section. The model predicts a recovery that is about 1-2 seconds faster; this might be because the strip recovers in water, which may provide some resistance to the recovery motion.

The theoretical model provides an effective tool to help design the printed active composites. For example, the programming strain influences the residual strain or stress stored in the programmed PACs. Using the same dimensions of the composite shown in Figure 2.3.1-4a, we vary the prescribed strain and measure the curvatures of the sample in the recovery procedure. The length of the sample  $L=70\text{mm}$  and the programming temperature  $T_H=70^\circ\text{C}$ ,  $T_L=0^\circ\text{C}$ . Figure 2.3.1-4b shows the initial curvature and the maximum curvature of the PAC as a function of the pre-stretch strain, using values from both experiments and theoretical predictions. It is clear that the curvature increases with the pre-stretch because the residual mismatch strain, which is the driving force of the bending, increases with the programming strain. The effects of the volume fraction of the fibers are investigated by experiments and simulations. We vary the number of fibers in fiber family 1 (which has the higher  $T_g$  (in purple color)) to vary the volume fraction from 14.4% to 7.22%, 3.61% and 2.4%. Comparison between the experimental results and theoretical predictions of the initial and maximum curvatures are plotted as a function of the volume fraction of the fiber with higher  $T_g$  in Figure 2.3.1-4c, which shows that when the volume fraction increases the maximum curvature will increase monotonously; however, the initial curvature is nearly unchanged.

**Printing self-folding and self-opening structures.** As described above, by tuning the volume fraction of fibers and the prescribed strain, the bending of the SMP composites can be controlled. Here we show an example of self-folding and opening structures that exploit this phenomenon and our understanding of it. More examples can be found in the manuscript.

We first design a self-assembling and disassembling trestle. Figure 2.3.1-5a shows the design of the trestle, which has 4 identical active composite strips connected at the center. Figure 2.3.1-5b shows the cross-section of the composite strip. Every strip has one fiber with higher  $T_g$  (fiber 1) and twelve fibers

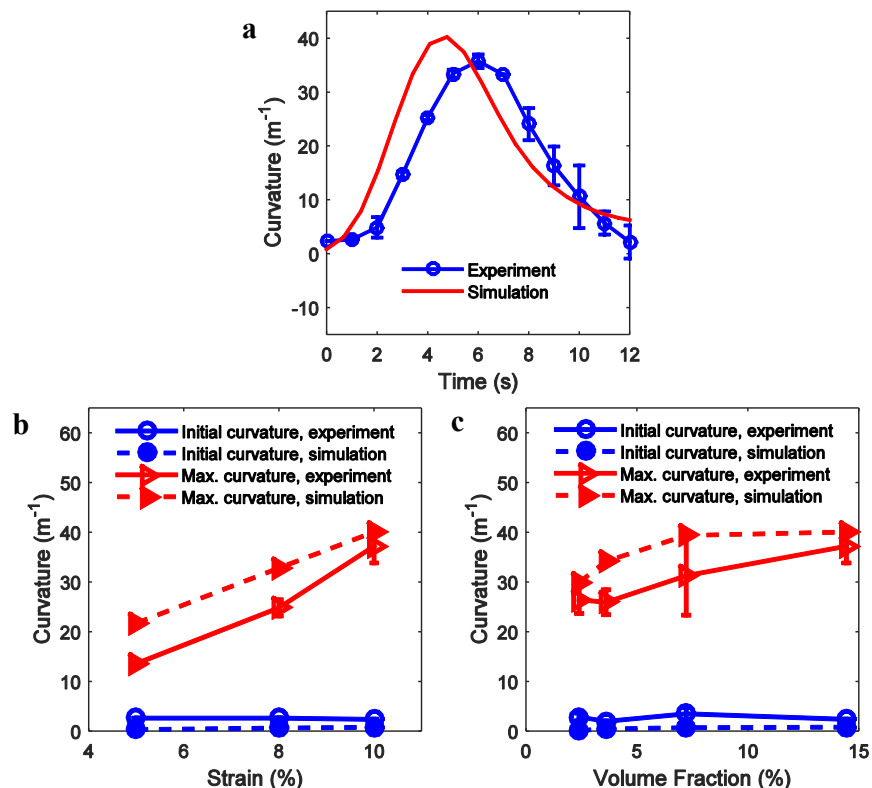


Figure 2.3.1-4. Comparison of the curvatures between experiments and theoretical model. (a) Bending curvature of the SMP composite vs heating time. (b) Effects of the programming strain and (c) the volume fraction of fibers on the initial and maximum curvature.

with lower  $T_g$  (fiber 2) and the dimensions of the strip are 55mm(length) by 6mm(width) by 2mm(thickness). The volume fractions of fiber 1 and fiber 2 are 1.2% and 14.4% respectively. The structure is stretched with a strain of 8% at 70°C then cooled to 0°C. After releasing at the low temperature, the sample bends slightly with a small curvature, as shown in Figure 2.3.1-5c. When heated, the strips fold and the trestle stands up from the flat shape as shown in Figures 2.3.1-5d-f. If we continue heating the sample, the trestle goes back to its flat shape (Figure 2.3.1-5g). This design can be used as an active supporting trestle controlled by external heating.

Using 3D printing technology to print shape memory polymers provides an easy and efficient way to manufacture active structures, and of course it can be used to create complex shapes tailored for specific applications. Here we further demonstrate one example: a smart hook (Figure 2.3.1-6). In this design, two 3D printed composites strips are connected at the ends. After being stretched with 10% strain, cooled to 0°C and relaxed under 0°C water for 1 min, one end handle of the structure is cut off. Then the nearly flat sample can be used as a hook to lift a small box. We first put the sample into hot water with temperature of 30°C and the straight sample bends to form two half circular shapes (Figure 2.3.1-6b-c). Using the two half circular shapes, we can lift up a small basket from water (Figure 2.3.1-6e). To release the box into another position, we increase the temperature of the sample to be higher than the  $T_g$ s of the fibers (Figure 2.3.1-6f-h). From these simple designs, we can see the great potential of using the 3D printed active materials in creating smart structures that can deform on demand by controlling the environment temperature.



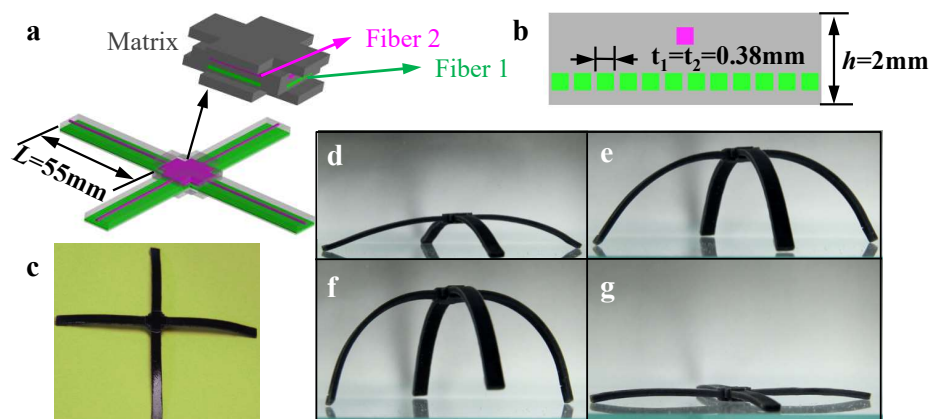


Figure 2.3.1-5. Self-assembling and disassembling trestle. (a) The design of the trestle. (b) The cross section of the composites strip. (c) The shape of the structure after programming. (d)-(g) The deformation behavior of the structure in the recovery process.

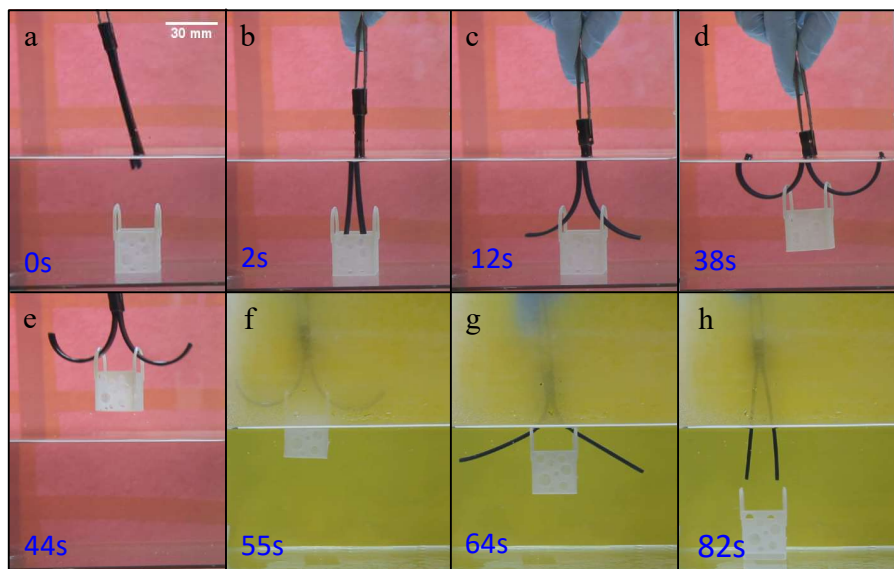


Figure 2.3.1-6. Smart hook. (a)The programmed hook. (b)-(c)The bending deformation of the structure under hot water with temperature of 30°C. (d)-(e) A small box is lifted up from water. (g)-(h)Releasing the small box into another container. The water in the container is in 70°C.

#### 2.4.1 Reversible shape changing components using shape memory polymers and hydrogels

In this work, we demonstrate a new reversible shape-changing component design concept enabled by 3D printing two stimuli-responsive polymers - shape memory polymers and hydrogels – in prescribed 3D architectures. Our approach uses the swelling of a hydrogel as the driving force for the shape change, and the temperature-dependent modulus of a shape memory polymer to regulate the time dependence of such shape change. Controlling the temperature and aqueous environment allows switching between

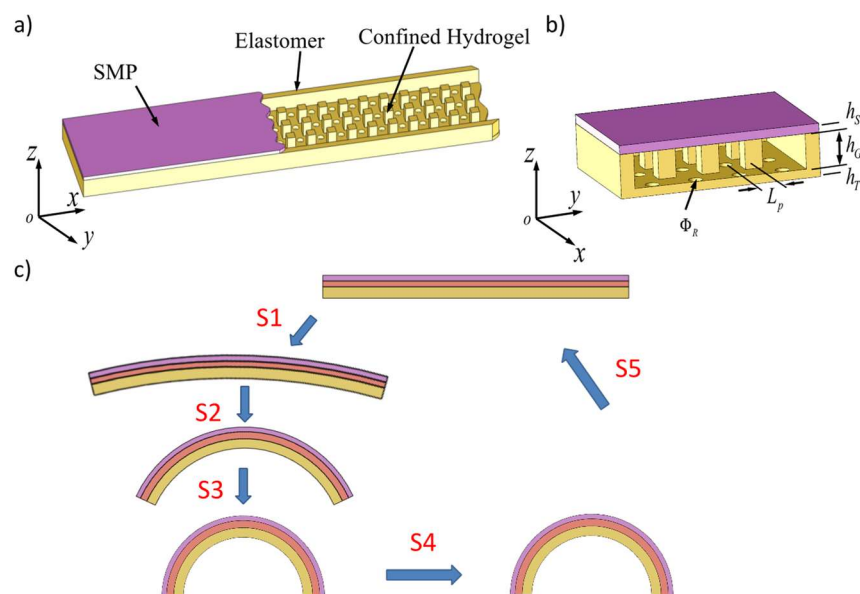


Figure 2.4.1-1. The Schematic graphs of the design concept of the two-way reversible actuator. a) The reversible actuation component by 3D printing where the hydrogel is confined by the SMP and the elastomer layers; b) The key dimensions in the design. c) Schematic plots for a typical two-way actuation: In S1, the sample is immersed in water at low temperature; in S2, it is brought to a high temperature environment and bends; in S3, it is cooled down to a low temperature; in S4, it is allowed to dry for an elongated time period; in S5, it is heated to recover the original printed shape. This finishes one actuation cycle, which can be repeated many times.

two stable configurations – the structures are relatively stiff and can carry load in each – without any mechanical loading and unloading. This work is in the manuscript “Mao, Y., Ding, Z., Yuan, C., Ai, S., Isakov, M., Wu, J., Wang, T., Dunn, M.L., and Qi, H.J., 2016. 3D Printed Reversible Shape Changing Component with Stimuli Responsive Materials. *Scientific Reports* 6, Article number: 24761.” More details can be found in this manuscript.

**Design concepts.** The key concepts to our design are to convert the hydrogel’s hydraulic swelling force from equiaxial to a linear or planar force that can drive the shape change in one particular direction or one particular plane, and to use the temperature sensitivity of the SMP properties to regulate the time for such shape change. Figure 2.4.1-1a shows the design, where hydrogel and elastomer columns are sandwiched between a layer of the SMP (top) and a layer of the elastomer (bottom). Small holes are placed in the elastomer layer to allow water (or other solutions) to flow in and out. Figure 2.4.1-1b shows the notations of dimensions in the design. Figure 2.4.1-1c shows the flow chart of working steps for a reversible actuation cycle. The printed component is straight after printing. It is then immersed into water at a temperature  $\sim 0^\circ\text{C}$  for a certain amount of time to allow the hydrogel to absorb the water (step S1); in addition, due to the low temperature, the stiffness of the SMP is high; therefore, the volume swelling of the hydrogel is highly constrained, and the strip does not show significant shape change. Next (step S2), the strip is brought into a high temperature environment (such as a water bath) where the SMP softens

significantly. This reduction in the SMP stiffness allows the large shape change. In addition, the elastomer column that connects top and bottom layers imposes constraints on hydrogel swelling in the z-direction, thus converting the swelling force into the x-y plane. Because of the stiffness difference between the elastomer and the SMP, the strip bends. After actuation at high temperature, we cool the strip to a temperature below the  $T_g$  of the SMP (step S3); due to the increase of the SMP stiffness, the strip is stiff. In the ambient environment, the hydrogel loses water and dries in step S4. After the hydrogel is fully dry, immersing the strip into a high temperature environment recovers the straight shape of the strip (step S5). At low temperature, the strip becomes stiff again. This finishes one cycle of reversible actuation, which can be repeated multiple times.

We used a multiple material 3D printer (Objet260 Connex, StrataSys, Eden Prairie, MN, USA) to realize the above concepts. We mainly used three materials in the printer material library: Grey60, Tangoblack (TB) and a hydrogel. As shown in the Method Section, Grey60 is a digital material with the glass transition temperature ( $T_g$ ) at  $\sim 48^\circ\text{C}$ , which can be used as the SMP when the temperature is changed between  $0^\circ\text{C}$  and  $60^\circ\text{C}$ . TB is rubbery at the RT and is used as the elastomer; the printed hydrogel absorbs water, showing a RT linear swelling ratio of 1.18, or volumetric swelling ratio of 1.64.

**Demonstration of the two-way actuation of a simple actuator.** The concept described above was implemented into a simple design, which was then printed by the 3D printer. Here, the top SMP layer was 0.5 mm in thickness, and the bottom TB layer was 1.5 mm, and hydrogel layer was 0.5mm. The radius of the hole was 0.4mm. The pillar had a square cross-section with the edge length of 0.5mm.

The printed strip is shown in Figure 2.4.1-2a. It was first immersed in cold water ( $3^\circ\text{C}$ ) for 12hrs and showed a small amount of bending (Figure 2.4.1-2b). The strip was then immersed in hot water (temperature of  $75^\circ\text{C}$ ) and it bent into the shape showing in Figure 2.4.1-2c in  $\sim 10$  sec. The strip was then removed from the water and was cooled down to the RT (Figure 2.4.1-2d). The strip maintained the bending shape (Figure 2.4.1-2e). At the low temperature, it was stiff, which is evident in Figure 2.4.1-2f where the bent strip can support a deadweight of 25g. After drying at low temperature, the strip was immersed in high temperature water again and it recovered the flat shape.

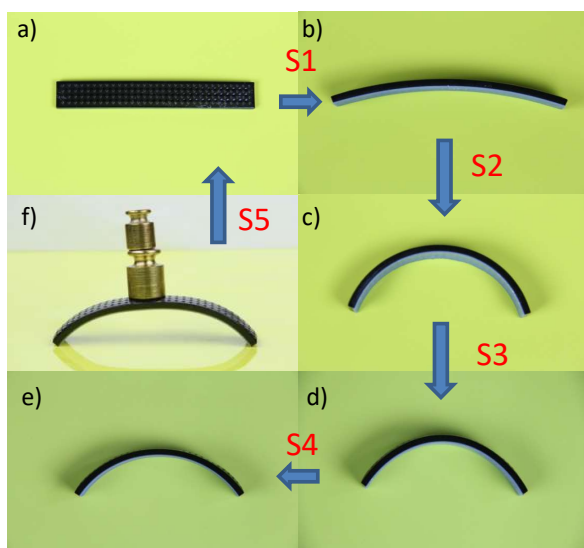


Figure 2.4.1-2. The bending angle of two activated shape memory strip in the desired shape memory cycle. a) The printed strip is straight; b) it bends slightly after immersing in cold water for 12hrs; c) it bends quickly when immersing in hot water; d) it is then taken out of water to the room temperature air; e) it is then air dried; f) the strip is stiff and can carry a load of 25g. If it is heated, it returns to the straight shape.

**Theoretical studies of the design.** Finite element method (FEM) simulations were conducted to investigate the complicated thermomechanical coupling of the SMP and the swelling property of the hydrogel by using ABAQUS (Dassault Systems, Johnston, RI, USA). The thermomechanical properties of the elastomer and the SMP were considered using a user material subroutine based on the finite element constitutive models developed by the authors. The non-equilibrium swelling/shrinking behaviors of hydrogels were modeled by using user element (UEL) provided by Chester et al. [11, 12]. To reduce the FEM model size, only a quarter of a unit cell was considered.

Figure 2.4.1-3b shows the bending angle as a function of time in water. It is clear that when the strip is in the cold water, the angle evolves slowly as water is absorbed by the hydrogel. However, once the strip is in the hot water (or the high temperature environment), it bends quickly, as indicated by a sudden jump in bending angle in Figure 2.4.1-3b. The inset in Figure 2.4.1-3b reveals the change of angle occurs in  $\sim 10$ s in hot water.

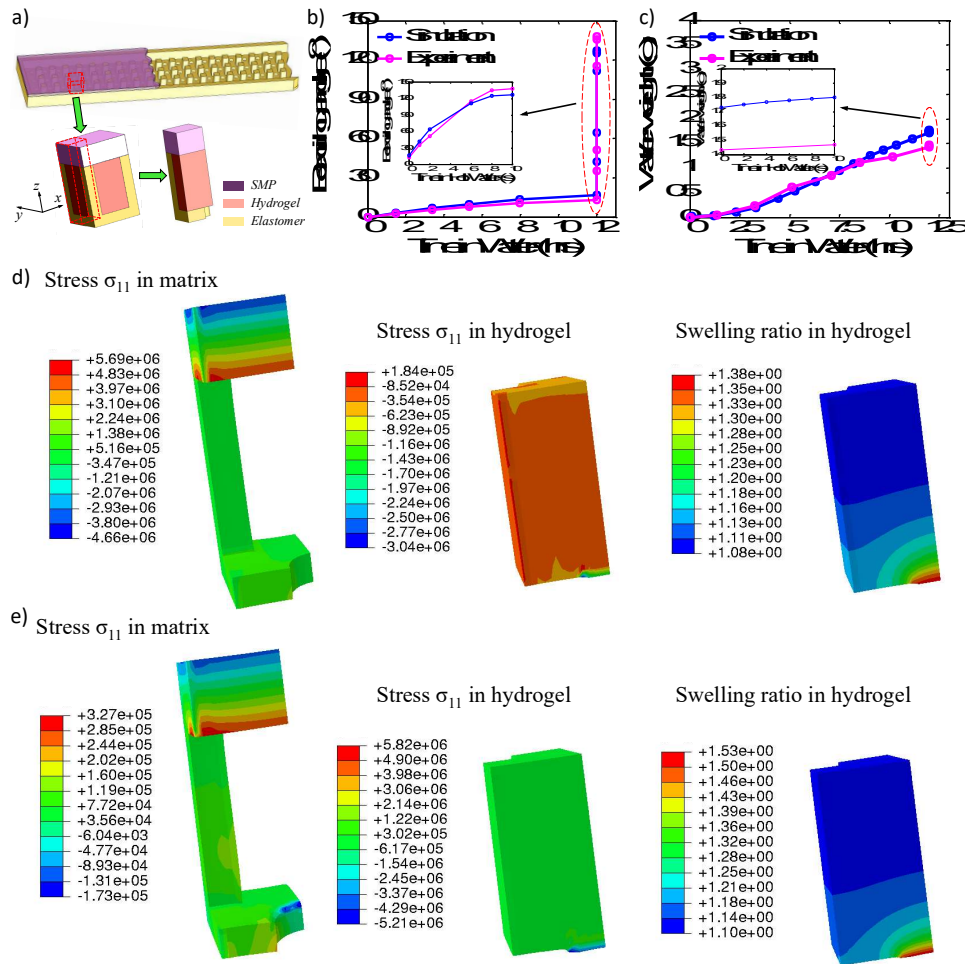


Figure 2.4.1-3. Finite element modeling of water in-take and actuation. (a) A schematic illustration of the finite element model. (b) Bending angle of the strip as a function of time of the strip in water. The inset shows the bending angle when the strip is immersed in hot water. Bending angle is calculated based on a strip that is 80mm long. (c) FEA simulation results of the weight of water inside the hydrogel as a function of time. Contour plots of axial stresses in the matrix and hydrogel and the swelling ratio in hydrogels at (d) the low temperature and (e) the high temperature.

Figure 2.4.1-3c shows the water absorbed by the hydrogel. It also shows that even during the sudden change of bending angle, the amount of water in-take only changes slightly, indicating that the modulus changes in the SMP, which is due to the temperature increase, is the key factor for the increase in bending angles. Figure 2.4.1-3d shows the stress contour for the matrix (left) and the stress and swelling ratio contours for the matrix (middle and right) at low temperature after water in-take. It can be seen that with the water in-take, the SMP (top) layer develops axial stress that is featured in bending deformation (compression on the top and bending on the bottom). In addition, the swelling of hydrogel is non-uniform, with most swelling occurring in the area where hydrogel is in direct contact with water. This is understandable, as this area has less constraint. Figure 2.4.1-3e shows the same contour plots at the high temperature. In comparison with the contour at low temperature, there are two differences. First, although the trends of stress distribution in the SMP are the same, the magnitude decreases significantly. This is because of the significant decrease in the modulus of the SMP. Second, the volume of hydrogel increases. This is interesting, as Figure 2.4.1-3b shows that water in-take remains almost constant as we increase the temperature. Therefore, the increase of hydrogel volume is because of the decrease of hydraulic pressure and the compressible nature of a hydrogel. It should be noted that hydrogels are usually assumed to be incompressible because their shear modulus is typically much smaller than their bulk modulus. This assumption is true when the hydraulic pressure is not high. However, under the confined environment in the current study, the significant hydraulic pressure can cause observable volume change of hydrogel. To further confirm that the sudden bending of the strip is caused by the change of the modulus of the SMP, instead of water in-take, we conducted experiments where we heated the sample by using an oven. The results show that although the bending speed is slow, the strip can reach the same bending angle as that heated in hot water.

We conducted parametric studies on the effects of layer thickness to the bending angle and structure stiffness. The details about these studies can be found in the manuscript. Here, we present the case of parametric study on actuation speed. Although many factors, such as the times for water absorption and depletion, can affect the actuation speed, we demonstrated the cases where we varied the dimensions of the component. We let the component absorb water at 3°C for 12 hours; we then took it to the high temperature of 75°C to allow the shape change. The change of bending curvature as a function of time (measured from the time heating starts) during heating was monitored and is reported in Figure 2.4.1-4 for the components with different layer thicknesses, represented as  $h_{\text{Elastomer}}:h_{\text{hydrogel}}:h_{\text{SMP}}$  in the figure. Here, we varied the thickness of the SMP and the hydrogel layers but maintained the total layer thickness to be constant at 2.5mm and the elastomer layer thickness to be 0.8mm. It can be seen that a thinner SMP layer generally promotes a larger curvature and a faster rate of curvature change. The

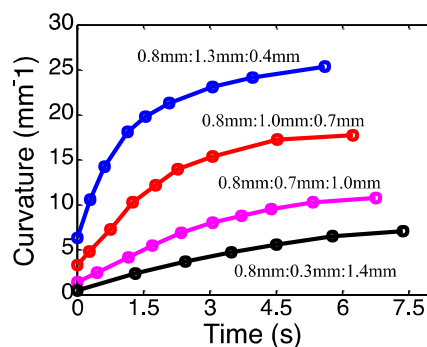


Figure 2.4.1-4. Actuation speeds of actuators with different dimensions. The change of bending curvature as a function of time for the actuators with different layer thicknesses (expressed as thicknesses of Elastomer:Hydrogel:SMP) during the Step 2 (heating).



difference in curvatures and curvature change rates can be used to design sequential folding patterns, as will be shown later in this paper.

**2D shape change objects.** To demonstrate the potential of our approach on reversible actuation of the design, we used the bending behaviors to create different shape changing structures. In the first example, we applied the reversible actuation concept to a hinge design, which was applied to a ladder where some portions of its structure have the reversible actuation components (Figure 2.4.1-5a). The hinge of the ladder consisted of three elements discussed above, where the thicknesses of the elastomer, the hydrogel, and the SMP layers were 0.5mm, 1.5mm and 0.5mm (shown in Figure 2.4.1-5b), respectively. The printed ladder is shown in Figure 2.4.1-5c. Similar to the general reversible activation cycle discussed in Figure 2.4.1-1a, after allowing the ladder in the low temperature water (3 °C) for ~10 hrs, the hinges bent slightly. After putting it in high temperature water (75 °C), it deformed into a bench as shown in Figure 2.4.1-5d. The bending configuration was fixed in low temperature (3°C) due to the glass transition property of the SMP layer. After drying in low temperature (3°C), the temporary configuration was sufficiently stiff and could sustain a 50g weight as shown in Figure 2.4.1-5e. After heating the bench to 75°C, it became a straight ladder again (Figure 2.4.1-5f). This process can be repeated many times.

**Reversible folding/unfolding origami.** Origami folding has attracted great research interest in recent years due to its potential application to active structures. For structural engineers, origami has proven to be a rich source of inspiration, and it has found its way into a wide range of structural applications, ranging from wrapping solar cells to medical stents to emergency shelters. Following the work of Fuchi et al. [13], who developed a design methodology for origami folding actuators., an origami actuator was designed by using reversible components. Here the hinge element had the thicknesses of 0.25mm, 0.4mm and 0.15mm for the elastomer, the hydrogel and the SMP layers, respectively. In Figure 2.4.1-6a, U and D indicate the bending directions of the hinge with U meaning upward and D for downward, respectively. The as-printed sheet is shown in Figure 2.4.1-6c. After being put in cold water for 10hr then transferred

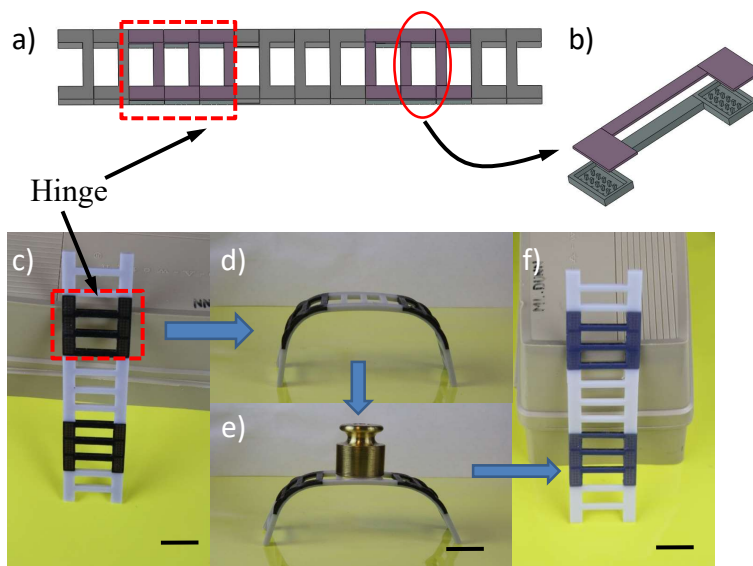


Figure 2.4.1-5. A reversible ladder and bench design. a) The design of the ladder with two hinges; b) each hinge contains the reversible component. c) The printed ladder. d) It bends into a bench shape after swelling in low temperature water for 10hrs, followed by heating to 75°C then cooling to the RT. e) The bench is stiff and can carry a load of 50g. f) The bent shape is recovered when the bench is put in high temperature water (75°C). The scale bars represent 20mm.

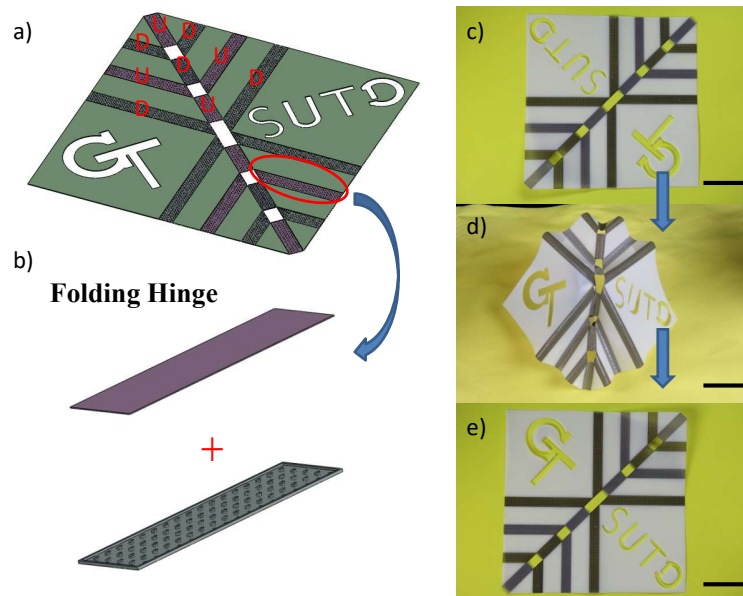


Figure 2.4.1-6. Self-folding/unfolding origami. a) A schematic graph of the design; b) the hinge uses the reversible actuation element; c-e) the reversible actuation of the sheet changing from flat sheet to folded shape, to flat sheet again. The scale bars in c-e) are 45mm.

to hot water, the plane sheet folded into a 3D origami structure. After being sufficiently dried in cold air and being heated by hot water, the sheet recovered its initial flat configuration (Figure 2.4.1-6e).

As a final example, we demonstrate a lotus flower. We designed and printed a flower-shaped 3D structure composed of three types of petals, and experimentally demonstrated the control of folding of petals as a function of controllable geometrical size. According to the discussion in Figure 2.4.1-4, for designs with the same total and elastomer layer thicknesses, those with thinner SMP layers promote larger curvatures and faster response speeds. By elaborating the design of geometrical size, we can create the sequence folding of petals like a flower. The three layers were designed with different thickness ratios of layers of the elastomer, the hydrogel, and the SMP as shown in Figure 2.4.1-7a. The inner layer was designed with the thicknesses of the elastomer, the hydrogel and the SMP layers as 0.2mm, 0.4mm, and 0.3mm. The second layer was designed with the thicknesses of 0.2mm, 0.3mm, and 0.4mm for the elastomer, the hydrogel and the SMP layers; and the outer layer was designed with the thicknesses of the elastomer, hydrogel and SMP layers as 0.2mm, 0.2mm, and 0.5mm. The corresponding curvature change profiles were characterized by three different speeds for three layers as shown in Figure 2.4.1-7b. After putting this structure in low temperature water for 12hrs, the inner layer of petals bent a little as shown in Figure 2.4.1-7c. The structure was then immersed in high temperature water. Immediately, all the layers bent, forming a flower-like configuration (Figure 2.4.1-7d and e). Taking the structure out of hot water and letting it dry, the structure maintained the flower shape and was stiff. As shown in Figure 2.4.1-7g, it could carry a load of 25g. The flower-like structure was then put into hot water and the structure became flat again (Figure 2.4.1-7f). This process can be repeated many times.

### 2.5.1 Effects of oxygen to the interface during the layer-by-layer photocuring process

Photopolymerization is one of the most widely used methods for additive manufacturing and microfabrication of polymer structures. However, the mechanical properties of these materials, formed incrementally or layer-by-layer by photopolymerization, remain unclear. One critical issue is the strength of the interfaces between adjacent layers. During free radical photopolymerization, these interfaces are

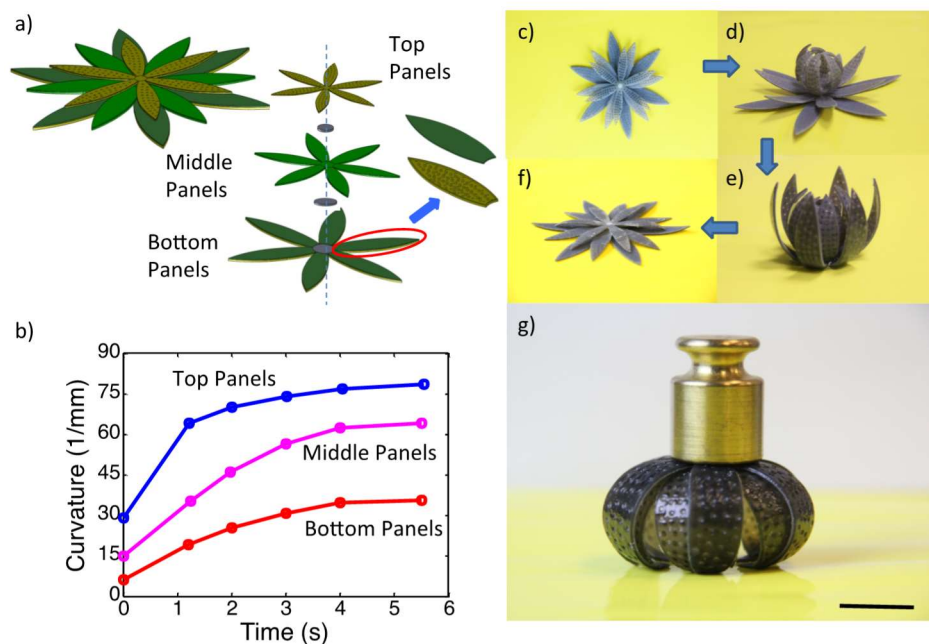


Figure 2.4.1-7. A self-folding/unfolding flower. a) Schematic of two activated shape memory petal-like structure; b) The configuration change under thermal activation as functions of time; c-f) the sequence of reversible actuation; g) the dried configuration is stiff and can carry a load of 25g. The scale bar in g) is 12.5mm.

exposed to atmospheric oxygen, which is detrimental to the polymerization reaction due to radical inhibition. The influence of oxygen on the interfacial properties, however, is still not well understood. In this work, the role of oxygen on interfacial strength during incremental photopolymerization is investigated. We carried out experiments on interfacial bonding under different photopolymerization processing parameters to investigate the effect of oxygen on interfacial strength. Based on experimental results, an interfacial model was developed to capture the evolution of interfacial strength under oxygen inhibition. This work was published in “Zhao, Z, Mu, X., Wu, J., Qi, H.J., Fang, D., 2016. Effects of oxygen on interfacial strength of incremental forming of materials by photopolymerization, *Extreme Mechanics Letters* 9(1):108–118.”

**Methods:** The resin used in this work was a mixture of 99.28 wt% PEG-DA (Poly(ethylene glycol) (700) diacrylate, 0.67 wt% photoinitiator Irgacure 819 (Phenylbis (2,4,6-trimethylbenzoyl)phosphine oxide and 0.05 wt% photoabsorber Sudan I. Realizing the challenge in conducting mechanical experiments on the single interface that is formed in the layer-by-layer photopolymerization method, we used an alternative approach, or the part-by-part incremental photopolymerization method, which is shown schematically in Figure 2.5.1-1. Samples were cured between two glass slides with 1mm thick glass supports at two edges. At first, one half of the sample (7.5mm×10mm×1mm) was cured for different time periods under various light intensities. Before photopolymerization of the first part, an oxygen permeable Poly(dimethylsiloxane) (PDMS) strip (cross section 1mm×0.5mm) (Figure 2.5.1-1a) or oxygen non-permeable glass (Figure 2.5.1-1b) was inserted at the center of the glass mold. These two cases provide comparative studies on the effects of oxygen to the interface properties. After curing the first part, the strip was removed, and the resin was injected into the second half of the mold. The whole structure with a total length of 15mm was then cured for a prescribed sufficiently long time. Tensile tests in the direction perpendicular to the interface were carried out by using a dynamic mechanical analysis (DMA) tester.



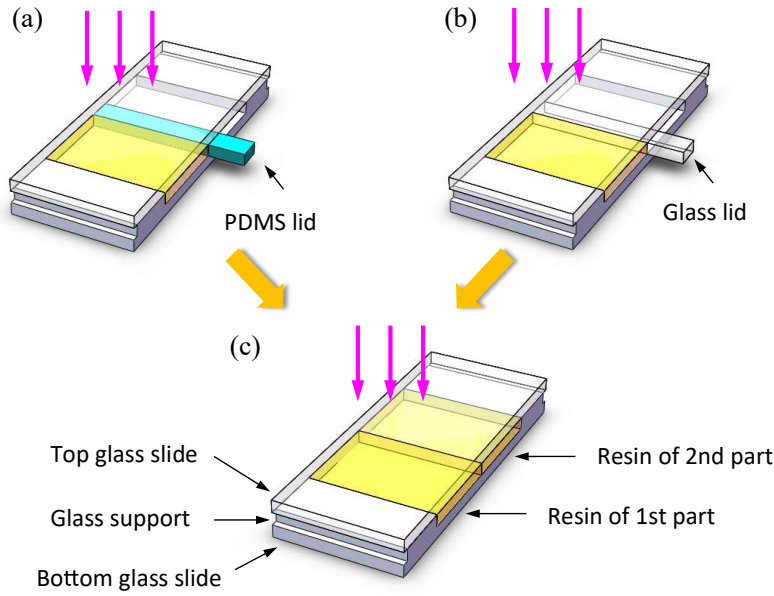


Figure 2.5.1-1. Part-by-part photopolymerization process. (a) Curing of the first part by inserting a PDMS lid. (b) Curing of the first part by inserting a glass lid. (c) Curing of the whole structure after the addition of a second part.

Fourier transform infrared (FT-IR) spectrum of the sample surface was taken on an FT-IR spectrometer with an attenuated total reflection (ATR) unit.

SEM and microscopic images of the interfacial structures are shown in Figure 2.5.1-2. In these figures, the locations of the interfaces are identified by the ridges and are marked by thin dashed lines. It is clear there are no apparent discontinuities, such as voids or cracks, at the interfaces, regardless of whether the first part was covered by PDMS or by glass.

**Theoretical model:** The model is mainly based on classical methods used in previous work on photochemistry and on photo-mechanics, but several additional assumptions are introduced to further simplify the model. The modeling domain is shown in Figure 2.5.1-3.

Evolution of chemical species during first part curing,

$$\text{Photoinitiator: } \frac{\partial \tilde{C}_I(x,t)}{\partial t} = \underbrace{-\beta \tilde{C}_I(x,t) I_0}_{\text{photoinitiator consumption}} + \underbrace{D_I \frac{\partial^2 \tilde{C}_I(x,t)}{\partial x^2}}_{\text{photoinitiator diffusion}} \quad (2.5.1-1)$$

$$\text{Free Radical: } \frac{\partial \tilde{C}_R(x,t)}{\partial t} = \underbrace{2\beta \tilde{C}_I(x,t)}_{\text{radical generation}} - \underbrace{k_t \tilde{C}_R^2(x,t)}_{\text{self-termination}} - \underbrace{k_o \tilde{C}_R(x,t) \tilde{C}_o(x,t)}_{\text{oxygen inhibition}} \quad (2.5.1-2)$$

$$\text{Molecular oxygen: } \frac{\partial \tilde{C}_o(x,t)}{\partial t} = \underbrace{-k_o \tilde{C}_R(x,t) \tilde{C}_o(x,t)}_{\text{oxygen consumption}} + \underbrace{D_{o-PEGDA} \frac{\partial^2 \tilde{C}_o(x,t)}{\partial x^2}}_{\text{oxygen diffusion}} \quad (2.5.1-3)$$

Oxygen diffusion in the PDMS strip,

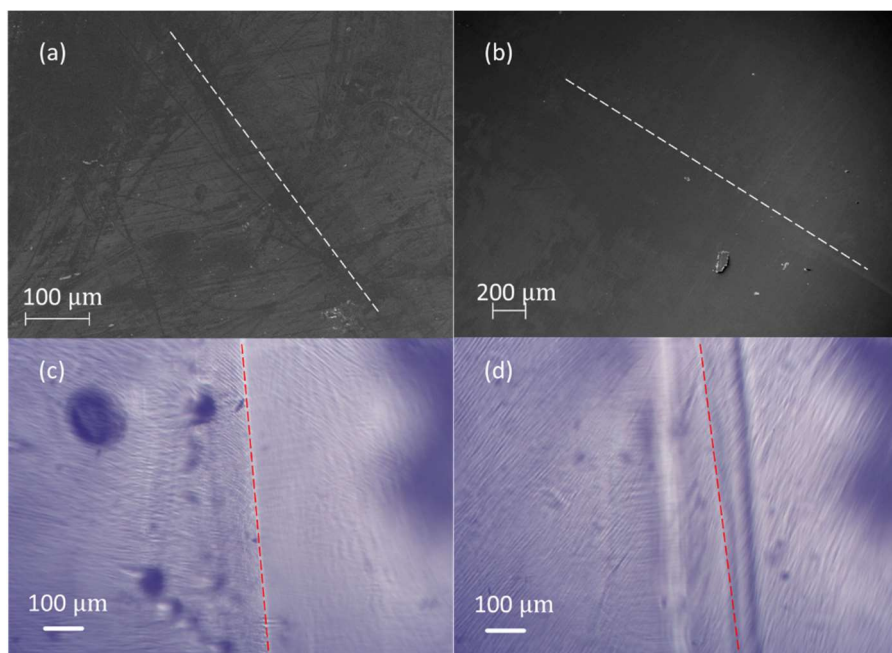


Figure 2.5.1-2. SEM and optical micrographs of the interface. (a) SEM image of sample interface prepared by inserting a glass strip (b) SEM image of sample prepared by inserting a PDMS strip (c) Microscopic image of sample interface prepared by inserting a glass strip (d) Microscopic image of sample interface prepared by inserting a PDMS strip. (Dashed lines were added to indicate the position of interface).

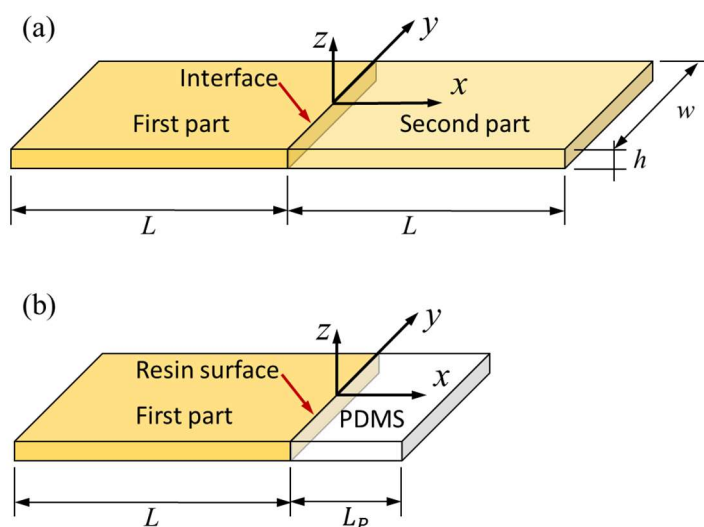


Figure 2.5.1-3. Schematic graphs of the modeling domains of first part curing (a) and second part curing (b).

$$\text{Double bonds in crosslinker: } \frac{\partial \tilde{C}_M(x,t)}{\partial t} = \underbrace{-k_p \tilde{C}_M(x,t) \tilde{C}_R(x,t)}_{\text{double bonds consumption}} \quad (2.5.1-4)$$

$$\frac{\partial \tilde{C}_o(x,t)}{\partial t} = D_{o-PDMS} \frac{\partial^2 \tilde{C}_o(x,t)}{\partial x^2} \quad (2.5.1-5)$$

Evolution of chemical species during second part curing,

$$\frac{\partial C_I(x,\tau)}{\partial \tau} = -\beta C_I(x,\tau) I_0 + D_I \frac{\partial^2 C_I(x,\tau)}{\partial x^2}, \quad (2.5.1-6a)$$

$$\frac{\partial C_R(x,\tau)}{\partial \tau} = 2\beta C_I(x,\tau) - k_t C_R^2(x,\tau) - k_o C_R(x,\tau) C_o(x,\tau), \quad (2.5.1-6b)$$

$$\frac{\partial C_o(x,\tau)}{\partial \tau} = -k_o C_R(x,\tau) C_o(x,\tau) + D_{o-PEGDA} \frac{\partial^2 C_o(x,\tau)}{\partial x^2}, \quad (2.5.1-6c)$$

$$\frac{\partial C_M(x,\tau)}{\partial \tau} = -k_p C_M(x,\tau) C_R(x,\tau). \quad (2.5.1-6d)$$

Interfacial bridging reaction,

$$\frac{dC_b(\tau)}{d\tau} = k_b C_M(0^-, \tau) C_M(0^+, \tau) \quad (2.5.1-7)$$

The relation between interfacial bonds and interfacial strength is described by the scaling relation  $\sigma_s = \alpha C_b$ .

**Results: Oxygen effect under different processing conditions:** Interfacial strength as a function of first part curing time is shown in Figure 2.5.1-4a, and the surface FT-IR spectrum of the first part is shown in Figure 2.5.1-4b. Two observations can be made based on these results. First, the interfacial strength decreases with the curing time of the first part, because there are fewer unconverted double bonds in the first part. Second, the existence of oxygen can improve the interfacial strength, especially for longer curing times. This comes from the fact that oxygen inhibition can decelerate the consumption of double bonds during first part curing. Interfacial strength as a function of light intensity is shown in Figure 2.5.1-4c. Although the presence of oxygen improves interfacial behavior even if light intensity reaches  $15 \text{ mWcm}^{-2}$ , the interfacial strength shows a continuous decrease with increases in light intensity as a result of higher reaction rate. Numerical results based on the theoretical model are shown in Figure 2.5.1-4a and Figure 2.5.1-4c, which agree well with experiments.

**Results: Details of interfacial reactions:** The evolution of chemical species during the first and the second curing are shown in Figure 2.5.1-5. Because the diffusivity of oxygen in PDMS is two orders of magnitude higher than that in PEG-DA, the oxygen concentration at the resin surface ( $x = 0$ ) nearly remains the same during the reaction (Figure 2.5.1-5a and Figure 2.5.1-5b). In the vicinity of this surface layer where oxygen inhibition dominates the reaction process, the number of reactive radicals is significantly reduced (Figure 2.5.1-5c). As a result, the conversion of double bonds near the surface is reduced, which provides more unreacted sites for interfacial bridging upon contact with the second part (Figure 2.5.1-5d).

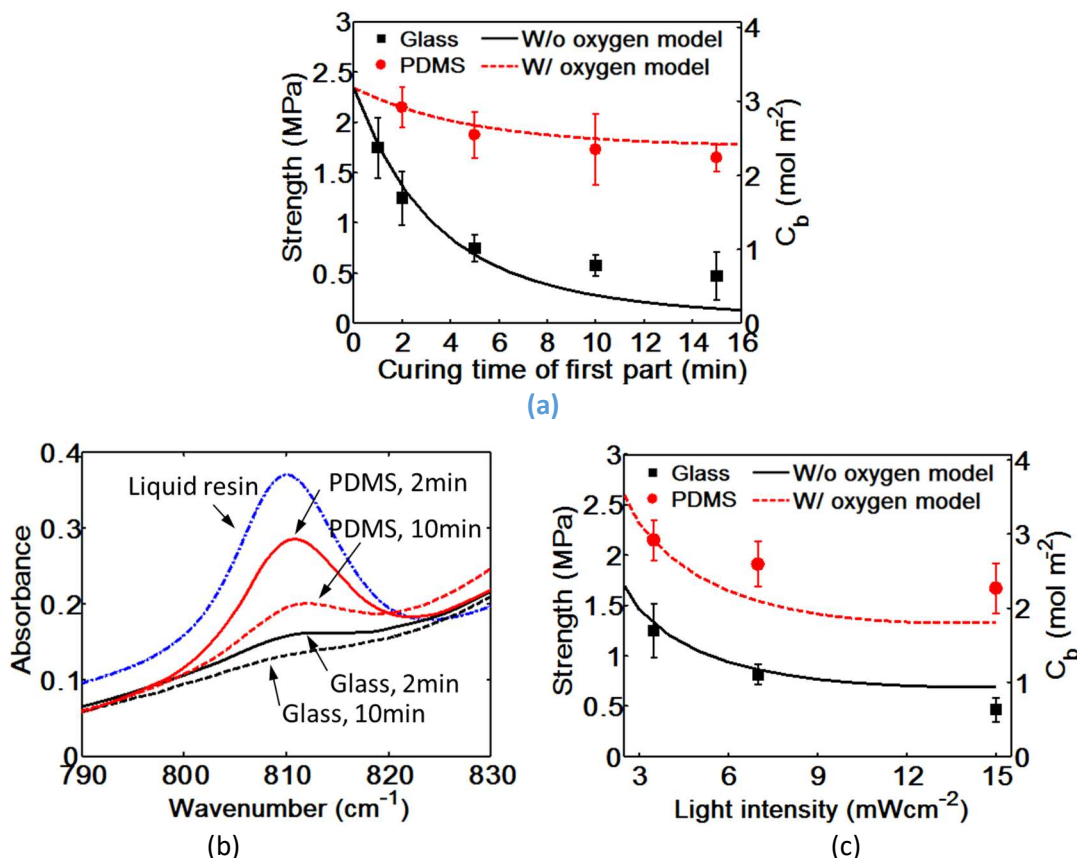


Figure 2.5.1-4. Interfacial properties of the two parts prepared under different conditions. (a) Symbols: Tensile strength as a function of curing times for the first part (light intensity  $3.5\text{mWcm}^{-2}$ ); Lines: concentration of interfacial bridges as a function of first part curing time (from the model in section 3). (b) FT-IR spectrum of liquid PEG-DA resin, the surface of the first part covered by glass or PDMS after 2min irradiation and after 10min irradiation. (c) Symbols: Tensile strength as a function of light intensity (curing time of first part 2min); Lines: concentration of interfacial bridges as a function of light intensity (from the model)

The interfacial strength shows a continuous reduction with both the irradiation time and the light intensity, as a result of a decrease in the number of double bonds in the first part, which is shown in Figure 2.5.1-6a&b. This trend is decelerated if oxygen is present. Because radicals are significantly reduced through inhibition reaction (Fig. 2.5.1-5a), many more double bonds are left unconverted, which is beneficial to interfacial bridging with the second part. In Fig 2.5.1-6a, for the case without oxygen, deviations between model prediction and experiments appear at longer time intervals. This may be because self-termination no longer obeys a second order kinetic rule due to the entanglement effect of the network.

In order to better illustrate the role of oxygen, interfacial bridging is calculated by varying the volume ratio of atmospheric oxygen; the interfacial strength is then derived by using the scaling relation  $\sigma_s = \alpha C_b$ . As can be seen in Figure 2.5.1-6c, interfacial strength  $\sigma_s$  increases by almost 200% as the atmosphere approaches pure oxygen. The strength as oxygen volume ratio approaches 0 corresponds to the case without oxygen.

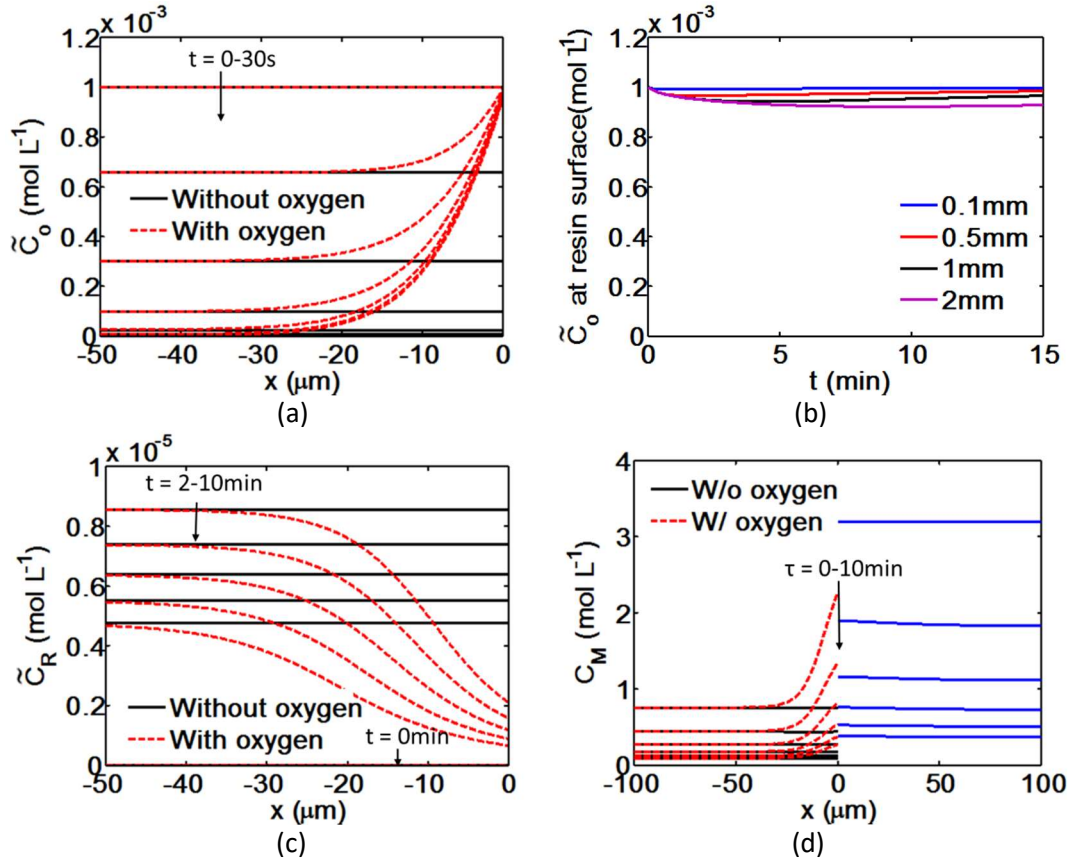


Figure 2.5.1-5. Evolution of different species during the part-by-part curing. (a) Oxygen concentration near the interface during the first part curing. (b) Oxygen concentration at resin surface as a function of time and PDMS layer thickness (c) Radical concentration near the free surface during the first part curing. (d) Double bond concentration in two sides during the second part curing (the first part curing time is 5min). Incident light intensity for (a)-(d)  $3.5mWcm^{-2}$ .

**Results: Parametrical studies:** We then conduct parametrical studies by varying model parameters. Here, the strengths of interfaces with ( $\sigma_s^{with}$ ) and without oxygen ( $\sigma_s^{without}$ ) are calculated respectively. Figures 2.5.1-7a and Figure 2.5.1-7b, show the dependence of  $\sigma_s^{with} - \sigma_s^{without}$  on resin composition, specifically the initial photoinitiator concentration  $C_{I0}$  and the initial double bond concentration  $C_{M0}$ . The red dot in Figure 2.5.1-7a indicates the experimental condition. As shown in both Figures 2.5.1-7a & b, the effect of oxygen is more apparent with the increase of  $C_{M0}$  at a fixed  $C_{I0}$ . This trend can also be found in Figure 2.5.1-7c. According to our model, the conversion rate of double bonds is proportional to a product of  $C_M$  and  $C_R$ , which relate to  $C_{M0}$  and  $C_{I0}$ , respectively. For a constant initial photoinitiator concentration, increasing the number of double bonds implies that more double bonds will be left unreacted. This is more pronounced in the presence of oxygen at the interface, as oxygen consumes a significant number of radicals. This analysis can also be used to explain Figure 2.5.1-7d where the initial photoinitiator concentration increases while maintaining the double bond concentration constant. In this case, the increase of photoinitiators generates more radicals, which consume more double bonds at the interface and thus reduce the interfacial strength.

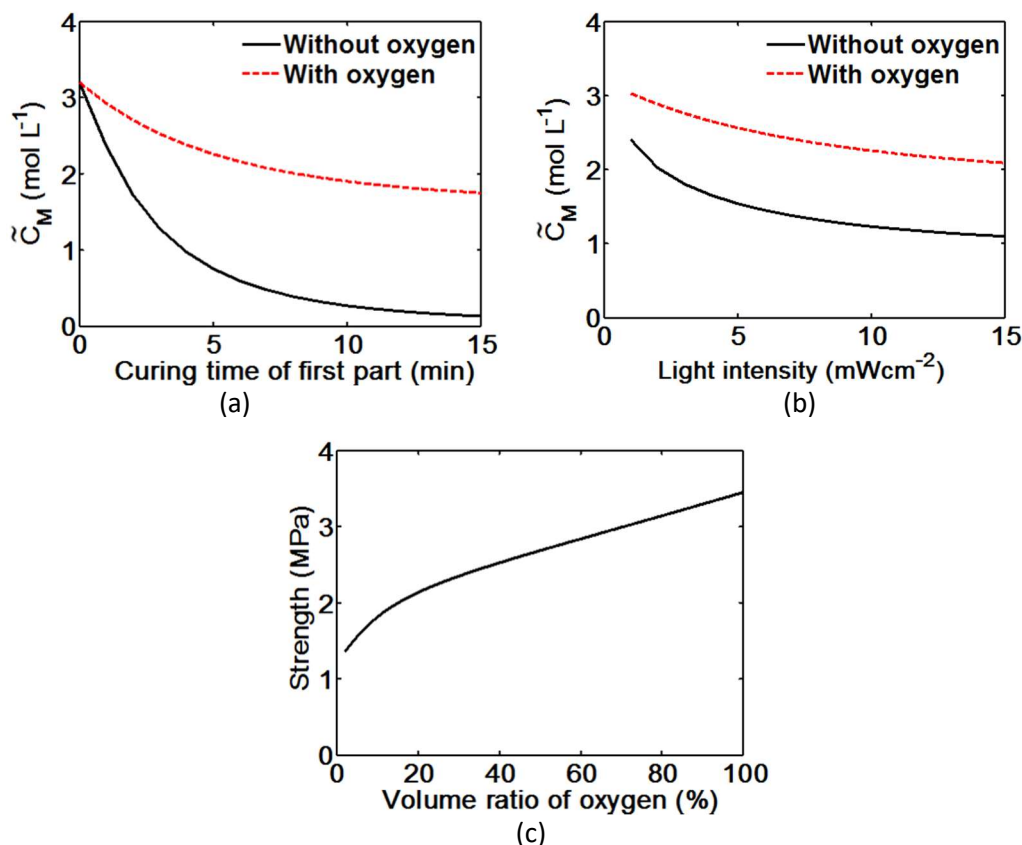


Figure 2.5.1-6. (a) Double bond concentration near the surface as a function of first part curing time (incident light intensity  $I_0 = 3.5 \text{ mWcm}^{-2}$ ). (b) Double bond concentration near the surface as a function of incident light intensity (first part curing time 2min). (c) Interfacial strength as a function of atmospheric oxygen volume ratio (first part cured for 2min,  $I_0 = 3.5 \text{ mWcm}^{-2}$ ).

Figure 2.5.1-7 suggests that a resin composed of a relatively small number of photoinitiators and a large number of double bonds (which can be realized by using short chain crosslinkers) seems desirable for the interfacial strength of incrementally photopolymerized structures. The discussion of Figure 2.5.1-7 shows that the conversion rate of double bonds plays an important role in determining the interfacial strength. In general, a slow conversion rate of double bonds at the interface in the first part curing will lead to a stronger interface. However, a slow double bond conversion rate in the bulk, which can be controlled by the photoinitiator concentration and the initial double concentration, is not desirable in layer-by-layer applications, as this leads a condition where the whole material/structure fails to fully cure. Oxygen, which only dominates at the interface, provides an efficient method of reducing the double bond conversion rate at the interface, thus it is beneficial to the interfacial strength and to the overall properties of the part or structure.

## 2.5.2 Origami Folding by Frontal Photopolymerization

Origami structures are of great interest in microelectronics, soft actuators, mechanical metamaterials and biomedical devices. Current methods of fabricating origami structures still have several limitations, such as complex material systems or tedious processing steps. In this work, we present a simple approach for creating 3D folding origami structures by the frontal photopolymerization method, which can be easily



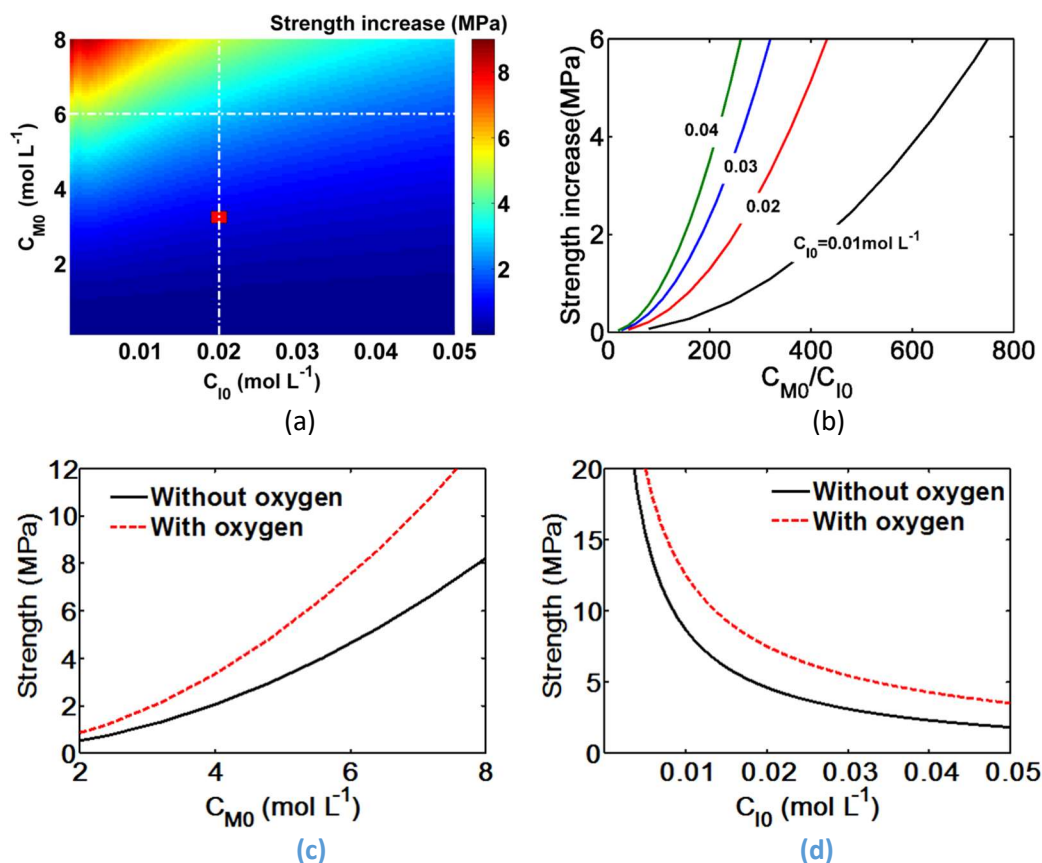


Figure 2.5.1-7. (a) Strength increase due to oxygen as a function of initiator concentration  $C_{I0}$  and double bond concentration of  $C_{M0}$  (first part cured for 2min, incident light intensity  $3.5 \text{ mW cm}^{-2}$ ). (b) Strength increase due to oxygen as a function of  $C_{M0}/C_{I0}$  (extracted from (a)). (c) Interfacial strength as a function of double bond concentration  $C_{M0}$  ( $C_{I0} = 0.02 \text{ mol L}^{-1}$ , extracted from (a)). (d) Interfacial strength as a function of initiator concentration  $C_{I0}$  ( $C_{M0} = 6 \text{ mol L}^{-1}$ , extracted from (a)).

implemented by using a commercial LED projector. This work is published in “Zhao, Z, Wu, J., Mu, X., Qi, H.J., Fang, D., 2016. Origami Folding by Frontal Photopolymerization, submitted.”

The concept of our method is based on the volume shrinkage during photopolymerization. When a polymer film is cured from one side in the frontal photopolymerization process, the newly cured layers shrink under the confinement of older layers. By adding photoabsorber into the polymer resin, an attenuated light field is created and leads to a nonuniform stress field in the thickness direction, which drives the film to bend towards the newly formed side. The degree of nonuniformity can be controlled by adjusting the LED light gray-scale and the irradiation time, an easy approach for creating origami structures. The behavior is examined both experimentally and theoretically. Two methods are also proposed to create different types of 3D origami structures.

The concept of our method is based on photopolymerization induced volume shrinkage. During photopolymerization of the resin, the material volume decreases as a result of covalent bond formation



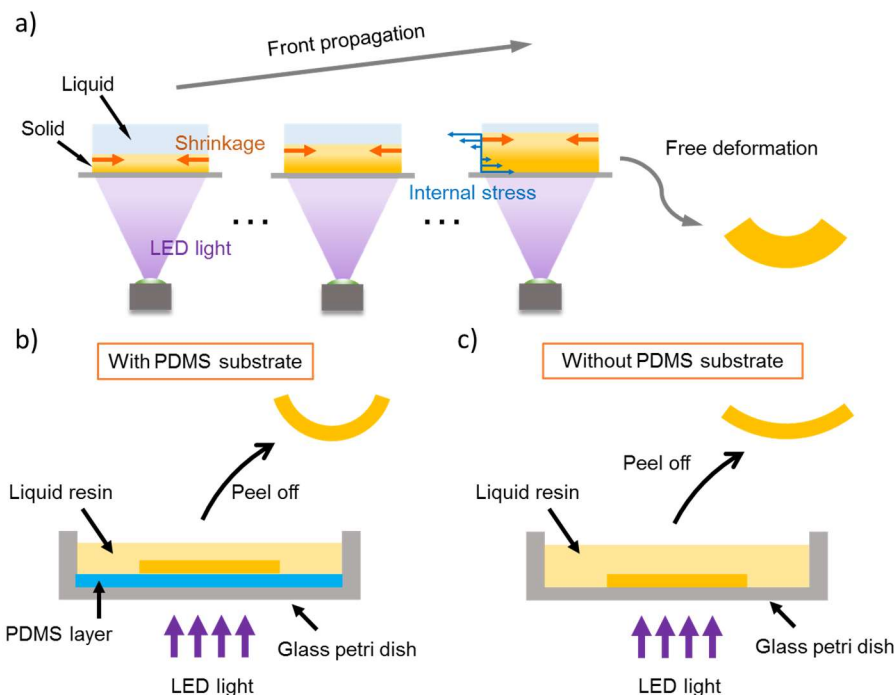


Figure 2.5.2-1. Shrinkage-induced bending during frontal photopolymerization. (a) Schematic process of volume-shrinkage-induced bending: Sequential shrinkage occurs during the frontal photopolymerization of a polymer sheet, and internal stress developed during the process drives the sheet to bend. (b) Schematic process of shrinkage-induced bending test (with PDMS substrate). (c) Schematic process of shrinkage-induced bending test (without PDMS substrate).

between monomers and crosslinkers. This behavior is commonly assumed to be undesirable in additive manufacturing (or 3D printing), microfabrication and manufacturing of polymer composites, because it causes shape distortion and internal stress. In frontal photopolymerization, the moving front of cured region leads to a nonuniform volume shrinkage, which can be controlled and utilized to create folding structures and 3D origami shapes

The process is shown schematically in Figure 2.5.2-1a. In order to control light penetration, photoabsorber is added to induce an intensity gradient in the resin. Upon irradiation, the surface layer directly exposed to light will be cured immediately, while the resin below this layer, without sufficient illumination, still remains in the liquid state. As the front of liquid-solid transition propagates toward the liquid resin, the thickness of the cured polymer film increases. Due to the presence of a light intensity gradient caused by the photoabsorber, volume shrinkage happens in a sequential manner. That is, early cured materials shrink first, while subsequently cured parts shrink under the confinement of the older parts. As a result, a nonuniform stress field develops across the sample's thickness, with a tendency to bend towards the newly formed parts. Because of the restriction imposed by the uncured liquid resin, film that has an internal stress gradient remains flat in shape. Bending occurs once the film is moved out of the liquid, and is related to several processing conditions, such as light intensity and illumination time. By imposing spatial control over the curing condition, complex 3D origami structures can be created.

**Results and discussions - Experimental investigation of shrinkage induced bending:** The property of acrylate resin was characterized by checking photopolymerized thin films with different illumination times under a constant intensity of  $5mWcm^{-2}$ , and the results showed the Young's modulus of the sample

increases linearly with the normalized conversion degree  $\phi$  of C=C double bonds. Significant shrinkage strain around -5% occurs after solidification, and its variation becomes much more mild as the reaction proceeds. During frontal photopolymerization, the evolution of these two properties can be combined to control the development of the internal stress field.

In order to demonstrate the concept of shrinkage induced bending, polymer strips were cured in a glass petri dish filled with liquid resin, with LED light projected upwards from the bottom. Inspired by the lubrication effect from both residual oxygen inhibition and pendent oligomers at the surface of poly(dimethylsiloxane) (PDMS), a PDMS substrate was inserted to make sure that cured parts would not stick to the bottom so that the sample could be removed easily. The process is shown schematically in Figure 2.5.2-1b. After different periods of irradiation under various light intensities, the solidified strip was moved out of the liquid to measure its bending curvature. Figure 2.5.2-2a shows some selected samples that were cured under light intensity of  $5\text{mWcm}^{-2}$ . The rectangular strips were cut short to facilitate measurement. The bending curvatures were measured from several figures similar to Figure 2.5.2-2a and are summarized in Figure 2.5.2-2b in symbols. It is interesting to note that curvature decreases with both illumination time and incident light intensity. Although the sequential shrinkage behavior remains the same, sample stiffness increases due to the increased thickness and modulus, making it more difficult to bend. Bending almost disappears when the curing time is longer than 10s under the intensity of  $9.5\text{mWcm}^{-2}$ .

For a comparison group, the PDMS substrate in the petri dish was removed, and then rectangular strips were cured in the same manner with incident intensity of  $5\text{mWcm}^{-2}$  (Figure 2.5.2-1). The results are shown by red open circles in Figure 2.5.2-2b. In this case, the bottom surface, which cured earliest, stuck to the substrate and could not shrink freely, as is the case with a PDMS layer. After the whole part was cured and peeled off from the substrate, the bottom surface shrank to release internal stress. This tendency is in contrast with the fact that the bottom part was compressed during the sequential shrinkage process, and the overall bending curvature was reduced. Therefore, the boundary condition at the bottom of the substrate plays a key role in determining shape changing behaviors. The effect of the surface layer's

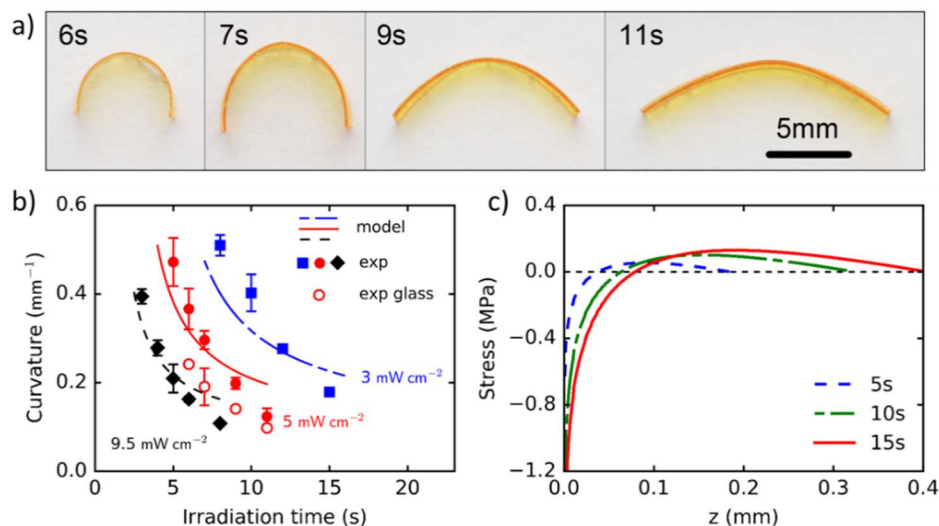


Figure 2.5.2-2. Experimental results of shrinkage-induced bending. (a) Rectangular samples cured in a petri dish with different irradiation time (light intensity  $5\text{mWcm}^{-2}$ ). (b) Bending curvature of photopolymerized strips as a function of irradiation time and incident light intensity. (c) Stress distribution across sample thickness (light intensity  $5\text{mWcm}^{-2}$ ).

confinement becomes negligible when the total thickness of cured sample increases, because the overall stress gradient along thickness governs the bending behavior.

**Theoretical model of shrinkage induced bending:** The shrinkage-induced bending is described by a theoretical model based on beam theory. During photopolymerization, samples are constrained by liquid resin. The out-plane rotation is restricted, and only in-plane stretching occurs. The mechanical behavior of films under illumination should be governed by force equilibrium along the thickness direction,

$$\int_0^{\tilde{z}(t)} \sigma dz = \int_0^{\tilde{z}(t)} E(\varepsilon - \varepsilon^S) dz = 0. \quad (2.5.2-1)$$

Here  $\tilde{z}$  is the solidified thickness. The stress  $\sigma$  is decided by  $\sigma = E\varepsilon^e = E(\varepsilon - \varepsilon^S)$ , where  $E$  is the Young's modulus,  $\varepsilon^e$ ,  $\varepsilon$  and  $\varepsilon^S$  are the elastic strain, the total strain and the shrinkage strain, respectively.  $E$  and  $\varepsilon^S$  are dependent on the conversion degree  $\varphi$  of double bonds in the acrylate resin (details of the photopolymerization model can be found in the Supporting information). The total strain  $\varepsilon$  and shrinkage strain  $\varepsilon^S$  are set to zero if the conversion degree  $\varphi$  is below the gel point  $\varphi_c$ . It should be noted that the integral domain of Equation (2.5.2-1) varies with time. Thus it is solved incrementally by time intervals to get the value of  $\varepsilon$  at different  $z$  and  $t$ .

When the solidified film is moved out of the liquid resin, the rotation constraint disappears, and the part will bend under its internal stress field. Both force equilibrium and moment equilibrium should be satisfied,

$$\int_0^{\tilde{z}(t)} \sigma dz = \int_0^{\tilde{z}(t)} E\varepsilon^e dz = 0 \quad (2.5.2-2a)$$

$$\int_0^{\tilde{z}(t)} z\sigma dz = \int_0^{\tilde{z}(t)} zE\varepsilon^e dz = 0 \quad (2.5.2-2b)$$

Here the elastic strain is obtained by a superposition of bending and stretching,

$$\varepsilon^e = \varepsilon - \varepsilon^S + \varepsilon_b + \kappa(z - \frac{\tilde{z}}{2}) \quad (2.5.2-3)$$

where  $\varepsilon_b$  is the bending strain of the midplane at  $z = \tilde{z}/2$ , and  $\kappa$  is the bending curvature. The value of  $\varepsilon$  for in-plane stretching is passed in from the calculation of Equation (2.5.2-1). Equation (2.5.2-2a) and (2.5.2-2b) can be solved as a whole to get the value of  $\varepsilon_b$  and  $\kappa$ .

Theoretical calculation results based on the model are shown in Figure 2.5.2-2b in lines. The dependence of the curvature  $\kappa$  on the irradiation time and intensity is captured well. An interesting finding is that, as a result of more uniform intensity distribution and higher rate of thickness increase, the decrease of curvature with irradiation time is faster under a stronger incident light. This observation leads to a design concept wherein, by varying light intensity (or gray scale pattern) in a 2D illumination pattern, we are able to create thick stiff panels or soft thin bending parts: for the same light irradiation time, parts under high light intensity have high stiffness but no bending, and parts under low light intensity are relatively soft but with a sufficient bending curvature.

Based on Equation (2.5.2-1) in the model, the evolution of the stress field for a sample cured under irradiation of  $5mWcm^{-2}$  is shown in 2.5.2-2c. The bottom layer that was cured at first stayed in a compressive state, while the top part was under tension. The absolute value of stress was higher in the bottom part because of much stiffer material. As the irradiation time increases, although a stress gradient still exists, the thickness and modulus of the cured sample becomes sufficiently large to resist bending deformation, and the overall curvature is negligible.

**Origami structures created by one-side illumination:** Utilizing shrinkage-induced bending in photopolymerization, we can create complex 3D structures from flat polymer sheets with programmed 2D light patterns. It should be pointed out, if the polymer sheet is cured by illumination from the bottom, as we explained before, it can only bend towards the top side. We will show first how to produce origami structures from this type of one-side illumination. Using an LED projector, 2D light patterns with spatial control over intensity are created through variation of the gray scale. Low intensity is used at those points where folding (or large bending) is expected. For the table structure in Figure 2.5.2-3a-d, intensities were set to  $15\text{mWcm}^{-2}$  and  $3\text{mWcm}^{-2}$  for the panel and legs, respectively. This was realized by creating figures with a spatial variation of grayscale (inset in Figure 2.5.2-3a). After a specific irradiation time (10s for Figure 2.5.2-3a), as discussed before, the cured sheet remained flat while immersed in the liquid resin. Parts that were exposed to high intensity were thicker, and parts exposed to low intensity (for example those legs in Figure 2.5.2-3a) were relatively thinner. When the sample was removed from the liquid, those parts exposed to low intensity (legs in Figure 2.5.2-3b) bent towards the newly formed side as a result of nonuniform stress. Because the bending parts had lower stiffness, this configuration was not stable. To fix the shape, samples were held by a tweezer and further cured under a uniform LED light of  $10\text{mWcm}^{-2}$  for 20-30s (Figure 2.5.2-3c), which stiffened the structure due to the dramatic increase of the modulus in the previously soft parts. After this post curing, the sample became strong enough to support some weight. A table structure holding several glass cover slips (with a total weight of 1.1g) is shown in Figure 2.5.2-3d.

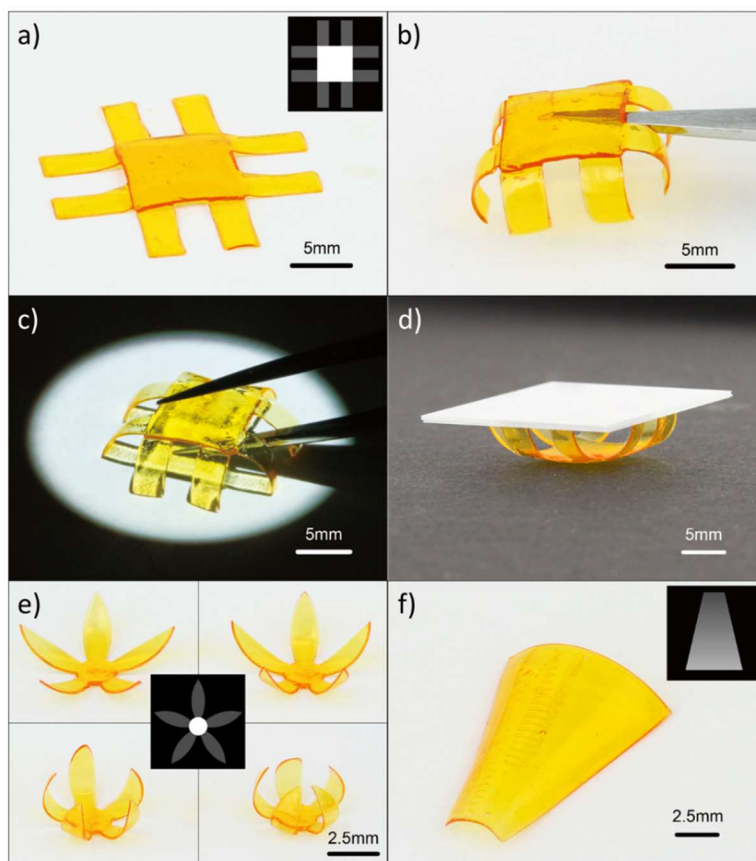


Figure 2.5.2-3. Fabrication of origami structures by one-side illumination. (a) Polymer sheet right after photopolymerization. (b) Free bending of spatial differently cured sheet. (c) Shape fixing of bending structures by post curing. (d) Sample after post curing is stiff and able to hold several glass cover slips. (e)

Flower structures with different opening degree. (f) Polymer sheet with a continuous variation of curvature.

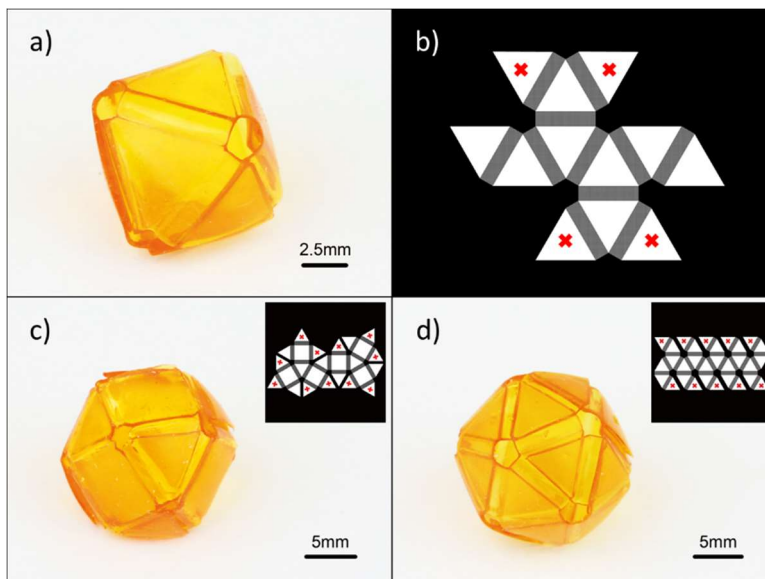


Figure 2.5.2-4. Polyhedrons created by one-side illumination (a) Octahedron (panel intensity  $15 \text{ mWcm}^{-2}$ , hinge intensity  $3 \text{ mWcm}^{-2}$ , irradiation time 6s). (b) The grayscale pattern of octahedron structure. (c) Truncated cube (panel intensity  $15 \text{ mWcm}^{-2}$ , hinge intensity  $3.3 \text{ mWcm}^{-2}$ , irradiation time 6s). (d) Regular icosahedron (panel intensity  $15 \text{ mWcm}^{-2}$ , hinge intensity  $4 \text{ mWcm}^{-2}$ , irradiation time 6s).

Much more delicate control over the light pattern produces structures with higher complexity. Flowers with different opening degrees are shown in Figure 2.5.2-3e. These four flowers were all created using an irradiation period of 6s. The illumination intensity of the central round panel was  $10 \text{ mWcm}^{-2}$ , and petal intensities were set to 2.5, 4, 6 and  $7 \text{ mWcm}^{-2}$ , respectively. The sample that was illuminated with the lowest intensity shows the smallest opening angle. The round panel at center is illuminated with a high intensity, and it remains flat in all 4 cases. A polymer sheet with continuous variation of bending curvature is shown in Figure 2.5.2-3f. This structure was realized by illuminating a trapezoidal pattern with a gradient of grayscale for 4s. The edge with the highest curvature was illuminated with the lowest intensity ( $2.5 \text{ mWcm}^{-2}$ ), and intensity gradually increased till the other edge (to  $10 \text{ mWcm}^{-2}$ ).

3D folding structures were created by using a combination of flat panels and hinges bent towards one side. Some different types of polyhedron capsules are shown in Figure 2.5.2-4. In order to stabilize the folding process, extra panels are introduced in the light pattern. For example, to form the shape in Figure 2.5.2-4a, four more panels marked by red crosses are attached to the net pattern of octahedron in Figure 2.5.2-4b. During the folding process, an extra panel overlaps on the top of a neighbor panel and thus stabilizes the structure.

**Origami structures created by two-sides illumination:** Structures presented in the previous section are created by polymer sheets bending towards one single side, thus the freedom of design is limited. In this section, we will show a modified method that is able to create more complex origami structures. The process is shown schematically in Figure 2.5.2-5a. Liquid resin is injected into a flat mold confined by two glass slides, two PDMS lubrication layers are pasted on the inner sides of the glass slides respectively to avoid adhesion of cured parts. The distance between two PDMS slides is confined to 0.5mm. For the first step, parts designed to bend towards direction 1 (indicated by number 1 in Figure 2.5.2-5a) are illuminated

under low intensity from the bottom. After that, the whole structure is flipped over without in-plane movement of position. Then parts designed to bend towards direction 2 (indicated by number 2 in Figure 2.5.2-5a) are illuminated in the same manner. By releasing the mold, the cured sheet bends towards the two different sides. In a real application, one can also apply two light sources, or use a light splitter to expedite the processing time. Two light patterns are projected in sequence to realize this two-step

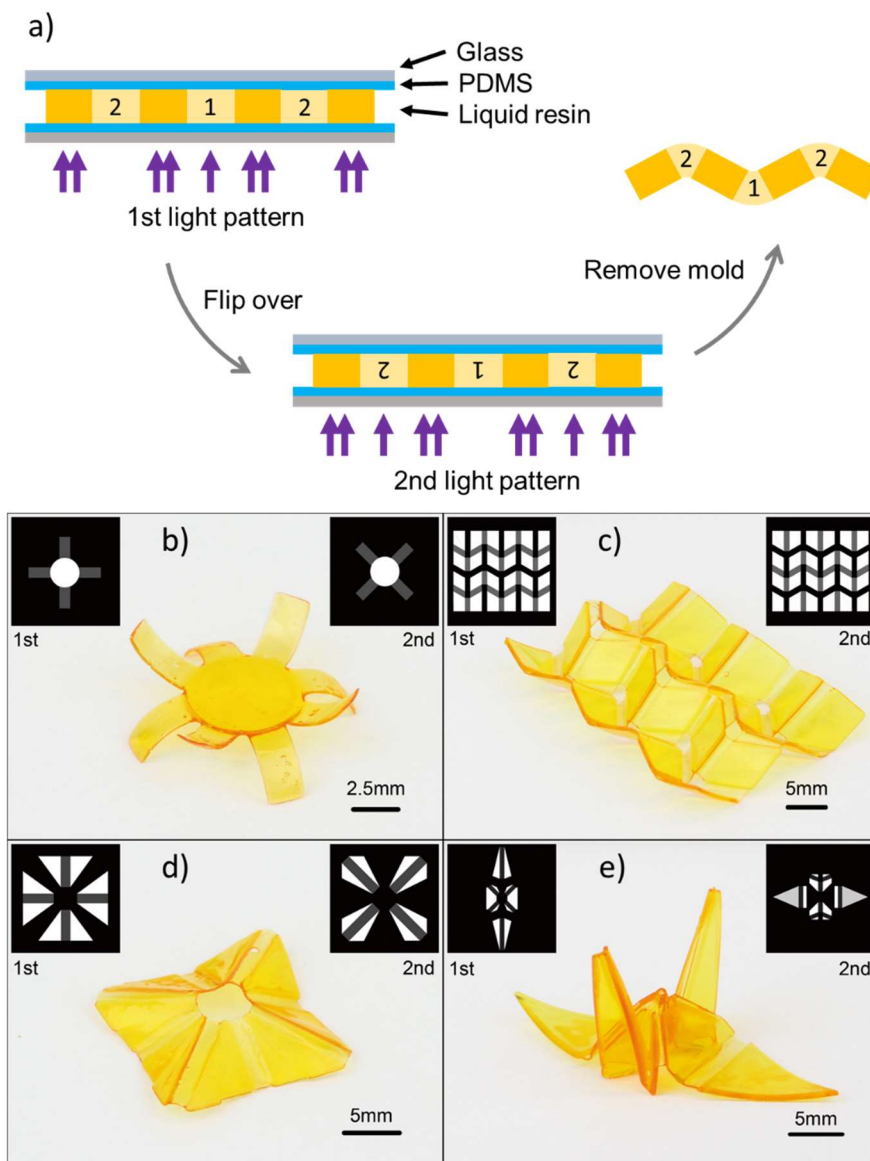


Figure 2.5.2-5. Fabrication of origami structures by two-sides illuminations. (a) Schematic process of two-sides illumination method. (b) Table (panel intensity  $18 \text{ mWcm}^{-2}$ , petal intensity  $2.5 \text{ mWcm}^{-2}$ , irradiation time of each side 7s), (c) Miura structure (panel intensity  $20 \text{ mWcm}^{-2}$ , hinge intensity  $2 \text{ mWcm}^{-2}$ , irradiation time of each side 7s), (d) tent (panel intensity  $18 \text{ mWcm}^{-2}$ , hinge intensity  $2 \text{ mWcm}^{-2}$ , irradiation time of each side 7s) and (e) crane (panel intensity  $20 \text{ mWcm}^{-2}$ , body hinge intensity  $1 \text{ mWcm}^{-2}$ , wing hinge intensity  $2 \text{ mWcm}^{-2}$ , irradiation time of each side 15s). created by two-sides illumination method.



illumination. The positions marked by 2 are made black during the first step illumination, and the positions marked by 1 are made black during the second illumination, while plane panels are irradiated in both steps.

3D origami structures produced by two-side illumination are presented in Figure 2.5.2-5b-e. Figure 2.5.2-5b shows a table with legs in two directions, created by illuminating the leg parts from two sides. The intersection points of different hinges are left as voids to facilitate the folding process. This is shown, for example, by the vertices in the Miura structure (Figure 2.5.2-5c) and the top of a pyramid tent (Figure 2.5.2-5d). Different intensities can be used for separate hinges to enrich the freedom of the origami. For the origami crane in Figure 2.5.2-5e, an intensity of  $2\text{ mWcm}^{-2}$  was used for the wing hinges and a very low intensity of  $1\text{ mWcm}^{-2}$  was used for the hinges of legs and tails.

A comparison between these two methods shows that they are suitable for different conditions. While the second method of two-side illumination has the ability to create very complex structures, extra processing steps become inevitable, such as, for example, the preparation of a mold and the insertion of liquid resin. As for the one-side method, structures can be created by just shining a single pattern onto a liquid resin vat, but the degree of freedom of the origami is confined. Thus, if a structure can be designed simply by a combination of hinges turned towards one direction, the one-side method seems sufficient. The two-side illumination method becomes necessary when more delicate control over the origami is desired.

### 2.6.1 Thermal cure effects on electromechanical properties of conductive wires by direct ink write for 4D printing and soft machines

Recent developments in soft materials and 3D printing are promoting the rapid development of novel technologies and concepts, such as 4D printing and soft machines, that in turn require new methods for fabricating conductive materials. Despite the ubiquity of silver nanoparticles (NPs) in the conducting electrodes of printed electronic devices, their potential use in stretchable conductors has not been fully explored in 4D printing and soft machines. This work studies the effect of thermal cure conditions on conductivity and electro-mechanical behaviors of silver ink by the direct ink write (DIW) printing approach.

This work is published in “Mu, Q, Dunn, C.K. Wang, L., Dunn, M.L., Qi, H.J., Wang, T., 2016. Thermal cure effects on electromechanical properties of conductive wires by direct ink write for 4D printing and soft machines, submitted.”

Our studies showed that the electro-mechanical properties of silver wires can be tailored by controlling cure time and cure temperature to achieve conductivity as well as stretchability. For the silver NP ink we used in the experiments, silver wires cured at  $80^{\circ}\text{C}$  for 10-30min have conductivity  $>1\%$  bulk silver, Young's modulus  $<100\text{MPa}$ , yield strain  $\sim 9\%$ , and can retain conductivity up to 300% strain. In addition, under stress controlled cyclic loading/unloading conditions, the resistance of these wires is only about 1.3 times the initial value after the 100th repeat cycle (7.6% maximum strain in the first cycle). Silver wires cured at  $120^{\circ}\text{C}$  for 10-20min are more sensitive to strain and have a yield strain of around 6%. These properties indicate that the silver ink can be used to fabricate stretchable electrodes and flex sensors. Using the DIW fabrication method, we printed silver ink patterns on the surface of 3D printed polymer parts, with the future goal of constructing fully 3D printed arbitrarily formed soft and stretchable devices and of applying them to 4D printing. We demonstrated a fully printed functional soft-matter sensor and a circuit element that can be stretched.

**Materials and Method:** The silver nanoparticle ink used in this study was DuPont ME603, which was donated by DuPont Inc. and has a solid content of 49%-53%, viscosity of  $15\text{-}35\text{ mP}\cdot\text{s}$  and sheet resistivity  $<200\text{ m}\Omega/\text{sq}/\text{mil}$ . The manufacturer recommends the curing condition of  $120^{\circ}\text{C}$  -  $140^{\circ}\text{C}$  in a static box oven for 10min. In this work, we DIW printed the ink onto a 3D printed elastomer substrate, namely TangoBlack, one of the model materials available in the material library of the polyjet 3D printer Objet



Connex 260 (Stratasys Inc., Edina, MN, USA). The reason for choosing a 3D printed substrate is that our work is intended to combine 3D printed materials with DIW of functional inks, and TangoBlack is a material used in our previous work on 4D printing. In addition, we found that when the silver ink was printed onto a soft substrate such as an elastomer, it could be easily peeled off for mechanical testing.

**Direct Ink Write setup:** We printed the silver ink onto a 3D printed elastomer substrate using a DIW experimental setup, which is shown in Figure 2.6.1-1a. The printing platform moves the substrate along the y-direction, while a pressure controlled syringe moves in the x- and z- directions. The pressure in the syringe is controlled by a pressure regulator (Ultimus V, Nordson EFD, East Providence, RI, USA). The syringe was attached to a nozzle with 0.61mm inner diameter. With a pressure of 15psi and a printing speed of 3mm/s, we were able to print the silver ink with consistent cross-sectional areas.

**Thermal curing:** Once the silver ink was printed, it was cured in a convection oven (Model 13-247-750G, Fisher Scientific, Pittsburgh, PA, USA) at different temperatures and curing times. To record the resistance change during curing, we fabricated two copper electrodes that connected the printed lines to a multimeter (Keithley2100, Keithley Instruments, Cleveland, OH, USA), which was controlled by a LabVIEW data acquisition program and sampled at 0.5-5Hz.

**Measurement of cross-sectional area:** To calculate the resistivity and modulus of printed silver wires cured under different conditions, the cross sectional area of these wires should be known. Cross-sectional images of the cured silver wires were taken with a trinocular microscope (Model 89404-886, VWR, Suwanee, GA, USA). 2.6.1-1c shows a typical cross-section of the cured ink. The cross-sectional area was then calculated by using the open source image processing software ImageJ.

**Stress-strain and cyclic loading/unloading tests:** After curing and measuring the cross-sectional area, the silver wires were carefully peeled off from the substrates using a pair of tweezers. The electrical and mechanical properties were then studied. We used a dynamic mechanical analysis (DMA) tester (Model Q800, TA Instruments, New Castle, DE, USA) and a multimeter to measure the electro-mechanical properties of cured freestanding wires. For the stress-strain tests, the strain control mode was used with a strain rate of 10% /min. For the cyclic loaded/unloaded tests, the stress control mode was used with a stretch/release speed of 25MPa/min (corresponding to a strain rate of 0.5%/s -2%/s), and a holding time of 0.5min between cycles. The resistance change during cyclic testing was also recorded. All electromechanical property tests were performed at room temperature (22°C).

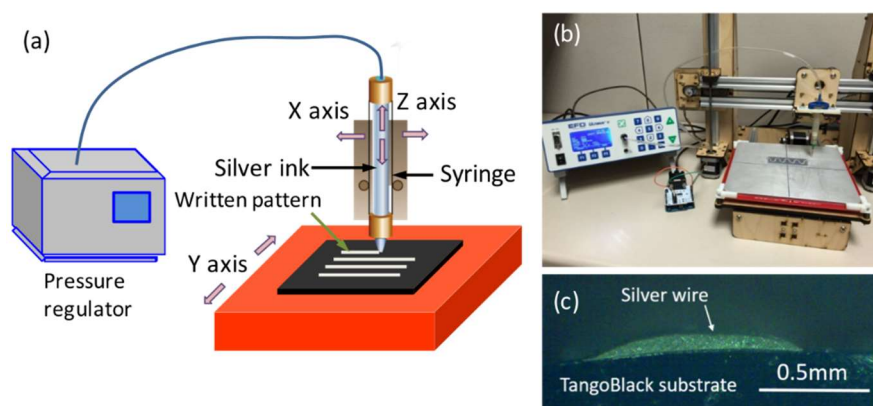


Figure 2.6.1-1. (a) A schematic graph of the DIW setup where the syringe can move in the x- and z- directions and the motion stage can move in the y-direction. A pressure regulator is used to control the pressure applied to the syringe. (b) A photo of the DIW experimental setup. (c) A microscope image of a cross section of written silver wire on the elastomer substrate.

**Resistivity:** For all resistance measurements, a two-point probe method was used to calculate the bulk resistivity and its change throughout curing.

**Results and discuss - Effect of thermal cure conditions:** In order to choose proper curing temperatures, both TGA and DSC tests were conducted to study the mass change during curing. The TGA and DSC curves are shown in Figure 2.6.1-2. It can be seen that the mass of the sample decreases as the temperature increases, settling at ~54% of the initial mass. This value confirms the removal of solvents and additives and agrees with the solid content (49%-53%) of the ink according to the manufacturer. The mass reduction can be divided into three stages, which are shown by the slope change in the TGA curve, and which can be identified from the three peaks in the derivative thermogravimetry (DTG) curve. In the first stage, the sample's mass quickly drops 26% between 47°C and 177°C, with an endothermic reaction observed from the DSC curve, which may be caused by the evaporation of solvents. In the second stage, the mass sharply drops another 11% near ~200°C, where the peak on the DSC test indicates decomposition of organic additives or removal of residual solvents. Finally, in the third stage, at around 440°C there is another mass drop, which may be caused by decomposition of other organic/inorganic additives.

**In situ resistance change during curing:** The TGA/DSC curves show that as the temperature increases, the solvent in the ink evaporates at different temperatures. Thus, we cured the ink at different temperatures in the range of 80°C -180°C for a relatively long time (60min) to detect resistance changes. We compared the curing processes at four different temperatures: 80°C, 100°C, 120°C, and 140°C (Figure 2.6.1-3a). To reduce the variations between individual samples, we normalized the resistance during curing by using individual samples' respective  $R_{60min}$ , the resistance measured at 60min. The infinitely large resistance at the onset of curing is because the silver NPs are surrounded and separated by solvent and organic shell, inhibiting the formation of a conductive path. The resistance changes show that the solvent evaporates gradually as a function of curing time, where longer curing times contribute to the drop in resistivity and the formation of conductive paths within wires. For the 120°C and 140°C cured samples, the resistance is nearly saturated within the first 10min, which agrees with manufacturer suggested curing conditions, while the 80°C and 100°C cured samples show slower curing rates, but the resistivity finally becomes constant after curing for 40min-60min.

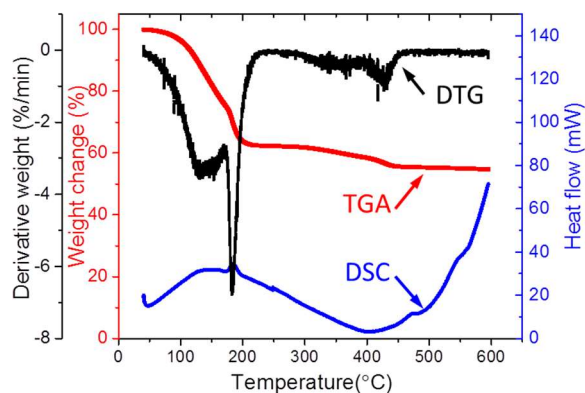


Figure 2.6.1-2. TGA (red line) and DSC (black line) measurements of the ink during curing: Heated from 40.00°C to 600.00°C at 10.00°C /min. The specimen mass: 18.343 mg for TGA, and 13.790 mg for DSC. The derivative thermogravimetry (DTG) curve is also shown in black color.

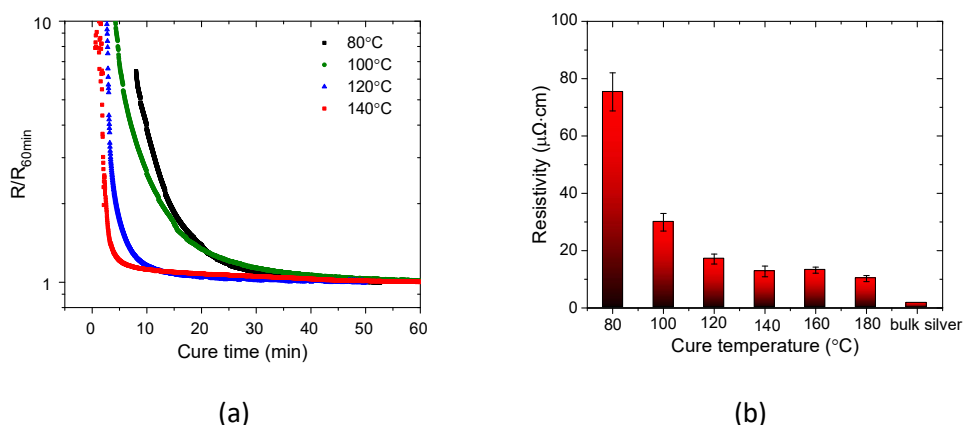


Figure 2.6.1-3. (a) Resistance change during curing at 80°C, 100°C, 120°C, 140°C for about 60min. (b) Calculated resistivity cured at different temperature for 60min and compared with bulk silver.

To calculate the resistivity, optical microscope images of the wire's cross section were taken to measure the cross sectional area (see Figure 2.6.1-1c for a typical image). Under the aforementioned operation conditions (15psi pressure, 3mm/s speed), the wires had an average width of 1.07mm, and a cross-sectional area of 0.062mm<sup>2</sup>. Using this measurement, the resistivity was calculated and is shown in Figure 2.6.1-3b for curing 60min at different temperatures. The resistivity of bulk silver is also shown for comparison. With curing temperatures greater than 140°C, the effect of temperature on resistivity is not obvious, and the saturated resistivity is ~8 times higher than that of bulk silver. In the lower curing temperature range (80°C -120°C), the resistivity drops significantly as the temperature increases. Interestingly, even at 80°C, the ink can be conductive after being cured for 60min, and the resistivity is only 5-6 times higher than those cured at 140°C. In addition, Figure 2.6.1-3a shows that the resistance becomes almost constant after 40min-60min (even at 80°C), indicating a wire with stable conductivity is formed.

Microstructure characterization: SEM images (Figure 2.6.1-4) show the morphology and particle packing for the ink cured under different conditions. For comparison, images from the air-dried ink are also presented. The overall view (image in the middle) of the air-dried ink shows separated small islands with different shapes and diameters without a clear interconnected path. A zoomed-in image (the left image) of the connected area shows that the silver nanoparticles of ~1 $\mu\text{m}$  diameter are nearly separated from each other; for the unpacked area, small silver particles having diameters of ~100nm are separated from each other without forming a conductive path. In samples cured at 80°C for 30min, we see the formation of conductive paths. As shown in the image in the middle, connected islands are forming, with some amount of holes. The zoom-in of the connected area (left image) shows fully packed silver particles and inter-particle boundaries can be seen but not very clearly. For the unpacked area (right image), we see large particles that are close to each other (as compared to the air-dried samples). When cured at 180°C for 30min, some pores exist, which might be responsible for the relatively large resistivity as compared to bulk silver, but large connected regions are also obvious. From the zoom-in of the connected region (left image), we can see better-connected particles; even in the not-fully connected-region (right image), silver NPs are physically in contact.

Electro-mechanical properties: We conducted tensile tests on freestanding silver wires. Three samples were tested for each curing condition. Figure 2.6.1-5 shows results from two representative samples subject to two different curing conditions (at 80°C for 20min and at 140°C for 20min, respectively). The

sample cured at a higher temperature exhibits a much higher yield stress and lower yield strain than does the lower temperature cured sample. The resistance of the high temperature cured sample is more sensitive to strain during stretching than that of the low temperature cured one. In addition, surprisingly, the silver wire can be stretched significantly. For the sample cured at 140°C for 20min, the cured wire can be stretched ~150%, but with significantly increased resistance; the sample cured at 80°C for 20min cured can be stretched 300% with an increase of resistance of ~ 400 times.

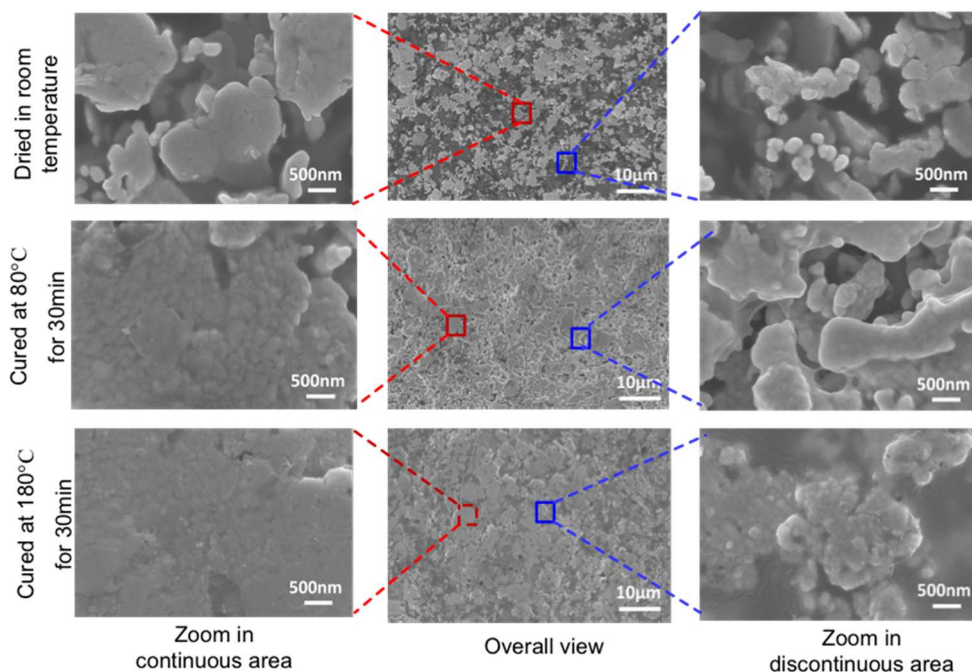


Figure 2.6.1-4. Comparison of SEM image of surface morphology: as dried, cured for 30 min at 80°C and cured for 30 min at 180°C.

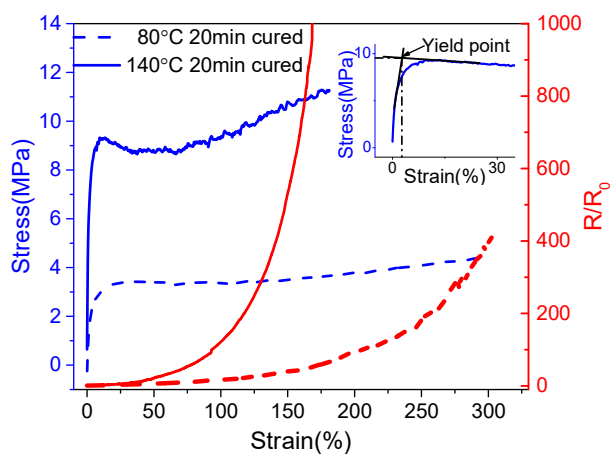


Figure 2.6.1-5. Stress-strain curves of printed silver wires and normalized resistance change when stretched, taking 80°C 20min and 140°C 20min cured samples as examples. The inserted image shows how to obtain yield strain and stress from the stress-strain curve of the 140°C 20min cured sample.

For applications in 4D printing and soft machines, the conductive materials should have 1) high electrical conductivity to achieve high-efficiency for the devices, 2) compliance that matches with the substrate, 3) high elasticity, and 4) an almost constant electrical conductivity under applied strain. In the following, we focus on the conductivity, modulus, yield strain, and elongation of the DIW printed silver wires.

**Conductivity:** Based on the curing condition study, we chose to cure the silver NPs in the oven at six different temperatures: 80°C, 100°C, 120°C, 140°C, 160°C and 180°C, with curing durations of 10min, 20min, 30min, 40min, 50min and 60min; the results are summarized in Figure 2.6.1-6a. In general, the resistivity decreases as the curing temperature and curing time increase. For the range of these curing conditions, the resistivity is between 150.9 $\mu\Omega\text{cm}$  -10.2 $\mu\Omega\text{cm}$ , which corresponds to a resistivity of 94 and 6.4 times that of bulk silver (1.6  $\mu\Omega\text{cm}$  [14]), respectively. Since the 3D printed materials from the 3D printer can sustain a high temperature of  $\sim 120^\circ\text{C}$ , we chose the silver wire that was cured under the mild temperature (lower than 120°C) to serve as conducting wires for 4D printing and soft machine applications.

**Young's moduli:** Figure 2.6.1-7 shows the evolution of Young's moduli as a function of curing temperature and curing time. Here, the Young's modulus is determined from the initial slope of the stress-strain curve ( $\sim 0.5\%$ ). It is clear that a higher temperature, or a longer curing time, leads to a higher Young's modulus. This is consistent with the SEM observations that higher curing temperature yields to more compacted and better connected silver NPs. The Young's moduli, however, are lower than that of bulk silver. From Figure 2.6.1-7, the highest modulus is  $\sim 800\text{MPa}$ , under the curing condition of 140°C for 60min. For bulk silver, the modulus of electron-beam deposited free stranding Ag films is roughly 63GPa, and the calculated  $E_{\langle 111 \rangle}$  is 82.2 GPa [15]; inkjet printed silver film after being sintered at 250°C has a modulus around 50GPa [16]. It is also interesting to note that for the 80°C curing temperature we observe no significant change in modulus as a function of curing time, even though this temperature yields a conductive line after curing. In our experiments, we found that curing temperatures higher than 140°C resulted in wires that were very stiff, which significantly limited their ability to stretch. Therefore, in the following, samples with curing temperatures below 140°C were used for the electromechanical property studies.

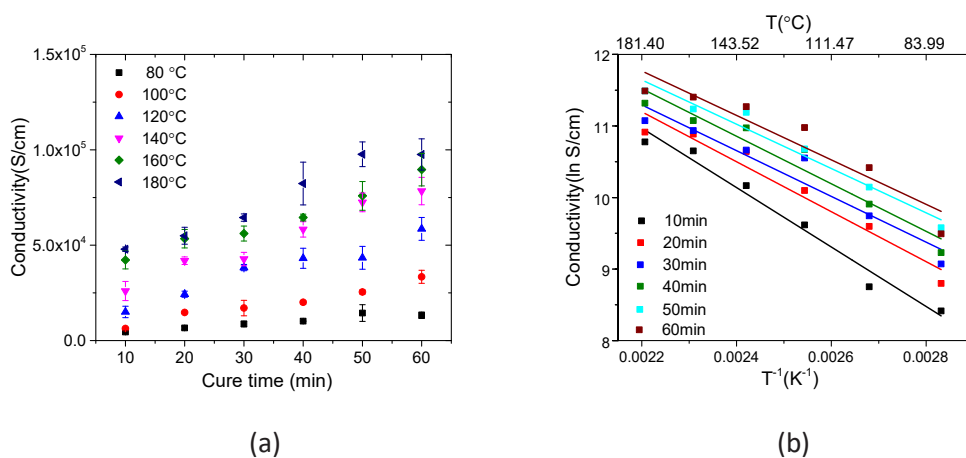


Figure 2.6.1-6. (a) Conductivity variation of the silver conductive wires as a function of cure temperature and cure time. (b) Arrhenius plot of electrical conductivity.

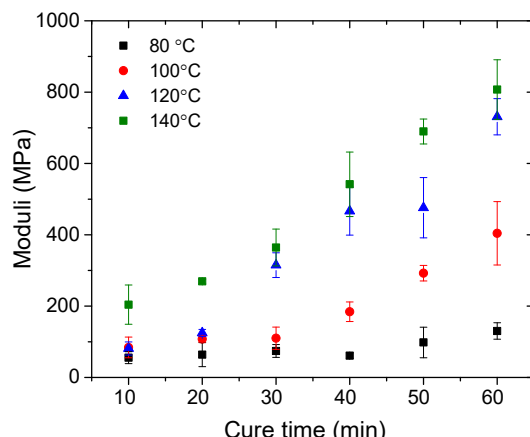


Figure 2.6.1-7. Modulus as function of cure time and cure temperature.

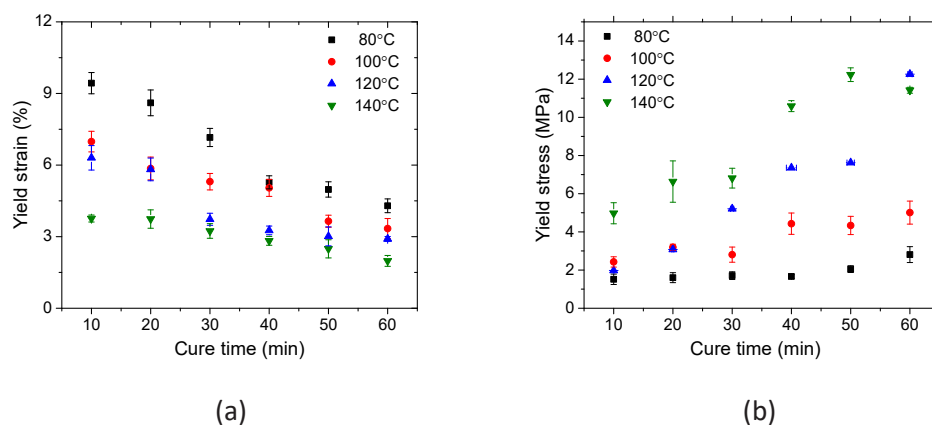


Figure 2.6.1-8. Yielding (point of intersection of tangents) behavior as a function of cure time and temperature (a) yielding strain; (b) yielding stress.

**Yield strain:** We determine the yielding point from the intersection of tangents of the stress-strain curves to obtain the yielding strain and stress. The yielding strains and yielding stresses are summarized in Figure 2.6.1-8. The yielding strain decreases with an increase in curing time and temperature, while the yielding stress increases with an increase in curing time and temperature. In general, the cured silver wires have yielding strains between 2.0% and 9.4%, which is larger than freestanding metal film whose stretch is only 1%-2%[17].

**Elongation:** As in Figure 2.6.1-5 shows, the cured silver wires can withstand a large elongation. During the experiments, the resistance increased into the MΩ range when the wire was subjected to large strains (>300%). Here, for the sake of analysis, we define the ultimate elongation as the strain when the normalized resistance is increased by 100 times ( $R/R_0 < 100$ ) or the silver wire breaks and conductivity is lost, whichever occurs first. Figure 2.6.1-9 shows the ultimate elongation of wires cured under different conditions. In general, we can obtain ~100% ultimate elongation for most curing conditions, which is much larger than sputtered metal films, which have a maximum elongation of around 50% on elastic substrate[18, 19]. This value is also larger than screen printed silver ink, which is about 50%[20]. Figure 2.6.1-9 also shows lower temperature cured silver wire has a longer elongation. In addition, 20min curing time gives the largest ultimate elongation for all the curing temperatures.



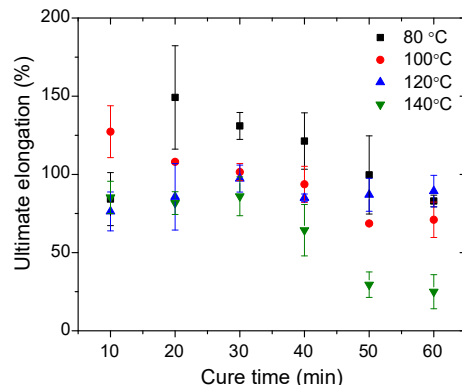


Figure 2.6.1-9. Ultimate elongation ( $R/R_0 < 100$  or sample crack) as a function of cure temperature and cure time.

Figure 2.6.1-10 shows that the silver ink in this study is capable of large elongation. Therefore, if it is deposited on an elastic substrate it may achieve high elastic deformation by embedded printing[21], encapsulation[22], and other methods that have potential for stretchable electrodes application. In addition, we found that for the silver wires we printed, the cure temperature of 80°C -120°C for 10-30min is suitable for 4D printing and soft machine usage, which typically require moderate to large deformation of the substrate materials

Examples of potential applications: Based on the thermal cure condition as well as the electromechanical properties study, we found that as the curing temperature and curing time increased the cured wires became more conductive but less stretchable. The silver wires cured at 80°C for 10-30min are stretchable, and thus can be used for stretchable applications; the silver wires cured at 120°C for 10-20min have good conductivity and are sensitive to applied strain; they are thus good for sensing. In the following, we demonstrate two potential applications.

The printed ink can be embedded into polyJet 3D printed parts, resulting in the fabrication of fully 3D printed, soft and stretchable devices. To fabricate such devices, we used a sequential process, where we printed a substrate using the 3D printer, followed by DIW printing, curing the ink and then encapsulating the ink by subsequent 3D printed layers. This process can be repeated to create multiple layers of embedded ink. As a demonstration, a stretchable LED circuit was printed, shown in Figure 2.6.1-10, where eight ink lines were patterned inside a 60mm long strip of TangoBlack connecting four LEDs in parallel, mimicking a typical ribbon cable with multiple conducting wires. The ink wires were cured at 80°C for 20 minutes in order to yield highly stretchable lines while still maintaining a high conductivity to illuminate the LEDs at a reasonable power output (~500mW). It was possible to stretch the cable by as much as 45% during testing. The online video shows the stretching process.

A flexible sensor was also printed. Here, a single layer serpentine strain gauge was printed inside of the elastomer ring. The ink line was cured at 120°C for 20 minutes, a more suitable curing condition for sensor applications. The fabricated sensor and the typical operating response can be seen in Figure 2.6.1-11. The sensor was tested in two bending configurations, 1) straight and 2) partially bent. When the finger bends, it bends the top face of the ring and stretches the conductive wire, causing an increase of the resistance. When the finger returns to the straight position, the resistance drops. The video in the online material shows the real time resistance change as the finger bends and returns.



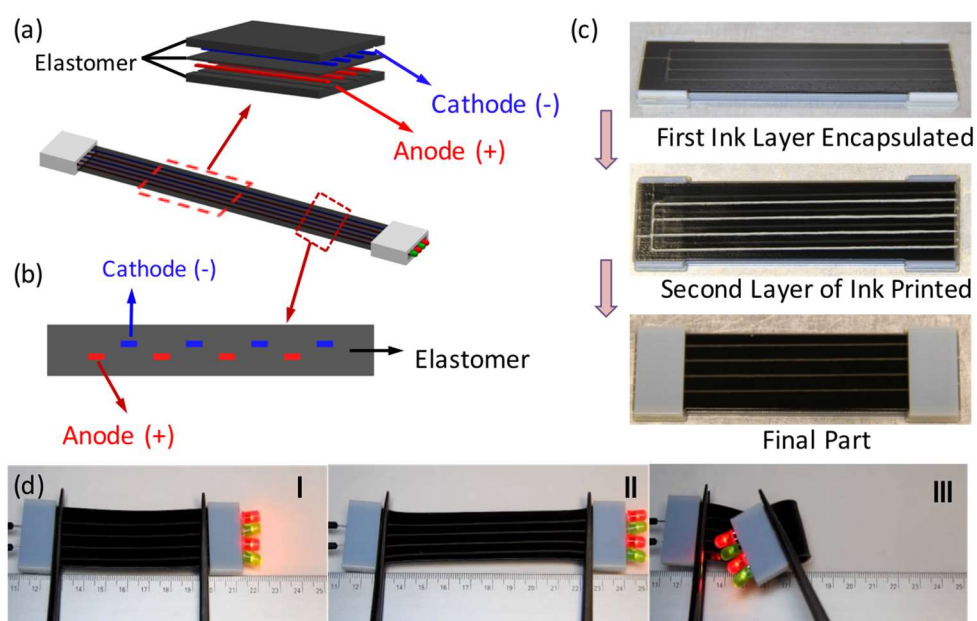


Figure 2.6.1-10. Fully printed stretchable cable by embedded silver wire into polyJet 3D printed parts: (a) The design of the cable. (b) The cross-section of the stretchable part of the cable. (c) The images of the printed part during the printing process. (d) Embedded silver wires in elastomer as circuits during stretching. Images of the printed cable under tensile strain of ( I ) 0% and (II) 40% and (III) under folding.

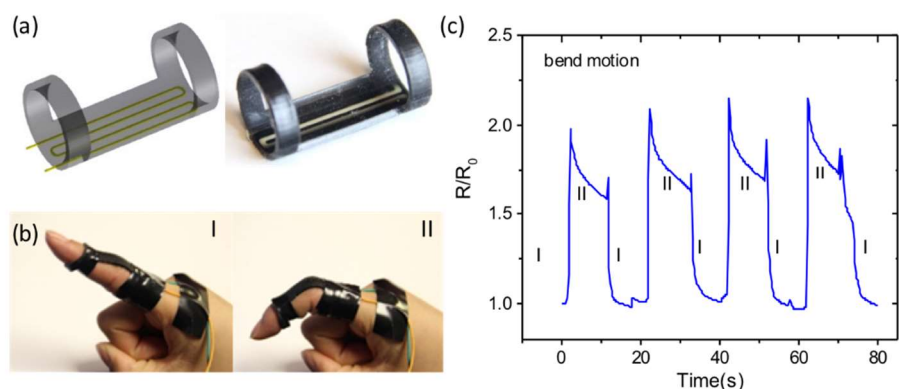


Figure 2.6.1-11. Detection of finger motion with all printed stretchable sensor. (a) Schematic and printed flex sensor. (b) Images of a bending sensor on a finger-ring mounted on the forefinger, in straight (I) and bend (II) positions. (c) Change in resistance of a representative gauge during four bending cycles.

## 2.7 Design Optimization

To develop, implement, and study our topology optimization framework, we first identified and implemented an accurate and efficient solid shell finite element formulation in our in-house design optimization software platform. The solid shell formulation allows modeling and predicting the mechanical phenomena in composite plates and shells with complex material arrangements. We further developed and studied a density method for optimizing active composites. This study revealed significant shortcomings of the density approach for the design of PACS. Therefore, we focused on developing and applying a LSM-XFEM approach for finding the optimal arrangement of active materials within an inactive phase. To facilitate optimizing PACS, we develop first a simplified PAC model amenable to iterative design optimization procedures. We refined and applied our LSM-XFEM approach for finding the optimal arrangement of active materials within an inactive phase. These studies involved printing samples of optimized PACs and verifying their behavior experimentally. While the simplified PAC model captured the basic shape memory polymer phenomena, it relied on a small strain assumption, which severely limits the applicability of the optimization approach. Therefore, we extended our simplified PAC model to account for finite strains. We further refined our models and LSM-XFEM optimization approach for finding the optimal arrangement of heterogeneous materials with imperfect bonding between the material phases. A foundational study on design sensitivities with the Heaviside enrichment strategy was a significant byproduct of this work.

### 2.7.1 Solid Shell Finite Element Formulation and Implementation

Conventional finite element formulations of plate and shell models are based on a degeneration principle, i.e. the behavior in thickness direction is modeled explicitly and the structural response is represented by the deformations of the mid-plane. While computationally efficient and sufficiently accurate for regular material arrangements, this approach is inadequate for complex material layouts and complicates modeling complex 3D constitutive models. These issues can be mitigated by using solid shell elements which are built upon a 3D formulation of the mechanical model. However, standard solid elements suffer from various locking phenomena and require highly resolved meshes, in particular in thickness direction, to predict accurately the response of thin structures. Solid shell elements mitigate this issue by enriching the strain approximation via Assumed Natural Strain (ANS), Enhanced Assumed Strain (EAS) concepts, and tuned numerical integration procedures.

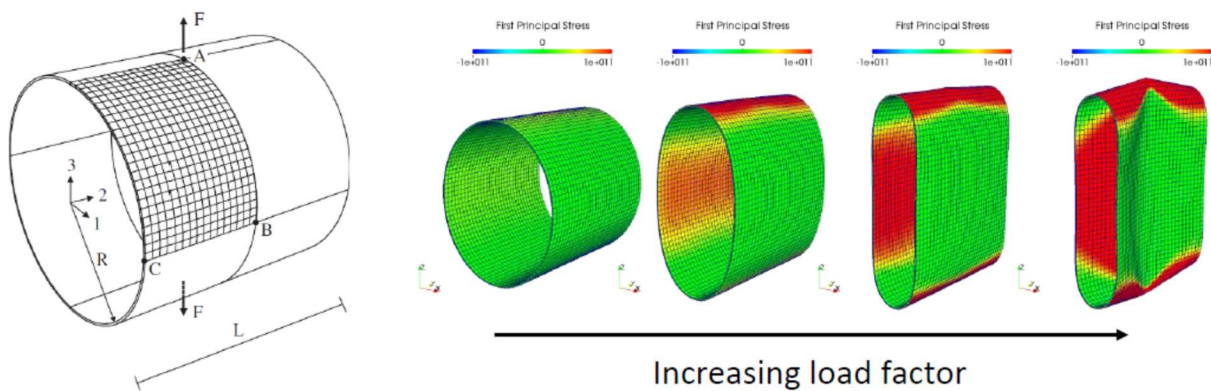


Figure 2.7.1-1. Benchmark example for solid shell element implementation: Cylinder buckling under tensile forces.

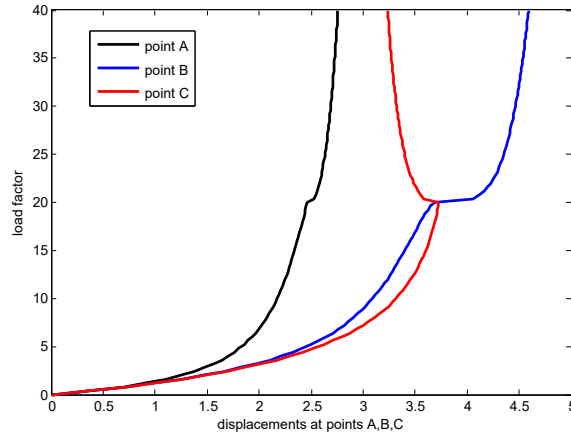


Figure 2.7.1-2: Load-displacement curves for points A, B, and C on cylinder; see Figure 2.7.1-1.

To enable the modeling of complex material layouts by finite elements, we identified and implemented a solid shell element formulation that does not rely on simplifying assumption of the material layout and that can be integrated into an XFEM formulation. After studying the literature and implementing 6 of the most promising formulations into a MATLAB prototype code, we identified the formulation of Schwarze and Reese [23, 24] as best suited for meeting the needs of this project. This solid shell formulation was implemented in our in-house finite element & optimization software platform, verified against a comprehensive suite of benchmark problems, and has been used in the design optimization studies described below. Figure 2.7.1-1 shows one of the benchmark problems studied. A cylinder is subject to two vertical forces acting in opposite directions. The cylinder undergoes a highly nonlinear behavior as the load-displacement curves for the points A, B, and C illustrate; see Figure 2.7.1-2. Our implementation matches perfectly the results reported in [24].

## 2.7.2 Optimization of Printed Active Composites by the Density Approach

We first explored the capabilities to optimize the material layout of printed active composites with the density approach. We describe the response of the composite via a homogenized macroscopic material model assuming small strains. The material properties are derived from a microscopic model using Mori-Tanka's homogenization approach [25, 26]. The micro-scale material architecture consists of unidirectional SMP fibers embedded in an isotropic inactive matrix. The shape memory effect of the active fibers is modeled via incompressible eigenstrains which approximate residual strains due to the training load via the magnitude and orientation of the eigenstrains. The fiber volume fraction and the fiber orientations were considered optimization variables and their optimum spatial distribution determined in the optimization process.

In our design studies, we determined the optimal design of printed active composites such that in the actuated stage, i.e. after releasing the training loads at  $T_L$ , the deformed shape of a composite plate matches a target shape. An example is shown in Figure 2.7.2-1. The objective of the problem is to find the optimum distributions of fiber volume fraction and in-plane fiber orientation, i.e. in the x-y plane, such that a square composite plate assumes a parabolic shape upon actuation, i.e. due to the shape memory behavior of the fibers. The design domain is restricted to the lower half of the plate. A residual fiber strain in the x-direction of 4% and in the y- and z-direction of -2% is assumed to capture the training loads. Figure 2.7.2-1 shows the optimum distributions of fiber volume fraction and in-plane fiber orientation, as well as the deformed and target shapes. Note the fiber orientations are visualized by drawing "streamlines" along the fiber directions. The optimized composite layout results in an actuated shape that matches well the

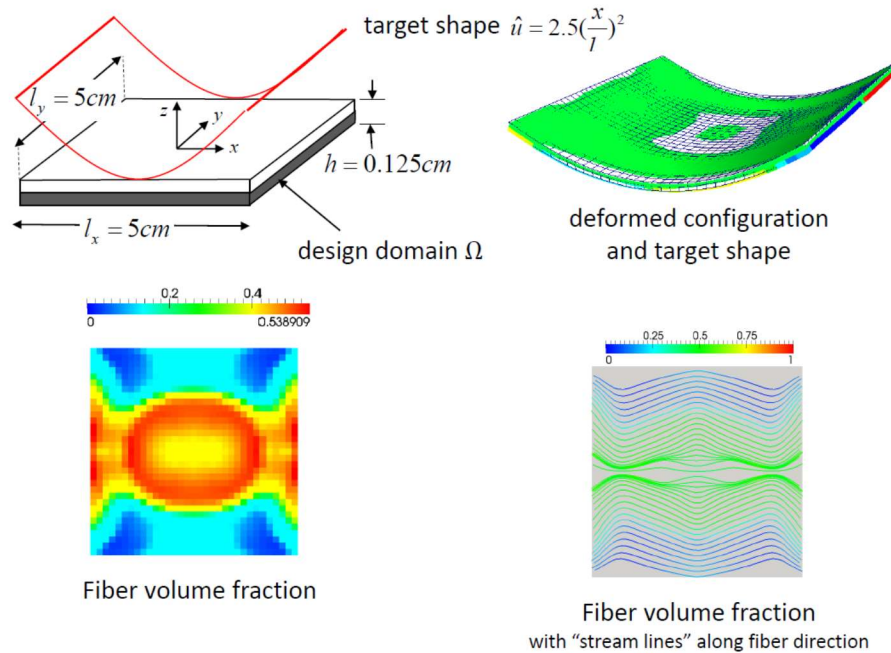


Figure 2.7.2-1. Optimization of fiber volume fraction and fiber orientation for shape matching.

target shape. While a constraint on the maximum total fiber volume fraction of 50% was imposed, this constraint was not active in the final design. Studies on different target shapes were performed and also showed that a broad range of target shapes can be matched with great accuracy through optimizing the fiber volume fraction and fiber orientation.

We studied methods for converting the optimized fiber volume fraction and fiber orientations into a printable design. To this end, we represented individual fibers by tubes which were generated as streamlines along the principal stiffness directions. The tube radius was defined as a function of the local fiber volume fraction. The parameters of this function and the spacing of the fibers were tuned manually to match the total fiber volume fraction in the plate. We then generated surface meshes for the tube/matrix interfaces which were used by the printing software of the Object 260 printer to fabricate the composite; see Figure 2.7.2-2. However, preliminary experimental studies suggest that this heuristic approach is prone to introducing significant discrepancies between the mechanical model used for optimization and the model extracted for printing.

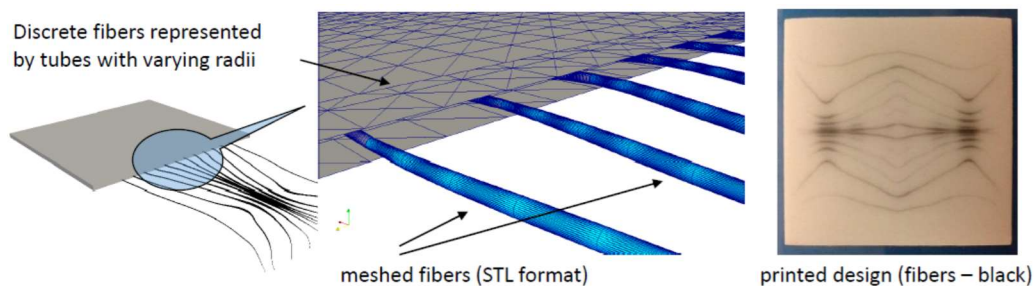


Figure 2.7.2-2. Realization of optimized active composite.

### 2.7.3 Simplified PAC Model for Design Optimization

To accurately model the response of PACs, in general large deformations and a complex thermo-mechanical constitutive behavior need to be considered, leading to a nonlinear non-conservative multi-physics model. Constitutive models for accurately describing the SM cycle of amorphous shape memory polymers (SMPs) have been developed in the first year of this project and are described in the previous project report. Considering these models within the topology optimization process significantly increases the algorithmic complexity and the computational cost. To create an analysis approach more amenable for design in terms of computational speed and ease of implementation but with acceptable fidelity, we developed two simplified mechanical models. We studied the accuracy of these PAC models against experimental results, and compared the optimization results obtained using these models. This work was published in *K. Maute, A. Tkachuk, J. Wu, H. J. Qi, Z. Ding, and M.L. Dunn. 2015. Level Set Topology Optimization of Printed Active Composites. ASME Journal of Mechanical Design, 137: 111704-1, 2015.*

Both simplified PAC models account for stress relaxation and the resulting residual stresses via eigenstrains that can vary with position. These models lump the complex nonlinear thermo-mechanical phenomena occurring during a thermo-mechanical cycle into an effective inelastic strain, i.e. eigenstrain. Both PAC models assume infinitesimal strains and a linear material behavior, but they differ in the approximation of the eigenstrains in the active phase. The more accurate model predicts the eigenstrains by resolving the strain field in the PAC at the training stage due to the programming loads at temperatures above the glass transition temperature. The simpler model assumes a uniform eigenstrain in the active phase which is predicted analytically. Subsequently, we first describe the more accurate model which is then simplified to the model with uniform eigenstrains. Both models were compared against experimental data.

We consider the response of the PAC at the training stage subject to programming loads, referred to stage (i), and after the programming loads are removed, referred to stage (ii). The effects of the phase transition of the active phase are modeled via eigenstrains, which are computed in stage (i) and applied in stage (ii), and a change in Young's modulus. The residuals of the static equilibrium equations in both stages are written in weak form as follows:

$$\bar{W}_S = \sum_{p=1}^2 \left( \int_{\Omega^p} \delta \bar{\varepsilon}_{ij}^p \bar{\sigma}_{ij}^p d\Omega - \int_{\bar{\Gamma}_T^p} \delta \bar{u}_i^p \bar{F}_i^p d\Gamma \right) = 0, \quad (2.7.3-1)$$

$$\hat{W}_S = \sum_{p=1}^2 \left( \int_{\Omega^p} \delta \hat{\varepsilon}_{ij}^p \hat{\sigma}_{ij}^p d\Omega - \int_{\hat{\Gamma}_T^p} \delta \hat{u}_i^p \hat{F}_i^p d\Gamma \right) = 0, \quad (2.7.3-2)$$

with

$$\bar{u}_i^p = \bar{U}_i^p \text{ on } \bar{\Gamma}_U^p, \quad \hat{u}_i^p = \hat{U}_i^p \text{ on } \hat{\Gamma}_U^p, \quad (2.7.3-3)$$

where  $(\bar{\cdot})$  denotes quantities in stage (i) and  $(\hat{\cdot})$  in stage (ii). Passive and active phases are denoted with superscripts ``1" and ``2". The displacement vector, the strain tensor, and the stress tensor are denoted by  $u_i^p$ ,  $\varepsilon_{ij}^p$  and  $\sigma_{ij}^p$ , respectively. External forces,  $F_i^p$ , act along the boundary  $\Gamma_T^p$ , and prescribed displacements,  $U_i^p$ , are applied at the boundary  $\Gamma_U^p$ . Note the boundary conditions typically differ between stages (i) and (ii). The material behavior at the two stages is described by the following constitutive equations:

$$\bar{\sigma}_{ij}^p = \bar{C}_{ijkl}^p \left( \bar{\varepsilon}_{ij}^p - \alpha^p \delta_{ij} \Delta \bar{T} \right), \quad (2.7.3-4)$$



$$\hat{\sigma}_{ij}^p = \hat{C}_{ijkl}^p \left( \hat{\varepsilon}_{ij}^p - f^p \bar{\varepsilon}_{ij}^p - \alpha^p \delta_{ij} \Delta \hat{T} \right), \quad (2.7.3-5)$$

where  $\hat{C}_{ijkl}^p$ ,  $f^p$ , and  $\alpha^p$  denote the elastic tensor, the strain fixity and the coefficient of thermal expansion, respectively. The Young's modulus of the active phase increases as the material transitions from a rubbery state in stage (i) to a glassy state in stage (ii). The elastic tensor of the passive phase is assumed constant. The strains of the programming state (i) are introduced as eigenstrains in the constitutive equation for stage (ii). For the passive phase the fixity is assumed negligible, i.e.  $f^1 = 0.0$ . In the following, we ignore thermal strains as the mismatch in  $\alpha^p$  is insignificant for the materials considered in this study.

Subsequently, we refer to the model described above as *two-stage* model. This model can be further simplified by approximating the strains in the training stage (i) by a uniform strain distribution. Assuming a homogeneous material and for simple geometries and programming loads,  $\bar{\varepsilon}_{ij}^p$  can be approximated analytically via kinematic compatibility considerations. As before, the fixity in the passive phase is assumed to vanish. Note that this simplification requires only modeling the static equilibrium of stage (ii). We refer to this model as "single stage" model.

The PAC models introduced above are built upon several simplifying assumptions. To investigate the ability of these models to capture the fundamental characteristics of the PAC response we consider the simple configuration of Figure 2.7.3-1, which was studied experimentally [29]. The active fibers are made of *Shore95* and exhibit a SM behavior; the passive phase is *Tango black+*. In the programming stage (i), the composite plate is subject to prescribed displacements  $\pm 0.5\bar{U}_1$  at the front and rear faces. In the

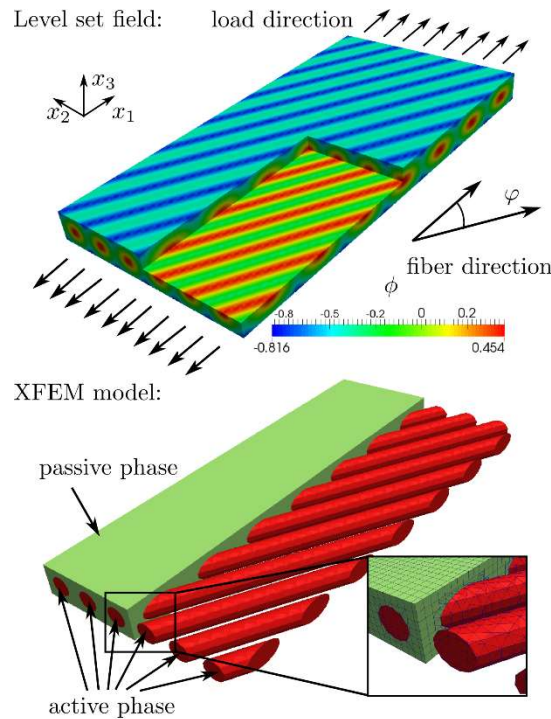


Figure 2.7.3-1: Composite plate model for PAC validation study.

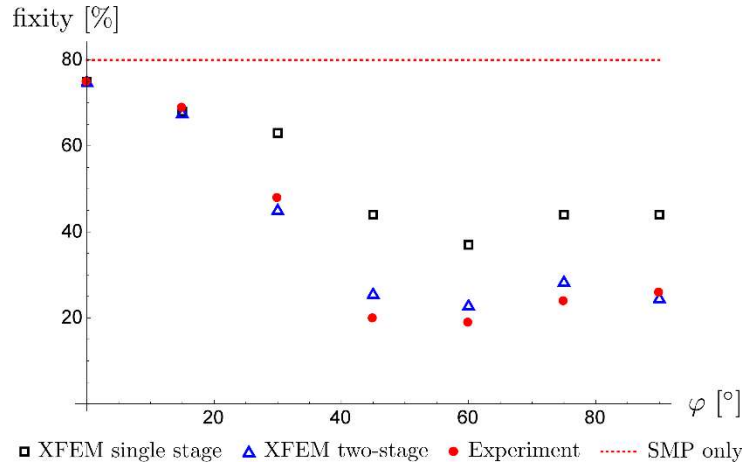


Figure 2.7.3-2: Comparison of experimental and XFEM results: fixity over fiber orientation.

programmed stage (ii) it is clamped at its center to suppress rigid body motion. In the case of the single stage model, the eigenstrain is assumed to be  $\bar{\varepsilon}_{ij} = \text{diag}[\bar{U}_1 / L, -0.5\bar{U}_1 / L, -0.5\bar{U}_1 / L]$ , which is consistent with the programming displacements and incompressible material. Details on the level set function that described the fiber layout, the XFEM model, and the material properties are given in Maute et al. [30].

The response of the PAC is studied for 7 different fiber orientations. The experimental results of KM-Ref1 and the XFEM predictions are compared in Figure 2.7.3-2. The fixity of the composite plate is measured by the elongation of the plate in the programmed stage (ii) relative to prescribed elongation  $\bar{U}_1$  at the programming stage (i). The fixity parameter of the active phase is calibrated by considering the experimental results for a plate made of the active phase only; see the dotted line in Figure 2.7.3-2. Comparing the experimentally measured and numerical results shows that the two-stage model captures well the PAC response across a wide range of fiber orientations. However, the single stage model leads only to acceptable results for fiber angles up to  $\varphi = 20^\circ$ , because the assumption for the eigenstrain distribution is valid only for small differences between training load and fiber directions.

Given the complexity of the material behavior and the uncertainty of the experimental results[31], the two-stage model and, to a lesser extent, the single stage model showed satisfactory agreement with the experimental measurements for the example considered above. This motivated the application of these PAC models to the design optimization problems presented in the following section. However, additional validation problems need to be studied in the future to increase the confidence in the proposed PAC model. Future studies should also include problems that exhibit large out-of-plane deformations and more complex inclusion geometries.

#### 2.7.4 Optimization of PACs by LSM-XFEM topology optimization

We studied the proposed LSM-XFEM approach for PACs with several design problems, using the single stage and two-stage PAC models. Here we report on three of them. In the first two examples, the target shape promotes a plate bending type response of increasing complexity. The third example explores the ability to generate localized deformations. Measurements for 3D printed realizations of the optimized designs were compared against numerical predictions of the programmed shape at stage (ii). The design studies illustrated the ability of the proposed optimization approach to find non-trivial designs. The comparison against experimental measurements motivates future research on improving the accuracy of the PAC model.



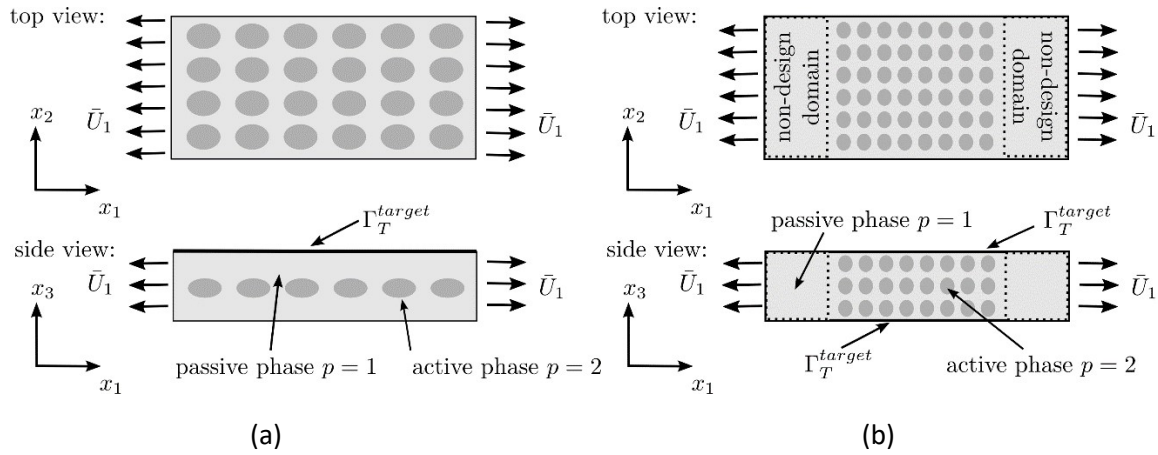


Figure 2.7.4-1. (a) Setup for 3D PAC layout optimization problem -- plate bending configuration. (b) Setup for 3D PAC layout optimization problem -- localized deformation configuration.

For all examples, we study the formulation of the optimization problem: we minimize the square of the difference between the displacements in the programmed stage (ii),  $\hat{u}_i$ , and a target deformation  $u_i^{target}$  integrated over the surface  $\Gamma_T^{target}$  where the deformations are monitored. This yields the following contribution to the objective function:

$$\mathcal{F}^{target} = \int_{\Gamma_T^{target}} w_i (\hat{u}_i - u_i^{target})^2 d\Gamma, \quad (2.7.4-1)$$

where  $w_i$  denotes the weighting factors for the components of the displacement vector. To prevent the formation of small geometric features and irregular shapes we augment the objective  $\mathcal{F}^{target}$  with the following regularization term that penalizes the perimeter of the phase boundary:

$$\mathcal{F}^{reg} = \gamma_{per} \int_{\Gamma_{1,2}} d\Gamma, \quad (2.7.4-2)$$

where  $\gamma_{per}$  denotes the perimeter penalty factor. The value of the perimeter penalty factor is chosen to smooth the surface of the phase boundary without significantly affecting the shape matching objective  $\mathcal{F}^{target}$ . The choice of  $\gamma_{per}$  is problem dependent and has been determined iteratively. While for the problems studied penalizing the perimeter often led to satisfactory results.

The geometry of the samples and boundary conditions in the programming stage (i) are depicted in Figures 2.7.4-1a and b for the plate bending and for the localized deformation problems, respectively. Details on the dimensions and material parameters are given in Maute et al.[30]. The difference between the target and programmed shape is measured at the upper surface for the first three examples and at the upper and lower surfaces for the fourth problem. The analytical expressions for the target displacements are given in Table 2.7.4-1 and are defined with respect to a coordinate system located at the center of the design domain.

In the programming stage (i), the samples are stretched by 6% by applying prescribed displacements on front and rear faces. In the programmed stage (ii), the samples are supported at their center to prevent rigid body motion. In all examples, the design domain is discretized by 8-node, tri-linear finite elements. Details on the mesh sizes and solver strategies are given in Maute et al. [30].

Table 2.7.4-1. Target shapes for PAC layout problems.

Case	$u_3, mm$
Parabolic bending	$-2.4 \left( \frac{x_1}{20} \right)^2$
Twisted parabolic bending	$-4.8 \left( \frac{x_1}{40} \right)^2 \sin \left( \frac{\pi x_2}{40} \right)$
Localized deformation	$-0.1 \text{ sign}(x_3) \max(0, 1 - (x_1^2 + x_2^2) / 25)$

The level set function is discretized by the same mesh used for the PAC analysis. The nodal level set values are defined as functions of the optimization variables, using a linear filter[30]. The resulting parameter optimization problems are solved by the Globally Convergent Method of Moving Asymptotes[32] without sub-cycling. The design sensitivities of the objective and constraints are determined by the adjoint method. The designs are initialized with uniform arrays of cuboids of either active or passive material, surrounded by material of the other phase.

The optimized designs were 3D printed by exporting the triangulated phase boundaries of the XFEM models for each phase separately, using the STereo Lithography (STL) file format. To this end, we extracted the XFEM mesh used for integrating the weak form of the governing equations. Note that this triangulation is aligned with the phase boundaries and thus each STL file defines the volume of one distinct phase. The STL files were loaded into the software interface of an Objet Connex 260 printer and a material type was assigned to each volume associated with an STL file. The printer software optimizes the material layout along the phase boundaries for improved bonding and material strength. The printed PAC sample were subject to the thermo-mechanical programming cycle described above and the programmed shape in stage (ii) was measured. Note that the experimental results reported here mainly serve as a proof of concept but lack the accuracy needed for rigorous quantitative comparisons between predictions and experimental measurements.

In Figures 2.7.4-2, Figure 2.7.4-3, and Figure 2.7.4-4 the results for the three problems are shown. In each figure the topology optimization result for the single and two-stage models are shown with the active phase colored in dark gray; the bright gray color is the inactive phase. The figures also show the finite element prediction of the two-stage optimized design with the colors representing the  $\hat{u}_3$  displacement component. The printed design is shown in the second row. Note for visualization purposes, we print the sample with a transparent matrix material and a dark SMP material. However, the mechanical test is performed with *Tango Black+* and *Shore95*. The deformed sample after activation is shown for the first two examples. However, as our experimental instrumentation lacked the ability to sufficiently resolve sub-millimeter deformations, we were not able to obtain meaningful measurements for the third problem.

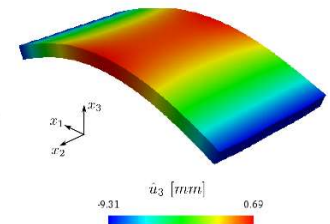
Single stage design:



Two-stage design:



Two-stage design:



Sample 3D printed with transparent passive phase:

Programmed sample at stage (ii):

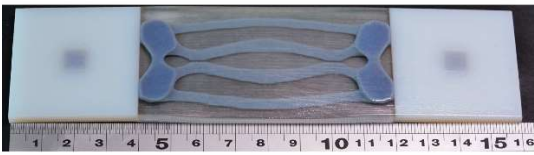


Figure 2.7.4-2: Optimization results for parabolic bending target shape.

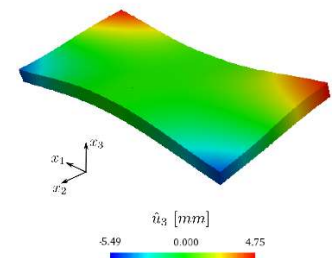
Single stage design:



Two-stage design:



Two-stage design:



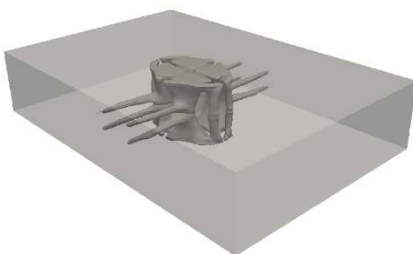
Sample 3D printed with transparent passive phase:

Programmed sample at stage (ii):

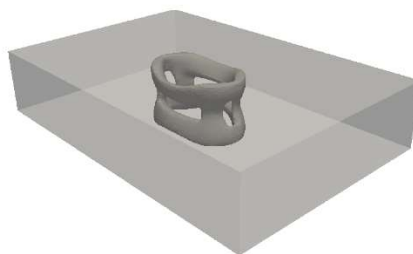


Figure 2.7.4-3: Optimization results for twisted parabolic bending target shape.

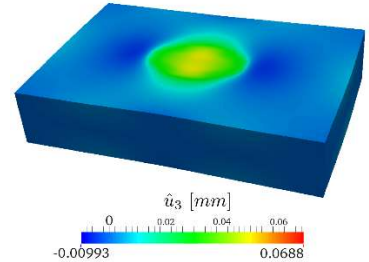
Single stage design:



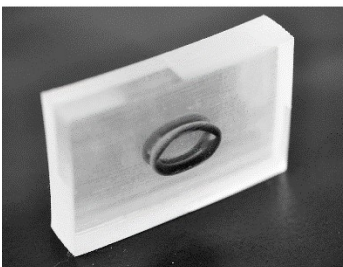
Two-stage design:



Two-stage design:



Sample 3D printed with transparent passive phase:



Printed active phase:



Figure 2.7.4-4: Optimization results for localized deformation target shape.

The numerical results demonstrated that the proposed optimization approach provides a crisp and well resolved description of the phase boundaries. Surface meshes of the phase boundaries could be easily extracted from the XFEM model and directly exported into the software interface of 3D printers without the need for any form of post-processing.

For all design problems studied with a bending type target deformation, the target shapes could be matched with acceptable accuracy. Both PAC models resulted in conceptually similar designs with sophisticated spatial arrangements of the active phase. The results for the example with a localized target deformation suggest that creating localized deformations is a challenging design problem even if the amplitude of the target design is small. Nevertheless, the examples studied to date demonstrate the ability of the proposed optimization method to find non-trivial and non-intuitive designs. Analyzing the designs optimized with the single stage PAC model by the more accurate two-stage PAC model showed that the shape mismatch is significantly larger than the one of the designs optimized with the two-stage model, see[30]. This observation suggests that the accuracy of the PAC model has a noticeable influence on the optimization results and therefore an accurate PAC model should be used for topology optimization.

The comparison of the XFEM predictions against experimental measurements for the optimized designs of the examples with a bending type target deformation suggests that the proposed two-stage PAC model may be appropriate for design purposes but insufficient to accurately predict the PAC response in the presence of large deformations. During the third year of this project, more accurate but still computationally tractable PAC models will be researched and integrated into the proposed optimization framework. Furthermore, the perimeter constraint was found to be insufficient to explicitly control the local feature size of the active phase. Thus, methods will be explored to constrain the minimum feature size and to account for the resolution limits of 3D printers.

#### 2.7.5 Finite Strain PAC Model for Design Optimization

The small strain assumption on which the PAC models described in Section 2.7.3 are based is not valid for the level of training loads used for practical applications and does not capture accurately the deformations achieved upon activation. Therefore, we expanded our simplified PAC model onto finite strains and studied the influence of the finite strain model on the optimum material layout. This study is currently completed and a paper on the results of these studies is currently in preparation.

**Finite strain PAC model:** While there are several constitutive models available to accurately describe the behavior of amorphous shape memory polymers (SMPs), these models are too complex and too computationally costly for design optimization. Previously, we have created an analysis approach more amenable for design in terms of computational speed and ease of implementation but with acceptable fidelity. This approach accounts for stress relaxation and the resulting residual stresses via eigenstrains that can vary with position. The eigenstrains are predicted by resolving the strain field in the PAC at the training stage due to the programming loads at temperatures above the glass transition temperature. However, our previous PAC model assumes infinitesimal strains and a linear material behavior. To overcome this limitation, we developed a nonlinear PAC model which accounts for finite strains, but is still considerably simpler than constitutive models that describe the phase transition and the associated changes in material properties during the shape memory cycle.

We consider the response of the PAC at the training stage subject to programming loads, referred to stage (i), and after the programming loads are removed, referred to stage (ii). The effects of the phase transition of the active phase are modeled via eigenstrains, which are computed in stage (i) and applied in stage (ii), and a change in Young's modulus. The residuals of the static equilibrium equations in both stages are written in weak form using a total Lagrangian formulation as follows:

$$\bar{W}_S = \sum_{p=1}^2 \left( \int_{\Omega_0^p} \delta \bar{F}_{ij}^p \bar{P}_{ij}^p d\Omega - \int_{\bar{\Gamma}_{0,T}^p} \delta \bar{u}_i^p \bar{T}_i^p d\Gamma \right) = 0, \quad (2.7.5-1)$$

$$\hat{W}_S = \sum_{p=1}^2 \left( \int_{\Omega_0^p} \delta \hat{F}_{ij}^p \hat{P}_{ij}^p d\Omega - \int_{\hat{\Gamma}_{0,T}^p} \delta \hat{u}_i^p \hat{F}_i^p d\Gamma \right) = 0, \quad (2.7.5-2)$$

with

$$\bar{u}_i^p = \bar{U}_i^p \text{ on } \bar{\Gamma}_{0,U}^p, \quad \hat{u}_i^p = \hat{U}_i^p \text{ on } \hat{\Gamma}_{0,U}^p, \quad (2.7.5-3)$$

where  $(\bar{\cdot})$  denotes quantities in stage (i) and  $(\hat{\cdot})$  in stage (ii). Passive and active phases are denoted with superscripts ``1" and ``2". The displacement vector, the deformation gradient tensor, and the 1<sup>st</sup> Piola-Kirchhoff stress tensor are denoted by  $u_i^p$ ,  $F_{ij}^p$  and  $P_{ij}^p$ , respectively. External forces,  $T_i^p$ , act along the boundary  $\Gamma_{0,T}^p$  in the reference configuration, and prescribed displacements,  $U_i^p$ , are applied at the boundary  $\Gamma_{0,U}^p$ . Note the boundary conditions typically differ between stages (i) and (ii). For the sake of simplicity, the material behavior at the two stages is described by a Saint-Venant Kirchhoff model:

$$S_{ij}^p = \lambda E_{kk} \delta_{ij} + 2\mu E_{ij}, \quad (2.7.5-4)$$

where  $S_{ij}^p$  and  $E_{ij}^p$  denote the 2<sup>nd</sup> Piola-Kirchhoff stress tensor and the Green-Lagrange strain tensor, respectively. Other hyperelastic material models can be easily accommodated. The Lamé constants are  $\lambda$  and  $\mu$ . Green-Lagrange strain tensors is computed for follows:

$$E_{ij}^p = \frac{1}{2} \left( F_{ki}^{e,p} F_{kj}^{e,p} - \delta_{ij} \right), \quad (2.7.5-5)$$

where  $F_{ij}^{e,p}$  is the elastic contribution of the deformation gradient tensor. In the training stage, we assume that there are no inelastic contributions to the total deformation gradient tensor,  $\bar{F}_{ij}^p$ , such that:

$$\bar{F}_{ij}^{e,p} = \bar{F}_{ij}^p = \delta_{ij} + \frac{\partial \bar{u}_i}{\partial X_j}, \quad (2.7.5-6)$$

where  $X_j$  denotes the location of a material point in the reference configuration. In the actuation stage (ii), we model the shape memory effect via a multiplicative decomposition of the deformation gradient tensor:

$$\hat{F}_{ij}^p = \hat{F}_{ij}^{s,p} \hat{F}_{ij}^{e,p} \quad \text{with} \quad \hat{F}_{ij}^p = \delta_{ij} + \frac{\partial \hat{u}_i}{\partial X_j}, \quad (2.7.5-7)$$

where the inelastic contribution,  $\hat{F}_{ij}^{s,p}$ , represents the eigenstrains due to deformations at the programming stage and is modeled as follows:

$$\hat{F}_{ij}^{s,p} = f^p \bar{F}_{ij}^p, \quad (2.7.5-8)$$

where  $f$  is the strain fixity parameter. Note that this approach is similar to the proposed in [34] but does not require modeling the phase transition. Instead, the fixity parameter in (8) represents the complete stress relaxation process and needs to be calibrated for particular thermos-mechanical cycling processes. The Young's modulus of the active phase increases as the material transitions from a rubbery state in stage (i) to a glassy state in stage (ii). The elastic tensor of the passive phase is assumed constant. For the passive phase the fixity is assumed negligible, i.e.  $f^1 = 0.0$ .

**XFEM discretization of PAC model:** The above finite strain PAC model was discretized by a Heaviside enriched formulation of the XFEM. In previous studies, we have shown that this enrichment strategy provides great flexibility and accuracy in modeling heterogeneous materials [27, 28]. However, as the Heaviside enrichment does not intrinsically guarantee the continuity of the displacement fields across material interfaces, additional continuity constraints need to be introduced. In this work, we use a Nitsche formulation [35]. Furthermore, the XFEM problem may become ill-conditioned when elements are interested such that small volumes of one phase are generated. These configurations do not only cause issues for solving the set of nonlinear equations, e.g. by Newton's method, but also lead to stress oscillations along the interface. The latter may severely affect the stability of the XFEM formulation of finite strain problems. To overcome these stability issues, we adopted and extended the so-called ghost penalization approach of Burman and Hansbo [36, 37] for finite strain problems.

The weak form of the governing equations augmented by Nitsche's formulation of the interface continuity condition and ghost stabilization can be written as follows:

$$\begin{aligned} \bar{W}_S = & \sum_{p=1}^2 \left( \int_{\Omega_0^p} \delta F_{ij}^p P_{ij}^p d\Omega - \int_{\bar{\Gamma}_{0,T}^p} \delta u_i^p T_i^p d\Gamma \right) \\ & + \sum_{p=1}^2 \sum_{F^p \in F_{cut}^p} \gamma_{GP} \int_{F_0^p} \left[ \delta \left( \frac{\partial u_i^p}{\partial X_j} \right) n_j \right] \left[ \left( \frac{\partial u_i^p}{\partial X_k} \right) n_k \right] dF \\ & - \int_{\Gamma_{0,12}^{12}} [\delta u_i] \{ P_{ij}^p n_j \} d\Gamma + \int_{\Gamma_{0,12}^{12}} [\delta P_{ij}^p n_j] \{ u_i \} d\Gamma + \sum_{e \in E_{cut}} \gamma_N^e \int_{\Gamma_{0,12}^{12}} [\delta u_i] [\delta u_i] d\Gamma, \end{aligned} \quad (2.7.5-9)$$

where the second row is the contribution of the ghost penalty formulation and the terms in the third row are due to the Nitsche interface condition. The symbol  $[\cdot]$  denotes the jump across an interface; the symbol  $\{\cdot\}$  represents an averaged value.

The ghost penalization measures the jump of the displacement gradients across an element interfaces, projected onto the interface normal. The set  $F_{cut}^p$  includes all interfaces between elements where at least one of the elements is intersected and the interface contains the phase p, i.e.  $F^p \cap \Omega_p \neq \emptyset$ . Note that these integrals are independent of the intersection configuration but are evaluated across the entire element face  $F^p$ , such that the degrees of freedom interpolating the displacement field  $u_i^p$  maintain a non-vanishing zone of influence. The penalty parameter  $\gamma_{GP}$  controls the strength of the ghost penalty term. The larger  $\gamma_{GP}$ , the smoother the spatial gradients of the displacement field and, thus, the stress field along the material interfaces, increasing the stability of the XFEM formulation at the cost of accuracy.

**Design optimization study with nonlinear of PAC model:** To investigate the influence of accounting for finite strains on the optimal PAC layout, we revisited a design study we performed earlier using our linear



PAC model [30]. The design problem is to find the arrangement of the SMP phase within a rubbery passive matrix such that a plate assumes a target shape after activation. To this end, we minimize the square of the difference between the displacements in the programmed stage (ii),  $\hat{u}_i$ , and a target deformation  $u_i^{\text{target}}$  integrated over the surface  $\Gamma^{\text{target}}$  where the deformations are monitored. This yields the following contribution to the objective function:

$$\mathcal{F}^{\text{target}} = \int_{\Gamma^{\text{target}}} w_i \left( \hat{u}_i - u_i^{\text{target}} \right)^2 d\Gamma, \quad (2.7.5-10)$$

where  $w_i$  denotes the weighting factors for the components of the displacement vector. To prevent the formation of small geometric features and irregular shapes we augment the objective  $\mathcal{F}^{\text{target}}$  with the following regularization term that penalizes the perimeter of the phase boundary:

$$\mathcal{F}^{\text{reg}} = \gamma_{\text{per}} \int_{\Gamma_{1,2}} d\Gamma, \quad (2.7.5-11)$$

where  $\gamma_{\text{per}}$  denotes the perimeter penalty factor. The value of the perimeter penalty factor is chosen to smooth the surface of the phase boundary without significantly affecting the shape matching objective  $\mathcal{F}^{\text{target}}$ . The choice of  $\gamma_{\text{per}}$  is problem dependent and has been determined iteratively. While for the problems studied penalizing the perimeter often led to satisfactory results.

The geometry of the plate and the boundary conditions in the programming stage (i) are depicted in Figures 2.7.5-1. The target shape represents a parabola with:

$$u_3^{\text{target}} = -2.4 \left( \frac{x_1}{20} \right)^2 \quad w_1 = w_2 = 0 \quad w_3 = 1 \quad (2.7.5-12)$$

In the programming stage (i), the samples are stretched by 6% by applying prescribed displacements on front and rear faces. In the programmed stage (ii), the samples are supported at their center to prevent rigid body motion. In all examples, the design domain is discretized by 8-node, tri-linear finite elements. The forward problem is solved by a nonlinear block Gauss-Seidel algorithm, thus taking advantage that that the stage (i) problem is independent of the stage (ii) problem. We observed that this strategy provides significant increase in robustness and reduction in computational costs over solving simultaneously the stage (i) and (ii) problems.

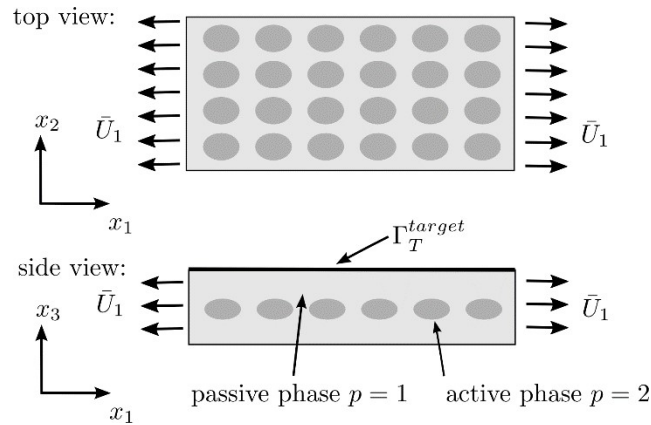


Figure 2.7.5-1: Geometry and boundary conditions of PAC design optimization problem.

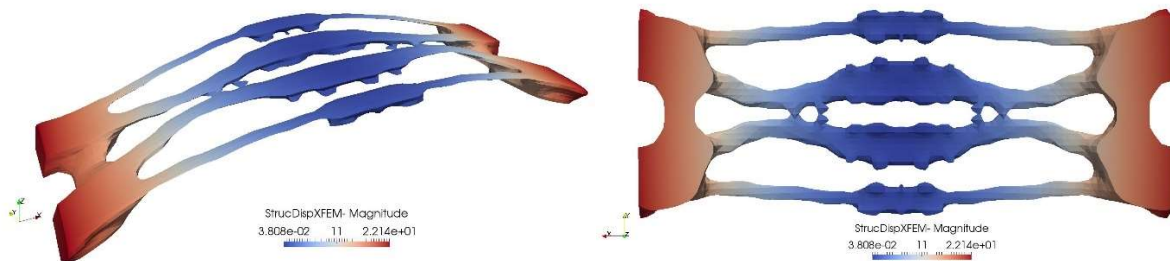


Figure 2.7.5-2: Optimization results using finite strain PAC models.

The level set function is discretized by the same mesh used for the PAC analysis. The nodal level set values are defined as functions of the optimization variables, using a linear filter [30]. The resulting parameter optimization problems are solved by the Globally Convergent Method of Moving Asymptotes[32] without sub-cycling. The design sensitivities of the objective and constraints are determined by the adjoint method. Here we solve the adjoint equations of the stage (i) and (ii) problems simultaneously, as these problems are linear. The designs are initialized with uniform arrays of cuboids of either active or passive material, surrounded by material of the other phase.

Figure 2.7.5-2 shows the layout of the SMP phase in the optimized design obtained with the nonlinear PAC model. Comparing this layout with the one obtained previously for a small strain PAC model shows that the designs have a similar geometry but differ locally. Note the additional ribs obtained when using the nonlinear model. The design optimized with the linear PAC model is inferior to the one optimized with the nonlinear PAC model. In future studies, additional optimization problems using the nonlinear PAC model will be performed and the potential of utilizing large deformation and instability phenomena, such as buckling, will be investigated.

## 2.7.6 Level-Set Topology Optimization with Contact, Cohesion, and Debonding

An important design consideration for engineered multiphase materials is the mechanical behavior along the material interfaces, in particular contact, cohesions, and debonding. To account for these phenomena in the design optimization process, we expanded our unique LSM-XFEM design optimization framework to contact and cohesive interface problems. In contrast to density based topology optimization approaches, where such phenomena cannot be resolved, the crispness of the interface description in both the geometry and analysis models allows us to solve and study such problems. The following study is published in: “R. Behrou, M. Lawry, and K. Maute. Level set topology optimization of structural problems with interface cohesion, *Int. J. Num. Meth. Engrg*, 2016, submitted”.

**Topology Optimization considering cohesive interface behavior:** Building upon the LSM-XFEM framework developed in previous years as part of this project, we created a finite element topology optimization approach for the design of two-phase structural systems considering contact and cohesion phenomena along material interfaces. The geometry of the material interface is described by an explicit level set method and the structural response is predicted by the eXtended finite element method. In this work the interface condition is described by a bilinear cohesive zone model based on the traction-separation constitutive relation. The non-penetration condition in the presence of compressive interface forces is enforced by a stabilized Lagrange multiplier method. The mechanical model assumes a linear elastic isotropic material, infinitesimal strain theory, and a quasi-static response. The optimization problem is solved by a nonlinear programming method and the design sensitivities are computed by the

adjoint method. For details on the mechanical model and the XFEM formulation of the cohesive interface model, the reader is referred to [38].

The performance of the method outlined above was evaluated studied with the optimization problem depicted in Figure 2.7.6-1, considering both a 2D and a 3D configuration. A structural anchor (represented by phase A) is embedded in a host material (designated as phase B) with frictionless and cohesive interface conditions, imposed at the boundary between both phases. We wish to determine the optimal geometry such that the holding force of the anchor is maximized.

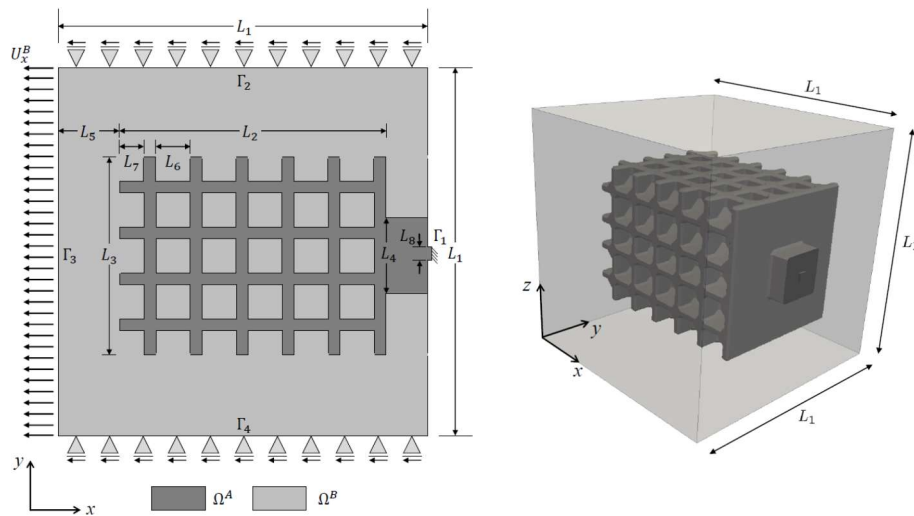


Figure 2.7.6-1: Design problems with cohesive contact interfaces.

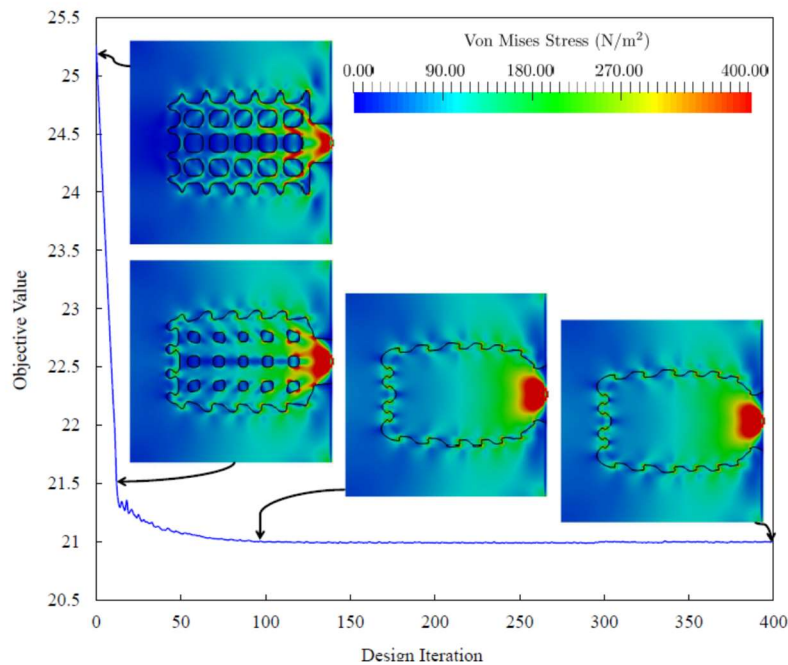


Figure 2.7.6-2: Evolution of 2D design assuming frictionless contact along the material interfaces.

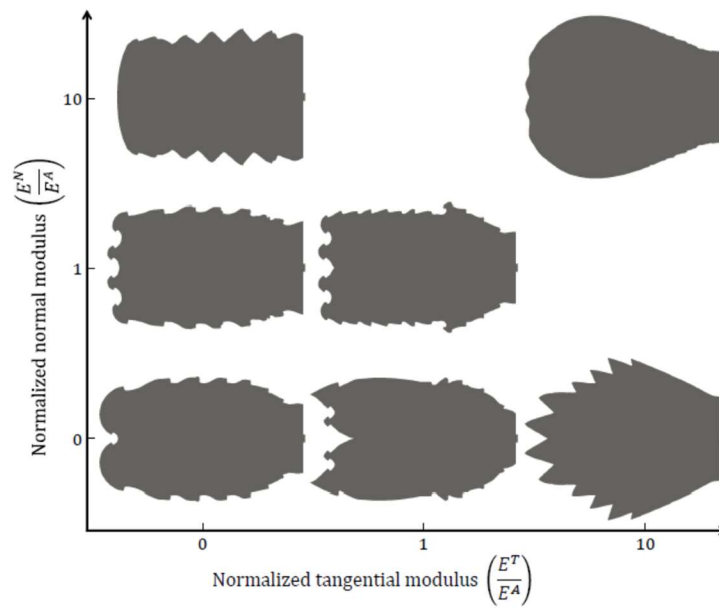


Figure 2.7.6-3: Influence of interface conditions on the optimized design (2D case).

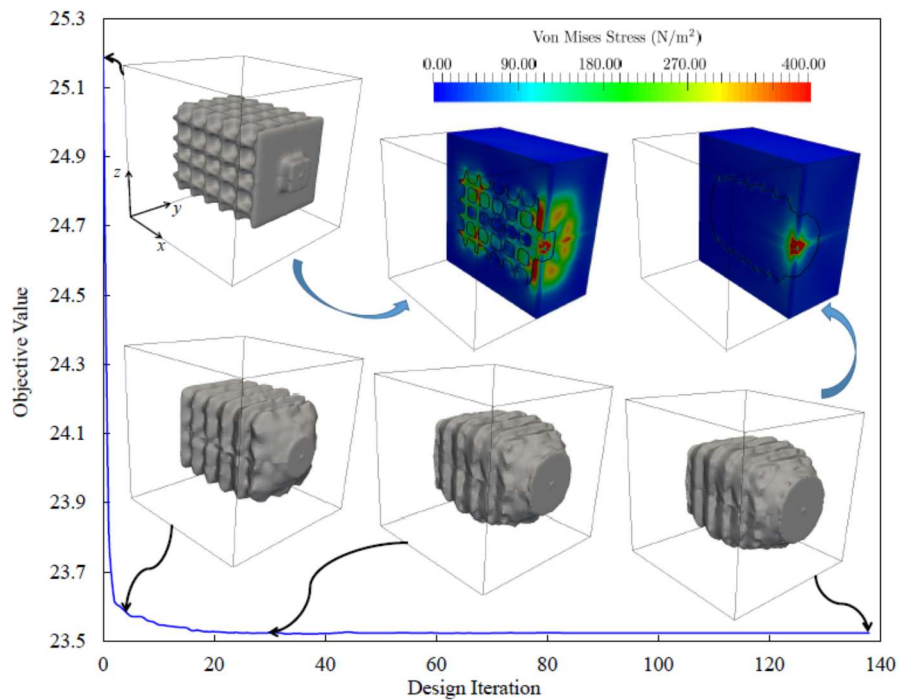


Figure 2.7.6-4: Evolution of 3D design assuming frictionless contact along the material interfaces.

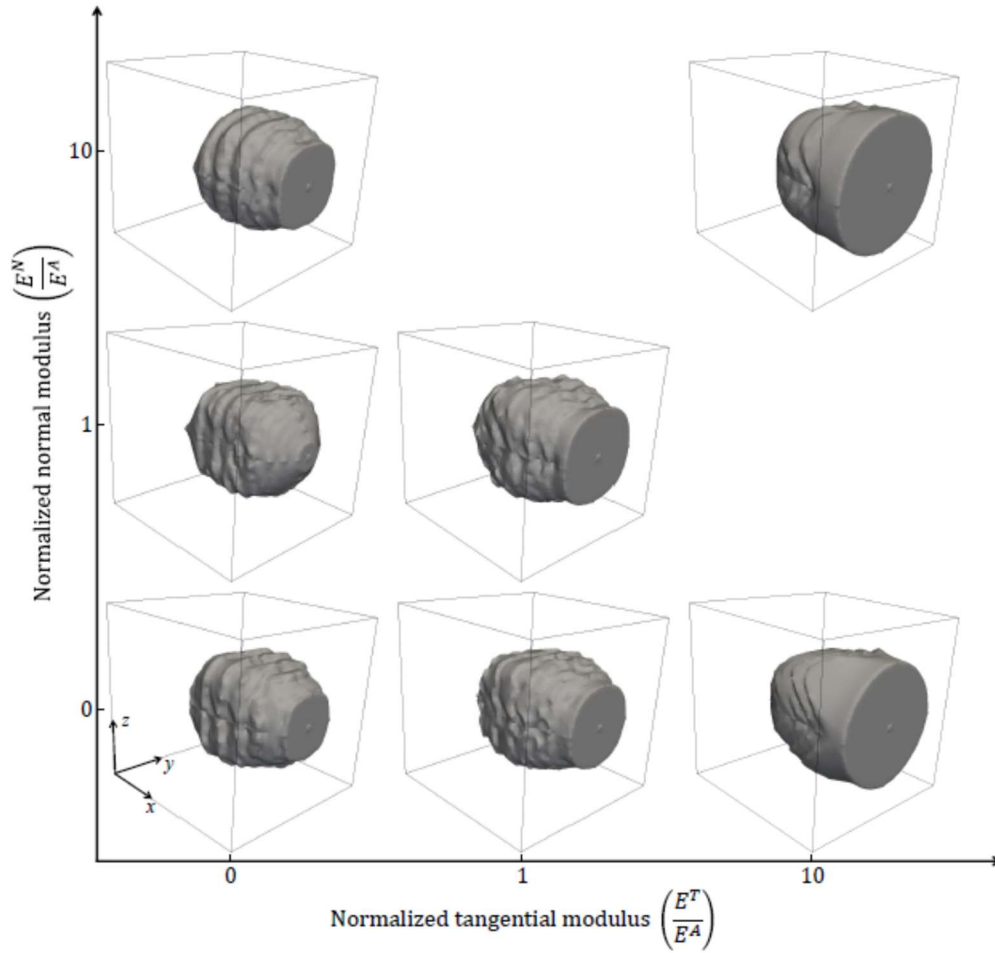


Figure 2.7.6-5: Influence of interface conditions on the optimized design (3D case).

Figure 2.7.6-2 shows the evolution of the design for the 2D case, assuming no-cohesion but accounting for frictionless contact. The holding force increases by forming noticeable barb-like structures. In Figure 2.7.6-3 we compare the influence of assuming cohesive forces in normal and tangential directions. We vary the resistance in horizontal direction along the horizontal axis and the resistance in normal direction along the vertical axis. The result in the lower left corner is the one for frictionless contact and the result in the upper right corner for perfect bonding. This design study illustrates the significant impact of the material interface properties on the optimal design.

In Figure 2.7.6-4 and Figure 2.7.6-5, the results for the 3D configuration are shown. Similar to the 2D design with frictionless contact, also the optimized 3D design features barbs along the interface. Again, the interface conditions have a significant influence on the optimized design. More details can be found in [38].

In summary, the results obtained from topology optimization reveal distinct design characteristics for the various interface phenomena considered. In addition, three-dimensional examples demonstrate optimal geometries that cannot be fully captured by reduced dimensionality. The optimization framework presented is limited to two-phase structural systems where the material interface is coincident in the undeformed configuration, and to structural responses that remain valid considering small strain

kinematics. In an ongoing study, the above results have been expanded onto accounting for finite strains [39] .

## Reference

1. Lendlein, A. and S. Kelch, *Shape-memory polymers*. Angewandte Chemie-International Edition, 2002. **41**(12): p. 2034-2057.
2. Liu, C., H. Qin, and P.T. Mather, *Review of progress in shape-memory polymers*. Journal of Materials Chemistry, 2007. **17**(16): p. 1543-1558.
3. Tibbits, S. and K. Cheung, *Programmable materials for architectural assembly and automation*. Assembly Automation, 2012. **32**(3): p. 216 – 225
4. Bendsøe, M.P. and O. Sigmund, *Topology optimization : theory, methods, and applications*. 2003, Berlin ; New York: Springer. xiv, 370 p.
5. Guo, Z.Y., X.Q. Peng, and B. Moran, *A composites-based hyperelastic constitutive model for soft tissue with application to the human annulus fibrosus*. Journal of the Mechanics and Physics of Solids, 2006. **54**(9): p. 1952-1971.
6. Guo, Z.Y., X.Q. Peng, and B. Moran, *Mechanical response of neo-Hookean fiber reinforced incompressible nonlinearly elastic solids*. International Journal of Solids and Structures, 2007. **44**(6): p. 1949-1969.
7. Lopez-Pamies, O., *An Exact Result for the Macroscopic Response of Particle-Reinforced Neo-Hookean Solids*. Journal of Applied Mechanics-Transactions of the Asme, 2010. **77**(2).
8. deBotton, G., I. Hariton, and E.A. Socolsky, *Neo-Hookean fiber-reinforced composites in finite elasticity*. Journal of the Mechanics and Physics of Solids, 2006. **54**(3): p. 533-559.
9. Oxman, N., *Variable property rapid prototyping*. Virtual and Physical Prototyping, 2011. **6**(1): p. 3-31.
10. Qi, H., et al., *Finite deformation thermo-mechanical behavior of thermally induced shape memory polymers*. Journal of Mechanics and Physics of Solids, 2008. **56**(5): p. 1730-1751.
11. Chester, S.A. and L. Anand, *A coupled theory of fluid permeation and large deformations for elastomeric materials*. Journal of the Mechanics and Physics of Solids, 2010. **58**(11): p. 1879-1906.
12. Chester, S.A. and L. Anand, *A thermo-mechanically coupled theory for fluid permeation in elastomeric materials: Application to thermally responsive gels*. Journal of the Mechanics and Physics of Solids, 2011. **59**(10): p. 1978-2006.
13. Fuchi, K., et al., *Origami Actuator Design and Networking Through Crease Topology Optimization*. Journal of Mechanical Design, 2015. **137**(9).
14. Kim, D. and J. Moon, *Highly conductive ink jet printed films of nanosilver particles for printable electronics*. Electrochemical and Solid-State Letters, 2005. **8**(11): p. J30-J33.
15. Huang, H. and F. Spaepen, *Tensile testing of free-standing Cu, Ag and Al thin films and Ag/Cu multilayers*. Acta Materialia, 2000. **48**(12): p. 3261-3269.
16. Kim, I., et al., *Effect of microstructural development on mechanical and electrical properties of inkjet-printed Ag films*. Journal of electronic materials, 2008. **37**(12): p. 1863-1868.
17. Lacour, S.E.P., et al., *Mechanisms of reversible stretchability of thin metal films on elastomeric substrates*. Applied Physics Letters, 2006. **88**(20): p. 204103.
18. Lu, N., et al., *Metal films on polymer substrates stretched beyond 50%*. Applied Physics Letters, 2007. **91**(22): p. 221909.
19. Li, T., et al., *Stretchability of thin metal films on elastomer substrates*. Applied Physics Letters, 2004. **85**(16): p. 3435-3437.



20. Merilampi, S., et al., *Analysis of electrically conductive silver ink on stretchable substrates under tensile load*. Microelectronics Reliability, 2010. **50**(12): p. 2001-2011.
21. Muth, J.T., et al., *Embedded 3D printing of strain sensors within highly stretchable elastomers*. Advanced Materials, 2014. **26**(36): p. 6307-6312.
22. Sawyer, E.J., et al., *Large increase in stretchability of organic electronic materials by encapsulation*. Extreme Mechanics Letters, 2016.
23. Schwarze, M. and S. Reese, *A reduced integration solid-shell finite element based on the EAS and the ANS concept-Geometrically linear problems*. International Journal for Numerical Methods in Engineering, 2009. **80**(10): p. 1322-1355.
24. Schwarze, M. and S. Reese, *A reduced integration solid-shell finite element based on the EAS and the ANS concept-Large deformation problems*. International Journal for Numerical Methods in Engineering, 2011. **85**(3): p. 289-329.
25. Mori, T. and K. Tanaka, *Average Stress in Matrix and Average Elastic Energy of Materials with Misfitting Inclusions*. Acta Metallurgica, 1973. **21**: p. 571-574.
26. Benveniste, Y., *A new approach to the application of Mori-Tanaka's theory in composite materials*. Mech. Materials, 1987. **6**: p. 147-157.
27. Makhija, D. and K. Maute, *Numerical Instabilities in Level Set Topology Optimization with the Extended Finite Element Method*. Structural and Multidisciplinary Optimization, 2014. **49**(2): p. 185-197.
28. Villanueva, C.H. and K. Maute, *Density and level set-XFEM schemes for topology optimization of 3-D structures*. Computational Mechanics, 2014. **54**(1): p. 133-150.
29. Ge, Q., et al., *Active Origami by 4D Printing*. Smart Materials & Structures, 2014. **23**: p. 094007-15.
30. Maute, K., et al., *Level Set Topology Optimization of Printed Active Composites*. ASME Journal of Mechanical Design, 2015. **137**(11): p. 111704.
31. Ge, Q., H.J. Qi, and M.L. Dunn, *Active materials by four-dimension printing*. Applied Physics Letters, 2013. **103**: p. 131901.
32. Svanberg, K., *A class of globally convergent optimization methods based on conservative convex separable approximations*. Siam Journal on Optimization, 2001. **12**(2): p. 555-573.
33. Maute, K., et al., *Level Set Topology Optimization of Printed Active Composites*. Journal of Mechanical Design, 2015. **137**(11): p. 111402-111402.
34. Ge, Q., H.J. Qi, and M.L. Dunn, *Active materials by four-dimension printing*. Applied Physics Letters, 2013. **103**(13): p. 131901.
35. Nitsche, J., *Über ein Variationsprinzip zur Lösung von Dirichlet-Problemen bei Verwendung von Teilräumen, die keinen Randbedingungen unterworfen sind*. Abhandlungen aus dem Mathematischen Seminar der Universität Hamburg, 1975. **36**: p. 9-15.
36. Burman, E. and P. Hansbo, *Fictitious domain finite element methods using cut elements: I. A stabilized Lagrange multiplier method*. Computer Methods in Applied Mechanics and Engineering, 2010. **199**(41): p. 2680-2686.
37. Burman, E. and P. Hansbo, *Fictitious domain finite element methods using cut elements: II. A stabilized Nitsche method*. Applied Numerical Mathematics, 2012. **62**(4): p. 328-341.
38. Behrou, R., M. Lawry, and K. Maute, *Level set topology optimization of structural problems with interface cohesion*. International Journal for Numerical Methods in Engineering, 2016.
39. Lawry, M. and K. Maute, *Level set shape and topology optimization of finite strain bilateral contact problems*. International Journal for Numerical Methods in Engineering, 2016.

# AFOSR Deliverables Submission Survey

Response ID:7257 Data

1.

**Report Type**

Final Report

**Primary Contact Email**

Contact email if there is a problem with the report.

maute@colorado.edu

**Primary Contact Phone Number**

Contact phone number if there is a problem with the report

3037352103

**Organization / Institution name**

University of Colorado Boulder

**Grant/Contract Title**

The full title of the funded effort.

3D Printed Composites for Topology-Transforming Multi-functional Devices

**Grant/Contract Number**

AFOSR assigned control number. It must begin with "FA9550" or "F49620" or "FA2386".

FA9550-13-1-0088

**Principal Investigator Name**

The full name of the principal investigator on the grant or contract.

Kurt Maute

**Program Officer**

The AFOSR Program Officer currently assigned to the award

Byung L. Lee

**Reporting Period Start Date**

07/15/2013

**Reporting Period End Date**

07/14/2016

**Abstract**

The goal of the research was to develop a new methodology for the fabrication and the design of new multifunctional composites and devices using 3D printing. The main accomplishments of this project can be summarized as follows: 1) Proposing and demonstrating the 4D printing concept and novel printed active composites (PACs); 2) developing multiple PAC continuum mechanics PAC models of various levels of accuracy and complexity; 3) developing the 4D printing concept to design PACs undergoing multiple shape changes; 4) developing a PAC-based concept that enables reversible shape changes; 5) application of PACs for printed origami design; 6) developing a finite element framework for the optimum design of PACs by topology optimization; 7) optimizing and experimentally characterizing PACs that undergo desired shape changes.

**Distribution Statement**

This is block 12 on the SF298 form.

Distribution A - Approved for Public Release

**Explanation for Distribution Statement**

DISTRIBUTION A: Distribution approved for public release.

If this is not approved for public release, please provide a short explanation. E.g., contains proprietary information.

## SF298 Form

Please attach your [SF298](#) form. A blank SF298 can be found [here](#). Please do not password protect or secure the PDF. The maximum file size for an SF298 is 50MB.

[sf0298+Maute.pdf](#)

**Upload the Report Document. File must be a PDF. Please do not password protect or secure the PDF. The maximum file size for the Report Document is 50MB.**

[Final+Report.pdf](#)

**Upload a Report Document, if any. The maximum file size for the Report Document is 50MB.**

### Archival Publications (published) during reporting period:

- [1] Ge, Q., Qi, H.J., Dunn, M.L., 2013, Active Materials by 4D Printing. Applied Physics Letter, 103, 131901.
- [2] Ge, Q., Dunn, C., Qi, H.J., Dunn, M.L., 2014. Active Origami by 4D Printing. Smart Materials and Structures, 23, 094007-15.
- [3] Yu, K., Ge, Q., Qi, H.J., 2014, Reduced Time as a Unified Parameter Determining Fixity and Free Recovery of Shape Memory Polymers. Nature Communication, 5:3066.
- [4] Yu, K., Ritchie, A., Mao, Y., Dunn, M.L., Qi, H.J., 2015. Controlled Sequential Shape Changing Components by 3D Printing of Shape Memory Polymer Multimaterials. Procedia IUTAM, 12, 193-203.
- [5] K. Maute, A. Tkachuk, J. Wu, H. J. Qi, Z. Ding, and M.L. Dunn. 2015. Level Set Topology Optimization of Printed Active Composites. ASME Journal of Mechanical Design, 137: 111704-1, 2015.
- [6] Mao, Y., Yu, K., Isakov, M., Wu, J., Dunn, M.L., and Qi, H.J., 2015. Sequential Self-Folding Structures by 3D Printed Digital Shape Memory Polymers, Scientific Reports, 5:13616.
- [7] Wu, J., Yuan, C., Ding, Z., Isakov, M., Mao, Y., Wang, T., Dunn, M.L., Qi, H.J. 2016. Multi-shape active composites by 3D printing of digital shape memory polymers. Scientific Reports 6:24224.
- [8] Mao, Y., Ding, Z., Yuan, C., Ai, S., Isakov, M., Wu, J., Wang, T., Dunn, M.L., and Qi, H.J., 2016. 3D Printed Reversible Shape Changing Component with Stimuli Responsive Materials. Scientific Reports 6:24761.
- [9] Zhao, Z, Mu, X., Wu, J., Qi, H.J., Fang, D., 2016. Effects of oxygen on interfacial strength of incremental forming of materials by photopolymerization. Extreme Mechanics Letters 9(1):108–118.
- [10] Zhao, Z, Wu, J., Mu, X., Qi, H.J., Fang, D., 2016. Origami Folding by Frontal Photopolymerization, submitted.
- [11] Mu, Q, Dunn, C.K. Wang, L., Dunn, M.L., Qi, H.J., Wang, T., 2016. Thermal cure effects on electromechanical properties of conductive wires by direct ink write for 4D printing and soft machines, submitted.
- [12] Sharma, A., Villanueva, H., Maute, 2016. On Shape Sensitivities with Heaviside-Enriched XFEM, submitted to Structural and Multidisciplinary Optimization.
- [13] Behrou, R., Lawry, M., Maute, K., 2016. Level set topology optimization of structural problems with interface cohesion, submitted to Int. J. Num. Meth. Engrg.
- [14] Lawry, M., Maute, K., 2016. Level set shape and topology optimization of finite strain bilateral contact problems, submitted to Int. J. Num. Meth. Engrg.

### New discoveries, inventions, or patent disclosures:

**Do you have any discoveries, inventions, or patent disclosures to report for this period?**

No

**Please describe and include any notable dates**

**Do you plan to pursue a claim for personal or organizational intellectual property?**

**Changes in research objectives (if any):**

**Change in AFOSR Program Officer, if any:**

**Extensions granted or milestones slipped, if any:**

**AFOSR LRIR Number**

**LRIR Title**

**Reporting Period**

**Laboratory Task Manager**

**Program Officer**

**Research Objectives**

**Technical Summary**

**Funding Summary by Cost Category (by FY, \$K)**

	Starting FY	FY+1	FY+2
Salary			
Equipment/Facilities			
Supplies			
Total			

**Report Document**

**Report Document - Text Analysis**

**Report Document - Text Analysis**

**Appendix Documents**

**2. Thank You**

**E-mail user**

Nov 15, 2016 17:29:52 Success: Email Sent to: maute@colorado.edu